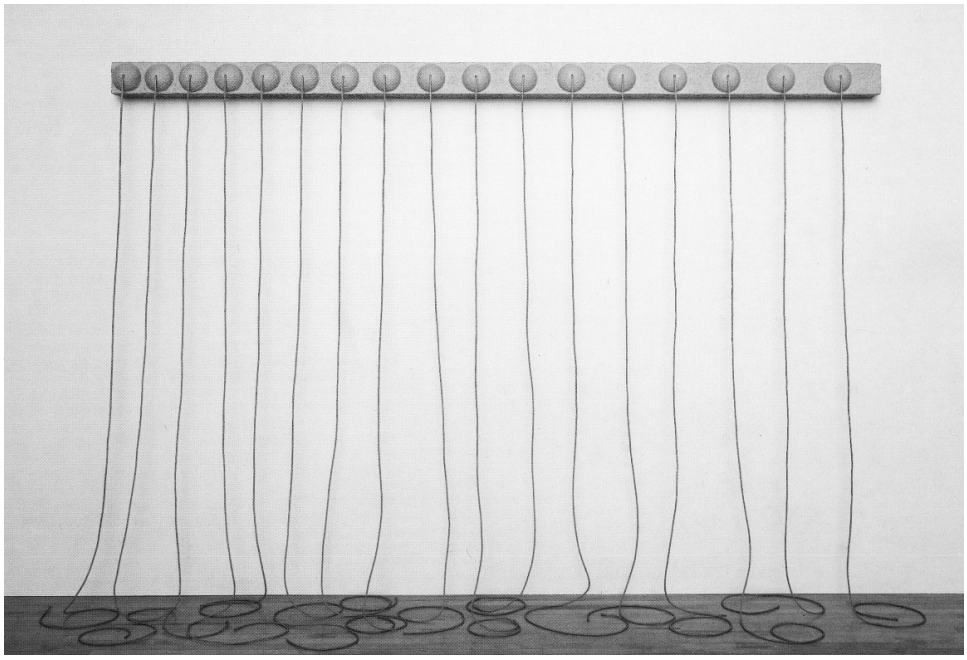

Extratropical Synoptic Structures at Tropopause Levels

Mark A. Liniger
Diss. ETH Nr. 14632

Diss. ETH No. 14632

Extratropical Synoptic Structures at Tropopause Levels

A dissertation submitted to the
SWISS FEDERAL INSTITUTE OF TECHNOLOGY
ZURICH

for the degree of
Doctor of Natural Sciences

presented by
MARK A. LINIGER

born 23 Mai, 1973
citizen of Luzern, Switzerland

accepted on the recommendation of
Prof. Dr. Huw C. Davies, examiner
Dr. Andreas Stohl, co-examiner
Dr. Heini Wernli, co-examiner

2002

Cover:
Addendum, 1967
Eva Hesse 1936-1970
Painted papier mâché, wood and cord
Tate Modern, London, purchased 1979

This sculpture has a simple, serial organisation consistent with Hesse's belief that "the work exists only for itself". Though particular spare, it has an organic informality that is characteristic for her work. The semi-circular forms which the cords hang resemble breasts. At eye level, the ropes are suspended in relative orderliness, yet nearer the floor they loop into large, chaotic coils. As Hesse said, "I was always aware that I could combine order and chaos, string and mass, huge and small".

Iwona Blazwick and Tina Fiske

Contents

Abstract

The dynamics and associated transport processes of the upper troposphere and lower stratosphere, i.e. at tropopause levels, are of primary importance not only for the development of underlying weather systems, but also for the chemical composition and radiative properties of the atmosphere. However, the processes in this region are not yet fully understood, not least because of: (i) the wide range of involved scales, in space and time; (ii) the difficulties for its observations; (iii) and the lack of highly resolved, analysed fields.

A case study typifying these aspects is undertaken for a strong tropopause fold into the troposphere. Water vapour observations of a state-of-the-art LIDAR instrument and satellite scans are compared to results from the Reverse Domain Filling (RDF) technique and the novel Lagrangian Forward Projection (LFP) applied to GCM analysed fields. Cross-tropopause transport across the western edge of the fold is identified by chaotic advection and a collocated mismatch is found between the water vapour distribution and the satellite data. Prompted by strong diabatic processes along its eastern flank, the fold breaks up over the Alps and disintegrates resulting in significant stratosphere-troposphere exchange by convective and radiative processes. The investigation of the dynamical counterpart, a tropospheric extrusion into the stratosphere, reveals cross-tropopause transport into the stratosphere. Together, both case study examples stress the importance of these upper-level structures for large scale transport and stirring by the identification of several dynamically distinctive origins and destinations.

In a second part, a novel dispersion measure is employed to characterize isentropic transport of various synoptic- to global-scale features. Its relation to potential vorticity (PV) is examined in detail by the inspection of individual structures and from a statistical perspective. The transport barrier along the polar vortex edge within the winter stratosphere is identified by a systematic triple band in the dispersion structure. Higher dispersion can in general be attributed to the tropopause region and is richer in structures, but the interrelation to PV is much less pronounced. From a global perspective, the results suggest that exchange across the extra-tropical tropopause must be seen as a continuous process that is not confined to rare events. This implies fundamentally different transport characteristics than for the polar vortex. The examined individual events indicate a linkage to synoptic- to meso-scale structure associated with Rossby-wave breaking.

Therefore, an identification procedure for anomalies as a deviation from the climatological mean tropopause is developed that focuses on the mid-latitude tropopause and allows a direct inter-seasonal comparison differently from conventional methods. The combination of the seasonal variability and climatological geographical distribution of the dispersion and anomaly frequency is in good agreement to the hypotheses. In winter, maximum dispersion along the tropopause is identified in regions of highest tropopause variability, collocated with the storm track regions. Both within the stratosphere and troposphere, lower dispersion and lower anomaly frequency is found. In summer, the region of maximum variability is much broader and shifted polewards and the correlation between PV and Lagrangian dispersion is significantly weaker, in particular in the lowermost stratosphere.

Zusammenfassung

Die Dynamik und die damit verbundenen Transportprozesse in der oberen Troposphäre und unteren Stratosphäre, d.h. auf Tropopausenniveau, sind von grosser Bedeutung sowohl für die Entwicklung der darunter liegenden Wettersysteme als auch für die chemische Zusammensetzung und Strahlungsprozesse der Atmosphäre. Die Vorgänge sind jedoch noch nicht vollständig verstanden, hauptsächlich wegen: (i) eines weiten Skalenbereiches, sowohl in Raum und Zeit; (ii) Schwierigkeiten ihrer Beobachtung; (iii) und dem Mangel an hoch aufgelösten Analysefeldern.

Eine Fallstudie, typisch für die erwähnten Aspekte, untersucht eine starke Tropopausenfaltung in die Troposphäre hinein. Wasserdampfbeobachtungen eines modernsten LIDAR-Gerätes und Satellitenaufnahmen werden verglichen mit Resultaten von Reverse Domain Filling (RDF) Berechnungen und der neu entwickelten Lagrangian Forward Projection (LFP), beide basierend auf globalen Analysefeldern. Es kann Transport durch die Tropopause durch chaotische Advektion entlang der westlichen Flanke der Falte identifiziert werden. Die tatsächliche Wasserdampfverteilung stimmt desweiteren nicht mit der Satellitenaufnahme überein. Durch diabatische Prozesse entlang der östlichen Flanke, bricht die Falte über den Alpen auf und die Überbleibsel lösen sich auf, begleitet von starkem Stratosphären-Troposphärentransport durch Konvektion und Strahlungsprozesse. Die Untersuchung des dynamischen Gegenstückes, einer troposphärischen Extrusion in die Stratosphäre, enthüllt Transport von troposphärischer Luft in die Stratosphäre. Zusammen betrachtet, betonen beide Fallstudien durch die Identifikation von mehreren, dynamisch verschiedenen Herkunfts– und Bestimmungsorten die Bedeutung von Strukturen auf dem Tropopausenniveau für grossskaligen Transport und Vermischungsprozesse.

In einem zweiten Teil wird ein neuartiges Ausbreitungsmass, im Folgenden als Dispersion bezeichnet, angewendet, um isentropischen Transport von synoptisch– bis globalskaligen Strukturen zu beschreiben. Die Beziehung der Dispersion zur potentiellen Wirbelstärke (PV) wird mittels der Betrachtung von einzelnen Strukturen und statistischen Analysen ermittelt. Die Transportbarriere entlang des polaren Wirbels in der Winterstratosphäre zeichnet sich durch ein dreifaches Band in der Dispersionsverteilung aus. Höhere, stark strukturierte Dispersion wird in der Tropopausenregion gefunden, wo aber die Beziehung zur PV schwächer ist. Aus einer globalen Perspektive implizieren die Resultate, dass der Austausch durch die aussertropische Tropopause als kontinuierlicher Prozess betrachtet werden muss, und nicht auf einzelne, grossskalige Ereignisse zurückzuführen ist. Die Tropopause hat deshalb fundamental andere Transporteigenschaften als der polare Wirbel. Desweiteren scheinen synoptisch– bis mesoskalige Strukturen, welche durch Brechen von Rossby-Wellen entstehen, stark mit der Dispersionsstruktur zusammenzuhängen.

Deshalb wird eine Technik zur Identifikation von Tropopausenanomalien als Abweichung vom klimatologischen Mittel entwickelt. Sie konzentriert sich auf die mittleren Breiten und erlaubt, anders als bestehende Methoden, eine direkte Betrachtung der saisonalen Variabilität. Die Hypothesen werden bestätigt durch die kombinierte Analyse der Häufigkeiten und den entsprechenden Dispersionsfeldern. Im Winter wird maximale Dispersion entlang der Tropopause in der Region der höchsten Tropopausenvariabilität gefunden, was den Sturmbahnregionen entspricht. Sowohl die Stratos– als auch die Troposphäre sind durch tiefere Dispersionswerte und Anomaliefrequenzen ausgezeichnet. Im Sommer ist die Region hoher Variabilität breiter und polwärts verschoben und die Korrelation zwischen PV und der Dispersion ist viel schwächer, insbesondere in der untersten Stratosphäre.

Chapter 1

Introduction

1.1 Motivation

The main global atmosphere may be divided into two regions: the troposphere containing about 90% of the mass and located in the lower 10 km, and above the stratosphere reaching up to about 50 km (Fig. 1.1). The two domains differ significantly by their chemical concentrations, e.g. the stratospheric humidity concentration is much lower and the ozone concentration much higher than in the troposphere. The troposphere is further characterized by weak vertical stability, latent heat release and strong baroclinicity in the extra-tropics that all can cause significant vertical motion. For the stratosphere, high vertical stability is characteristic and the infrared radiative cooling is mainly balanced by the radiative heating due to the ultraviolet absorption in the ozone layer (Holton, 1979).

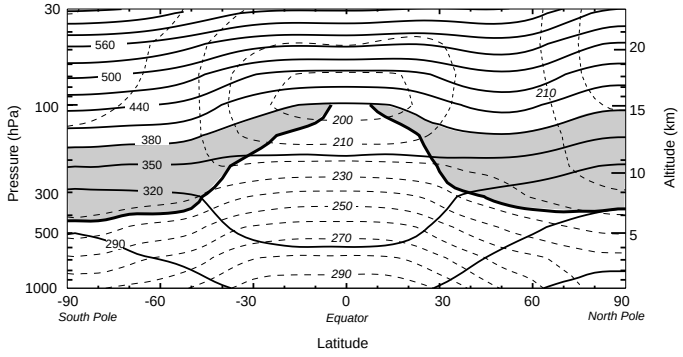

Figure 1.1: Latitude–altitude cross section for January 1993 showing longitudinally averaged potential temperature (solid contours) and temperature (dashed contours). The heavy solid contour (cutoff at the 380 K isentrope) denotes the 2 pvu potential vorticity contour, which approximates the tropopause outside the tropics. Shaded areas denote the "lowermost stratosphere" whose potential temperature surfaces span the tropopause (from Holton et al., 1995).

Transport characteristics within the two spheres and from one into the other are strongly related to the corresponding thermo-dynamical properties. On time scales of a few days to weeks a quasi-horizontal adiabatic flow dominates transport within the stratosphere, whereas there is also significant cross-isentropic motion associated with synoptic-scale activity within the troposphere.

Tropopause

The surface separating the tropo– from the stratosphere is referred to as tropopause and characterized in various ways (see Holton et al., 1995, for a detailed review). The

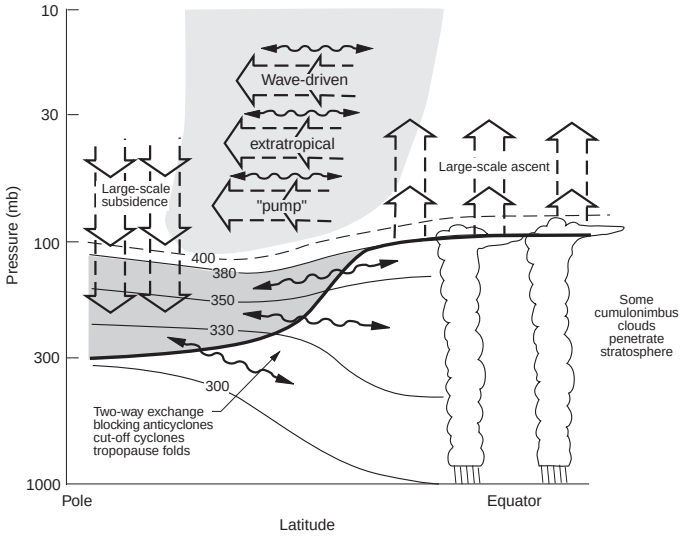

Figure 1.2: Dynamical aspects of stratosphere-troposphere exchange. The tropopause is shown by the thick line. Thin lines are isentropic or constant potential temperature surfaces labeled in Kelvins. Heavily shaded region is the lowermost stratosphere, light shading in the overworld denotes wave-induced forcing. The wavy double-headed arrows denote meridional transport by eddy motions. The broad arrows show transport by the global-scale circulation, which is driven by the extra-tropical pump (from Holton et al., 1995).

World Meteorological Organization (WMO) defines the tropopause as the lowest level at which the temperature lapse rate decreases to 2°C km^{-1} or less, provided also that the average lapse rate between this level and all higher levels within 2 km does not exceed 2°C km^{-1}. Beside this thermal definition, there are also several chemical definitions based on humidity, ozone or other species as isotopes and the "dynamical tropopause" definition based on potential vorticity and potential temperature (see also Section 1.3).

With a focus on adiabatic transport, often a subdivision of the atmosphere is employed for the study of transport near the extra-tropical tropopause by grouping the isentropes located entirely below the tropopause, referred to as "underworld", isentropes cutting the tropopause, the "middleworld", and the ones above, the "overworld" (Hoskins, 1991, see also Fig. 1.1). The stratospheric part of the middleworld is also referred to as "lowermost stratosphere".

Stratosphere

Within the stratosphere, a zonal-temporal average of the wind fields reveals a residual circulation in the form of a hemispheric, Hadley-like cell with a rising motion in the tropics, a poleward drift in the stratosphere, and by continuity of mass a return flow into the troposphere in the extratropics (broad arrows in Fig. 1.2). The mechanism was observed and deduced from Helium and humidity measurements over England and known as "Brewer-Dobson" circulation (Brewer, 1949; Dobson, 1956). Its forcing is attributed to Rossby wave breaking within the stratosphere acting as an "extratropical pump" (Haynes et al., 1991) in the region that is also referred to as "surf zone" (McIntyre and Palmer, 1984).

Polewards of the surf zone, the global-scale polar vortex is persistent in the winter hemisphere for several months (indicated by a negative temperature anomaly over the North Pole in Fig. 1.1), delimited by a pronounced circumpolar jet (Juckes and McIntyre, 1987). The impermeability of its edge and the strong radiative cooling is directly associated with downward motion and the ozone destruction in its interior (cf. "ozone hole"). The displacement of its edge and final disruption, i.e. "sudden stratospheric warming", is related to upward propagating Rossby waves of low zonal wavenumber (Holton et al., 1995; Polvani and Saravanan, 2000).

Troposphere and middle world

The simplicity of this transport picture must though be used with care, since it is the result of averaging and not detectable in instantaneous fields. In particular within the tropospheric component of the middleworld, the net flux across the tropopause into the troposphere is associated with processes of high variability and down to meso-scales that transport air masses in both directions (Bourqui, 2001; Wernli and Bourqui, 2002).

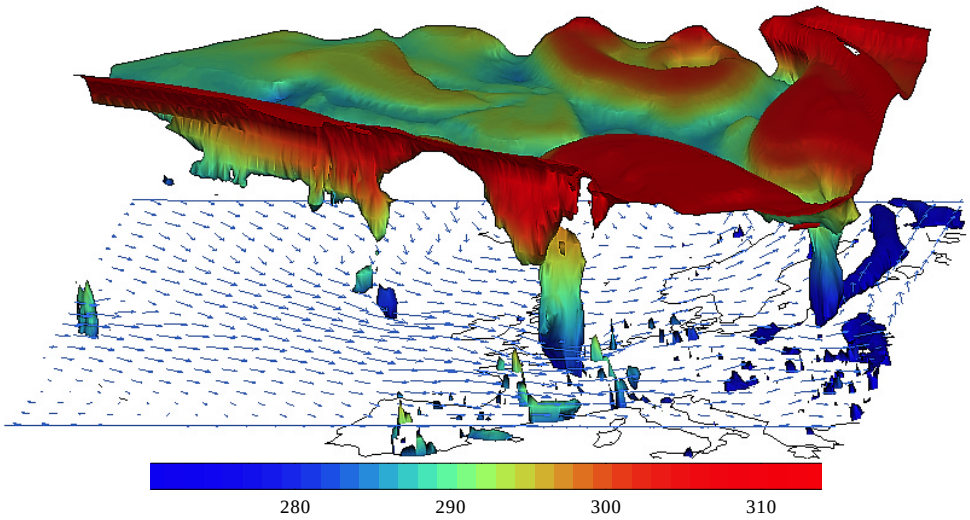

Figure 1.3: The 2 pvu iso-surface from a local model simulation at 06 UTC 26 Dec 1999. The surface is colored with the potential temperature values. Also shown are the 850 hPa horizontal wind vectors, the length of the maximum wind vector corresponds to 43.5 $\mathrm{m\,s^{-1}}$ (from Wernli et al., 2002).

Although the different chemical concentrations indicate the extratropical tropopause acting as a transport barrier similar to the polar vortex edge, the tropopause exhibits stronger horizontal gradients and its distortion is generally associated with Rossby waves of higher zonal wave number (Platzmann, 1968). The nonlinear Rossby wave breaking results in generally two different types of events: intrusions of stratospheric air advected equatorward into the troposphere (Appenzeller and Davies, 1992) and extrusions where tongues of tropospheric air extend poleward in the stratosphere (Peters and Waugh, 1996). The breaking is often associated with the generation of filamentary structures of sub-synoptic scales (Appenzeller et al., 1996). Also, baroclinic instability associated with the meridional temperature gradient and diabatic processes can lead to rapid change of its diverse structures, as observed for the winter storm "Lothar" (Wernli et al., 2002): An stratospheric intrusion in the form of a pronounced tropopause fold was further enhanced by the

interaction with the diabatically sustained storm's core in mid-tropospheric levels (Figure 1.3). The three-dimensional view of the tropopause generated with a mesoscale model simulation demonstrates the richness of structures as localized vertical tropopause deflections. The blob over France corresponds to the storm's core and extraordinary strong rotation.

Indeed, transport across the extratropical tropopause, i.e. stratosphere to troposphere and troposphere to stratosphere exchange (STE resp. TSE), is strongly linked to the upper-level signatures of weather regimes. Various studies have been conducted using both numerical and observational methods trying to link and quantify these processes. Important studies include considerations of STE in cut-off lows (Price and Vaughan, 1993), calculation of net transport during a tropopause folding event (Lamarque and Hess, 1994), the geographical and seasonal variations (Chen, 1995). A detailed review of STE is provided by Holton et al. (1995). More recently comparisons have been undertaken of various numerical methods (Wirth and Egger, 1999; Kowol-Santen et al., 2000) and the Lagrangian transport approach (Bourqui, 2001). STE affects water vapour, ozone and isotope (as Be^7) mixing ratios in the tropopause region that can even be detected in ground based, mountainous stations (Stohl et al., 2000).

1.2 Outline of the thesis

This study focuses on the middleworld near the tropopause. Transport characteristics are put into the context of the large, synoptic-scale variability of the extratropical tropopause in order to examine the link between the Lagrangian and the Eulerian views and the nature of the tropopause as a potential transport barrier.

In two case study analyses features associated with weather regimes and transport processes are related to smaller scale structures (Chapter 3). The first case is that of a deep tropopause fold that occurred during a field campaign undertaken with state-of-the-art measurements that enabled a direct intercomparison between various datasets. The dynamical counterpart of a tropospheric extrusion completes the picture of middleworld transport.

Based upon the derived insights, a statistical overview is established to further asses the properties of the intrinsic dynamical features (Chapter 4). The computation of a large number of trajectories is employed to describe the transport characteristics of the middle- and upperworld. The geographical and seasonal variability of Eulerian features potentially relevant for transport are then examined from a climatological standpoint (Chapter 5).

1.3 Potential vorticity

The space-time distribution of Ertel's potential vorticity (PV or Q) is an useful field to examine the dynamics of the upper troposphere and lower(most) stratosphere. PV combines absolute vorticity and static stability on a rotating sphere and the general form derived by Ertel (1942) can be expressed (under the hydrostatic assumption and the earth to be spherical) in the pressure coordinate system by:

$$\mathrm{PV} = -g\,\vec{\omega}\cdot\vec{\nabla}\theta\ ,$$

where $\vec{\omega} = \vec{\zeta} + f\vec{k}$ denotes the absolute vorticity, $\vec{\zeta} = \vec{\nabla} \wedge \vec{u}$ the relative vorticity, $f = 2\Omega \sin \Phi$ represents the earth rotational effect, $\vec{k}$ is the normal vector, $\vec{u}$ the velocity and $\theta = (p_0/p)^{\kappa} T$ the potential temperature.

PV exhibits several properties that combine kinematic and thermodynamic aspects, and makes it a powerful diagnostic for synoptic to global scale studies (Hoskins et al., 1985), although it can not be directly measured and its calculation requires spatial derivatives of wind and potential temperature fields. This is probably why its practical use was not possible until analysis fields from numerical models were available in the late 1970ies. A comprehensive review can be found in Hoskins et al. (1985), a recent introduction to PV as a diagnostic for meteorologists is given by Morgan and Nielsen-Gammon (1998), Some characteristics of PV of general interest and/or of importance to this work are itemized below:

Conservation

Under the adiabatic and frictionless assumption, PV is materially conserved

$$\frac{D}{Dt}\mathrm{PV} = 0 \ .$$

Under these conditions PV may be regarded as a passive tracer. Thus for example, PV is conserved on a surface of constant θ (isentrope), or vice versa, θ is conserved on a iso-PV surface.

Invertibility principle

The spatial distribution of PV anomalies against a given background state and an appropriate boundary condition (e.g. the surface temperature) permits the reconstruction of balanced[1] dynamics (Kleinschmidt, 1950; Hoskins et al., 1985). In a simplified picture, this can also be seen as an analogy to electrostatics, where the charge distribution (corresponding to PV) determines the electric field and vice versa (e.g. Bishop and Thorpe, 1994; Thorpe and Bishop, 1995).

Dynamical tropopause

The strong change in vertical stability resp. lapse rate across the tropopause (see Chapter 1.1) induces a strong change in PV for constant realative vorticity. Indeed, a strong vertical increase in PV in the extratropical stratosphere makes it possible to define a "dynamical tropopause" by PV. Usually, the iso-PV surface of 2 pvu[2] is used in the extra-tropics (see Fig. 1.1 resp. Holton et al., 1995). In the tropics, most definitions identify multiple tropopauses or fail completely (e.g. the PV tropopause). Usually, the isentrope of 380 K is used for dynamical studies.

[1] as balance condition, usually the geostrophic or the quasi-geostrophic approximations are chosen

[2] potential vorticity unit, 1 pvu = $10^{-6} m^2 s^{-1} K kg^{-1}$

Non-conservation

The conservation of PV is limited by diabatic and frictional processes and the sources are given by (Hoskins et al., 1985)

$$\frac{D}{Dt}\mathrm{PV} = -\vec{\nabla}\left(g\,\dot{\theta}\,\vec{\omega} + g\vec{F}\times\vec{\nabla}\theta\right) \ .$$

Diabatic effects ($\dot{\theta}$), as latent heat release in the troposphere or the (weaker) radiative heating and cooling in the stratosphere and above clouds, and frictional effects (F), over orography or associated with turbulence (Shapiro, 1980), can modify the PV distribution.

Considering the aims of this study, investigations of structures in the upper troposphere and lower stratosphere, condensational processes are the most important ones both with respect to location and scale. A region of latent heat release, i.e. $\dot{\theta} \neq 0$, can induce a positive (negative) Lagrangian PV tendency before (after) passing the heating region. The resulting change of PV strongly depends on the intensity and geometry of the heating and the synchronous ascent (Stoelinga, 1996; Wernli and Davies, 1997; Wernli, 1997; Pomroy and Thorpe, 2000).

Chapter 2

Data and Methodology

To a large extend, this study is based on spatio-temporally gridded data, created by combining measured data with short-term forecasts in a physically consistent manner (Section 2.1). This data is employed to calculate a PV-based global coordinate system (Section 2.2) and to introduce a Lagrangian perspective (Section 2.3 and 2.4). High-resolution state of the art observational data, DIAL and satellite scans, allow data/measurement inter-comparisons (Section 2.5 and 2.6).

2.1 Analysed and re-analysed data

The spatial fields of velocity, temperature and specific humidity (q) used in this study are referred to as "analysis fields" and stem from the European Center for Medium-range Weather Forecast (ECMWF). The fields are available at a time interval of 6 h. The process of their production is described hereafter (further details and references can be found at ECMWF, 2001).

1 May 1985	T106L16
13 May 1985	T106L19
17 September 1991	T213L31
1 April 1998	T319L31
9 March 1999	T319L50
12 October 1999	T319L60
21 November 2000	T511L60

Table 2.1: Resolution in ECMWF forecast model

The forecast model is based on a hydrostatic primitive equations and includes sophisticated parameterization schemes as for convection, gravity wave drag, radiation and planetary boundary layer processes, and was continuously reformed (e.g. Simmons et al., 1989; Hortal and Simmons, 1991; Ritchie et al., 1995). In Table 2.1 the truncated horizontal wavenumber and the number of hybrid levels are given from 1985 onwards.

Due to the chaotic nature of the atmospheric dynamics, forecast integrations are very sensitive to the initial conditions. The determination of the initial state as exact as possible is based on a worldwide operational measurement network with an irregular spacing consisting of primarly surface observations from weather stations, radio-sondes, aircraft observations and radiance and motion vectors from satellites. The data are combined with a short-range forecast (background) field by minimizing the differences in a dynamically consistent way to yield the analysis fields, a process that is referred to as assmilation.

Early assimilation techniques interpolate between the observed data and the background field taking into account the uncertainities of both values ("optimum interpolation"). An enhancement was achieved by the introduction of the 3-D variational (3D-Var) assimilation taking into account observations in a given time window (e.g. ±3 h) around the designated analysis time and minimizes the error with an iterative variational technique (e.g. Courtier et al., 1998; Rabier et al., 1998; Andersson et al., 1998). The first 3D-Var scheme was implemented in ECMWF operations in January 1996.

The computationally more expensive 4-D variational (4D-Var) analysis, introduced in November 1997, is an extension of 3D-Var incorporating also the time dimension. This is done by employing a simplified dynamical model that can be run also backward in time. Thus, the error between the model state and observational data can be calculated at exactly the time (and location) the measurements were taken by running the model iteratively forward and backward in time. A time window of ±3 h is used, from September 2000 on even ±6 h. (e.g. Rabier et al., 2000; Mahfouf and Rabier, 2000; Klinker et al., 2000).

The constraints of changes in the model formulation makes it difficult to compare analysis fields of different years. The Re-Analysis projects circumvent this problem by regenerating analysis fields for a certain period with a fixed model formulation and the retained observational data. For the ERA-15 reanalysis used in this study a T106L31 resolution was used to generate a global data set from 1979 to 1993. Apart from the horizontal resolution, the ERA-15 assimilation system is identical to the ECMWF operational system used between April 1995 and January 1996 (cf. Table 2.1).

In the present thesis, the data were interpolated on a regular longitude/latitude grid with 1 or 0.75° resolution, depending on the spectral resolution (cf. Table 2.1) and application.

2.2 Equivalent latitude

The availability of high-resolution hemispheric or global data sets makes it possible to calculate spatial and temporal derivatives as necessary for PV. The interpolation of PV on isentropic surfaces provides a potent perspective for the upper troposphere and lower stratosphere (see Section 1.3).

For climatological analyses it is often customary to calculate zonal means (as shown in Fig. 2.1a). A more physical approach is to average not along latitude but pseudo-conserved "material tubes" (McIntyre, 1980). PV contours on isentropic surfaces form pseudo-material tubes in an adiabatic frictionless flow. A new coordinate can then be created by labeling the PV value of each contour[1] to its "equivalent latitude", which is the latitude of the zonal circle that encloses the same area as the contour (Butchart and Remsberg, 1986). That is, if a parcel's PV value is Q, then its equivalent latitude is

$$\Phi_e = \sin^{-1}\left(1 - \frac{A(Q)}{2\pi r_e^2}\right),$$

[1]The methodology is not restricted to PV by any means. It could be also applied to another conserved tracer, e.g. θ on PV surfaces or even an observed atmospheric tracers constituent. It is however reasonable to choose a tracer that has a strong meridional and weak zonal variability.

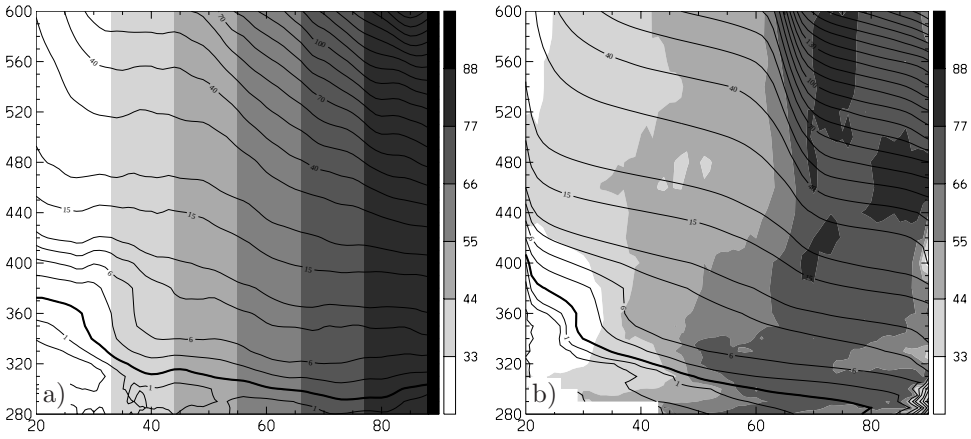

Figure 2.1: Geographical latitude (shaded in °N) and PV (contour lines of 0, 0.5, 1, 2, 4, 6, 8, 10, 15, 20 pvu, with 10 pvu spacing above and 2 pvu denoted bold) in (a) zonal mean and (b) equivalent latitude - θ representation on isentropic surfaces from 280 to 600 K (with 5 K spacing below 360 K and 20 K spacing above) at 00 UTC 01 March 2000.

where r_e is the radius of the earth and $A(Q)$ is the area enclosed by the contour of constant PV whose value is Q (cf. Sobel et al., 1997). If the contour is separated (e.g. cut-off cyclones), the area is computed by summing up including all "islands".

An extension of this concept considers also the vertical spacing of the isentropes (which results in a mass instead a horizontal area weighting), but revealed no significant enhancement (Nakamura, 1995). Another enhancement uses a selected PV contour collocated with the polar vortex edge preserving the meridional geometry polewards and relaxing it to geographical latitude towards the equator that tries to counter the strong PV undulation due to Rossby wave breaking in the surf-zone (Norton, 1994). This method requires an objective vortex edge definition and it is unclear how it can be applied in the absence of the polar vortex. Also, equivalent latitude itself has been used to define the polar vortex edge based on the PV gradient and wind velocity (Nash et al., 1996). Investigations by S. Buss, S. Hohl and the author indicate though a very limited objectivity since multiple edges are found regularly, in particular if using current high-resolution ECMWF analyses without smoothing.

As a demonstration for the concept of equivalent latitude, PV and geographical latitude are converted to equivalent latitude at a specific time instance (Fig. 2.1b). In comparison to the zonal mean counterpart (see Fig. 2.1a), PV increases polewards monotonically on each isentrope and regions of isentropic gradients (corresponding to steep PV contours) are enhanced noticeably. Geographical latitude converted to equivalent latitude though exhibits relatively low, partly even inversed isentropic gradients within the mid-latitudes due to the non-zonal alignment resp. strong meridional displacement of the PV contours (that are not necessarily disconnected from the main pool). The three-dimensional flow structure of this particular case is further discussed in Chapter 4.

2.3 Trajectories

The ECMWF analysis fields are further employed for the calculation of three-dimensional and isentropic trajectories using a tool developed by Wernli and Davies (1997) that follows a method introduced by Petterssen (1956).

Numerically, the finite-difference approximation of the trajectory equation $d\vec{x}/dt = \vec{u}(\vec{x})$ can be found by combining the Taylor expansions about the position at $t = t_0$ evaluated at $t = t_1$ and vice versa (Walmsley and Mailhot, 1983; Stohl, 1998):

$$\vec{x}(t_1) = \vec{x}(t_0) + \frac{1}{2}(\Delta t)\left\{\vec{u}(t_0) + \vec{u}(t_1)\right\} + \frac{1}{4}(\Delta t)^2\left\{\frac{d\vec{u}(t_0)}{dt} - \frac{d\vec{u}(t_1)}{dt}\right\} + \cdots .$$

The restriction to the first two terms is referred to as the "constant acceleration solution" and can be solved iteratively starting with

$$\begin{aligned}
\vec{x}_1(t_1) &\approx \vec{x}(t_0) + (\Delta t)\vec{u}(t_0) \\
\vec{x}_2(t_1) &\approx \vec{x}(t_0) + \frac{1}{2}(\Delta t)\left\{\vec{u}(t_0) + \vec{u}_1(t_1)\right\} \\
&\ldots \\
\vec{x}_i(t_1) &\approx \vec{x}(t_0) + \frac{1}{2}(\Delta t)\left\{\vec{u}(t_0) + \vec{u}_{i-1}(t_1)\right\},
\end{aligned}$$

where $\vec{u}_i$ is the velocity interpolated linear at $\vec{x}_i$. The identical result was obtained with a graphical approach by Petterssen (1956).

The accuracy of trajectory calculations, in particular in the presence of vertical motion as in the troposphere, is difficult to ascertain but has been addressed in several case studies (see Stohl, 1998, for a detailed review). Various numerous passive tracer experiments in the real atmosphere underline the high accuracy of trajectories calculated with analysed wind fields. The use of three-dimensional wind fields appear to out-perform the reduction to isentropes or isobars in the troposphere, whereas within the stratosphere, the computationally less expensive isentropic scheme is of similar accuracy (Stohl and Seiber, 1998). For the stratosphere, it is further recognized that the use of ECMWF analysed wind fields is reasonable in particular since the 4D-Var assimilation was introduced (see Section 2.1), and a high temporal resolution as 6 h improve the quality significantly (Knudsen et al., 2001). An inter-model comparison, including the one used hereafter, reveals a high consistency between the different implementations (Stohl et al., 2001).

2.4 Lagrangian techniques

The small scale structures of passive tracer distributions obtained by high-resolution measurements as satellite scans stand in opposition to the much coarser analysed tracer fields. Two techniques based on analysis fields try to counter this lack by generating structures of scales smaller than the resolution of the corresponding analysis fields: (i) the contour advection (CA) technique (Section 2.4.1) and (ii) the reverse domain filling (RDF) technique (Section 2.4.2). An extension of the latter as a powerful visualization technique of the Lagrangian flow is then introduced as Lagrangian Projection (Section 2.4.3). Methods to describe the kinematical history of air parcels are then introduced in Section 2.4.4.

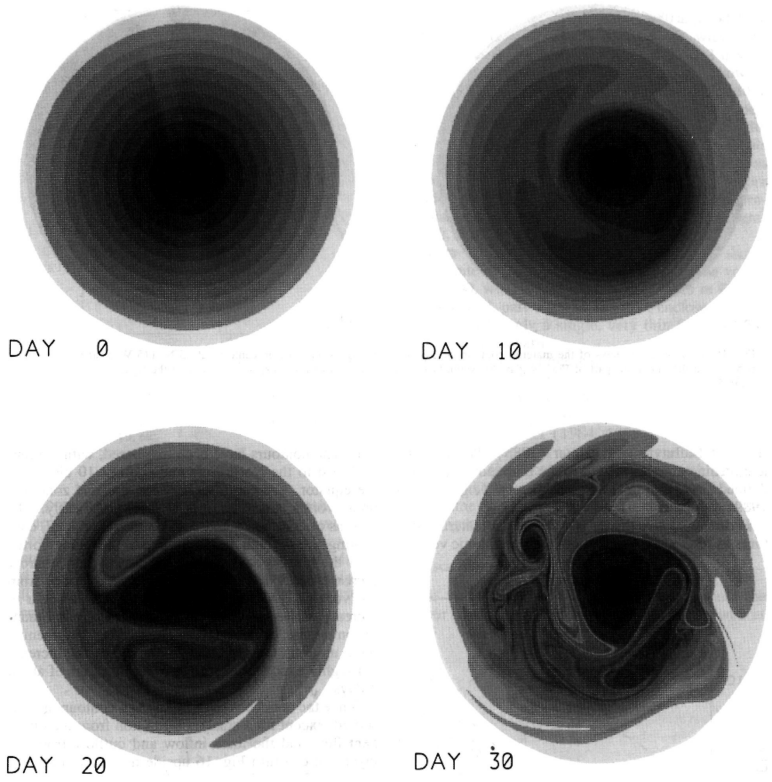

Figure 2.2: Contour advection results of Rossby wave breaking along the polar vortex edge in the northern hemispheric stratosphere for ten material contours showing days 0 to 30. The areas between contours have been shaded (from Norton, 1994).

2.4.1 Contour advection

The CA technique, as specified by Dritschel (1989), uses the wind field to advect isentropically an observed tracer or an analysed field as PV. Particles are placed along preliminary chosen contours, and then, at regular time intervals the particles are redistributed along the contours (using a local cubic spline). In sections of high curvature, more particles must be added. A "surgery" option discards filaments and other features finer than a preassigned scale. After an integration time of a few weeks, the resulting fields possess very rich small scale structures (Fig. 2.2).

The nature of Rossby wave breaking disturbing a vortex in a shallow water model was characterized with the advection of one contour in a shallow water model (Polvani and Plumb, 1992). For the stratosphere, Rossby wave breaking along the polar vortex edge is captured realistically employing the wind fields of a GCM simulation in Waugh and Plumb (1994) and independently for a shallow-water representation in Norton (1994). Comparisons to in situ measurements revealed good agreement (Waugh et al., 1994). On tropopause levels, CA of PV leads to filamentary structures similar to ones observed in satellite WV scans (Appenzeller et al., 1996). Investigation of the accuracy of CA on both tropospheric and stratospheric levels show that the displacement error of filaments is highly sensitive to the employed wind field resolution, whereas the stretching rates are quite robust (Methven and Hoskins, 1999).

While CA may provide a continuous and consistent view of the evolution of

tracer quantities, the results are shown to be of limited utility for slowly developing quantities, such as the area of the polar vortex (Baker and Cunnold, 2001). Beside the trajectory calculation, the CA technique depends on several tuning parameters, as the density of particles along the contours, the spline fitting technique and the surgery to counter too thin filaments. By default, it is restricted to quasi two-dimensional surfaces such as isentropes or PV surfaces and requires the specification of a tracer acting as a scalar marker, as PV or a chemical mixing ratio. This marker reduces the information about the origin from two to one dimension.

2.4.2 Reverse domain filling

An alternative to CA is the so-called RDF technique. It involves calculating the origin of tracers instead of their advection forward in time. From each grid point of a specified field or from an observational point a backward trajectory is traced in space and time using interpolated wind fields. The trajectories can then be used to advect a traced quantity from an earlier position to the location of the undertaken measurement generating a "high-resolution" tracer field.

Suitable tracers are measurable quantities as q, N_2O or ozone with an appropriate lifetime. Alternatively, PV is often employed as a virtual tracer. The fact, that PV is dynamically significant (i.e. it is linked directly with the flow dynamics) makes its structure much more meaningful with the flow field and less sensitive to the data assimilation process than a passive tracer as q. On the other hand, this results in the loss of small scale structures in a smooth smooth flow field (and temperature distribution). The three dimensional derivatives of the flow and temperature field for the calculation of PV cause an additional numerical smoothening.

For a single field the RDF approach is computationally less expensive than CA (Sutton et al., 1994). Sutton found that coarse-scale satellite observations of N_2O can be advected successfully to a regular grid of finer resolution using isentropic trajectories. Modified PV[2] derived from analysis fields has also been used as a tracer to reconstruct vertical cross-sections (Newman and Schoeberl, 1995). Good agreement was found between the enhanced fields and ozone measurements. Using three-dimensional trajectories of 7 to 8 days length, laminae in long-lived trace-gas profiles have been reproduced successfully around the developing polar vortex (Manney et al., 2000).

For the subtropical water vapour distribution, the reconstruction considering the minimum saturation along RDF trajectories (Pierrehumbert and Roca, 1998) and a similar study employing three-dimensional trajectories tracing relative humidity (Dessler and Sherwood, 2000) reveal a good agreement with satellite observations stressing the dominance of large scale advection also in the tropics.

The RDF approach differs intrinsically to CA. With the RDF technique no continuous evolution of a field can be represented, since for each time slice the fields have to be created independently calculating new trajectories. Also, the length of the integration time (i.e. backward trajectory length), is unclear and must be chosen subjectively. This parameter though may be adjusted for tuning after the integration. The surgery mechanism diffusing small scales for CA however is applied during the integration. The lack of a surgery mechanism in the RDF technique can be circumenvented by the "local gradient reversal"enhancement (Sobel et al., 1997).

[2]The so-called Lait-PV is scaled with a factor depending on θ to reduce its increase in the vertical (Lait, 1994).

This technique permits the quantification of transport similar to CA.

RDF is not restricted to an isosurface of a conserved quantity, as θ or PV, the technique can be applied to any structure in the observed fields such as along flight tracks, soundings or horizontal cross-sections in an arbitrary chosen coordinate. The desired resolution can be chosen in space and time in advance allowing to create gridded fields.

Depending on the characteristics of the flow and the length of the integration time, the RDF fields can exhibit structures of much smaller scales than the original analysed data. The reliability though is strongly limited due to non-conservative processes (e.g. precipitation or turbulence for WV) Within the stratosphere, isentropic RDF calculations advecting PV have been employed successfully with integration times of up to 10 days (Schoeberl and Newman, 1995).

At tropopause levels, the time scale of the modification processes is in the order of 24 h. Therefore, a trajectory length of typically 24 h is chosen herein.

The measure of success of CA and RDF relates to within the nature of chaotic advection in upper tropospheric and stratospheric levels. Chaotic advection is characterized by regular[3] and time dependent Eulerian velocity fields that yield to small scale tracer structures resp. chaotic particle trajectories (Aref, 1984; Ottino, 1989). Although the resolution of the wind fields is coarser than the observed tracer structures, the wind fields can be used for the calculation of trajectories to generate these structures.

2.4.3 Lagrangian Projection

An extension of the RDF technique can be obtained, by the application of the RDF technique to non-conserved quantities (e.g. pressure) or geographical markers (e.g. longitude). The advection itself is then carried out taking into account full physics by the use of three-dimensional non-adiabatic trajectories. This makes it possible to relate the Lagrangian historical dynamical development to Eulerian atmospheric structures. This novel analysis technique is referred to as "Lagrangian Forward Projection" (LFP, cf. Liniger and Davies, 2003).

The analogous procedure applied to forward trajectories putting the future development into the context of an earlier Eulerian field would be referred to as "Lagrangian Backward Projection".

2.4.4 Parcel dispersion

Paths of selected air parcels (referred to as "spaghetti diagram" Haidvogel and Halloway, 1984) or the position of many air parcels at a certain time (as by Kida, 1977; Sutton, 1994; Bowman and Chen, 1994) can be used to describe the kinematical history. As alternative, the change in geographical position (absolute or relative to neighboured trajectories) can be described with a single parameter as realized for Lyapunov exponents, absolute and relative dispersion (Provenzale, 1999) that are introduced in the following subsections. All the three quantities are based on measuring the distances between the positions of an ensemble of advected parcels.

[3] i.e. smooth with respect to the resolution or tracer structures

In analogy to LFP, such a value can be shown at the position of the trajectory initialization.

Lyapunov exponent

Originally a metric parameter for phase space studies, this quantity measures the mean exponential growth rate of the trajectory divergence to its infinitesimally closely surrounding trajectories by a limes in time to infinity (Lyapunov, 1907; Lichtenberg and Lieberman, 1992):

$$\lambda = \lim_{t\to\infty} \max_{i\neq j} \frac{1}{t} \log \frac{|\vec{x}_i(t) - \vec{x}_j(t)|}{|\vec{x}_i(0) - \vec{x}_j(0)|} \ .$$

Two linked problems arise in its application to the physical space: (i) data resolution limits a priori the initial specified distance from being chosen very small[4] and (ii) the limitation by the sphericity of the Earth prohibits a limes in time to infinity.

A possible way to counter these restrictions is the use of the largest growth of the eigenvalues of the deformation matrix along the trajectory. An example was outlined for an application to isentropic trajectories in the lower stratosphere by Pierrehumbert and Yang (1993). An alternative approach is the "pull-back" method (Lichtenberg and Lieberman, 1992) and adopted to atmospheric trajectories by Ngan and Shepherd (1999): When the distance from the investigated "central" trajectory to the originally neighbored ones exceeds a certain value, the neighbored trajectories are discarded and new ones are started close to the central one.

A Lyapunov exponent is a powerful statistical quantity to quantify chaos and hence it is widely used in fluid dynamics. In this study however, it is intended to examine individual values with respect to their geographical location and dynamical regime Thus, both of the approaches outlined above rise concerns: (i) only the local character of the field around the central trajectory is described, (ii) a non exponential growth with increasing time might not be captured and (iii) the neighbored trajectories are not retained and this would be desirable in regard to transport processes.

Absolute dispersion

Absolute dispersion (also called single-particle dispersion) provides a measure of the root mean square displacement of individual parcels in the time interval $[t_0, t]$ for an ensemble of N parcels:

$$A(t, t_0) = \sqrt{\left\langle |\vec{x}_i(t) - \vec{x}_i(t_0)|^2 \right\rangle_N} \ ,$$

with

$$\langle X \rangle_N = \frac{1}{N} \sum_{i=1}^{N} X \ .$$

[4] For phase space integrations the initial distance is usually limited only by numerical truncation of the model

Thereotically, the members of the ensemble should be initialized at infinitesimal distance in different realizations of the same flow. In practice however, the parcels are often seeded with different spatial positions of the same time and this is compatible if the initial separation is large enough.

Absolute dispersion can be used for micro scale processes in the troposphere (such as plume dispersion). For $t \gg 0$, absolute dispersion though is very sensitive to anisotropy of the background flow and this limits potential applications for atmospheric flows of synoptic to global scales.

Relative dispersion

Relative dispersion is defined analogously as the root mean square of the distances between the parcels at time t from the mean position of the ensemble (see Fig. 2.3):

$$D(t) = \sqrt{\left\langle |\vec{x}_i(t) - \langle \vec{x}(t) \rangle_N|^2 \right\rangle_N}$$

In contrast to absolute dispersion, this measure is invariant under a Galilean transformation and the controlling dynamic mechanism is essentially local, i.e. it is controlled by dynamical structures of similar length scale as the distance between the particles (Er-El and Peskin, 1981).

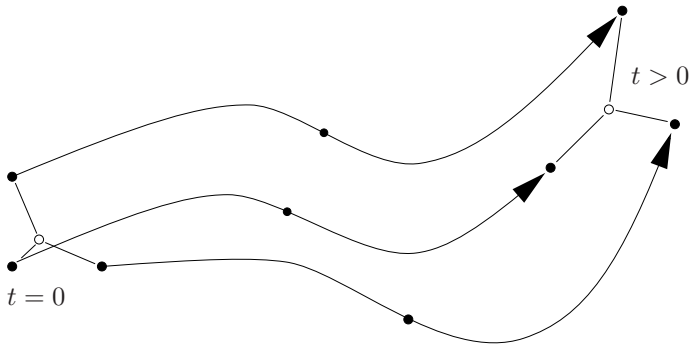

Figure 2.3: Illustration of relative dispersion for an ensemble of three parcels. Positions $\vec{x}_i(t)$ are denoted by dots, mean positions $\langle \vec{x}(t) \rangle_N$ by circles.

The initial distance between the parcels strongly influences the value of $D(t)$. To counter meridional variations in applications to trajectories initialized on a regular lon/lat grid, the relative dispersion can be weighted by its initial value. In analogy to the Lyapunov exponent, the logarithm is then taken yielding to the quantity that is hereafter referred to as "dispersion":

$$\sigma(t) = \log \frac{D(t)}{D(0)}. \tag{2.1}$$

For infinitesimal initial distances one can relate $\lim_{t\to\infty}(\sigma/t)$ to the Lyapunov exponent in physical space (Maryon and Buckland, 1995; Provenzale, 1999).

In global transport studies often the meridional relative dispersion D_y is investigated, i.e. considering only of dispersion in latitude (Bowman and Chen, 1994; Sutton, 1994; Ngan and Shepherd, 1999). For synoptic time scales however, the

non-zonal alignment of the jet-stream and the polar vortex edge limits the ability of the meridional dispersion to describe the local dynamics (Sutton, 1994).

The spherical distance | | is used in this study, as outlined in Appendix A.1 and the trajectories are initialized on a regular lon/lat grid of 0.5° spacing. An ensemble of three trajectories that initially form a triangle (see Fig. 2.3) is usually chosen and the resulting dispersion value is assigned to the trajectory initially positioned at the equatorward western edge that is the nearest to the mean position. Larger ensemble numbers would result in smoother structures. The same can also be obtained by a spatial smoothening of the distribution derived from a small ensemble.

Diffusion

In the case of Brownian motion, relative dispersion of constant growth can be related to a relative diffusion coefficient (Einstein, 1905)

$$K = \frac{D^2}{2t} \ ,$$

and applied to atmospheric flows by Richardson (1926). A more general formulation for a non-constant growth is given by (Richardson, 1948)

$$K = \frac{1}{2}\frac{\partial D^2}{\partial t} \ .$$

Based on this equation, Lagrangian models can be used to determine a pseudo-tropospheric synoptic diffusion. A high sensitivity on the trajectory length is found that has been attributed to different dynamical regimes (Maryon and Buckland, 1995; Pudykiewicz and Koziol, 1998). The use of meridional relative dispersion reveals also a strong meridional sensitivity (Bowman and Chen, 1994).

2.5 DIAL measurements

The airborne differential absorption lidar (DIAL) technique offers an opportunity to measure water vapor mixing ratios in the lower-most stratosphere with a very high resolution. Basically, the instrument measures the backscatter of laser pulses emitted into the atmosphere at two adjacent wavelengths. One wavelength is centered on an appropriate water vapor absorption line ("on-line") and the second non-absorbing wavelength is selected for the reference measurement ("off-line").

The new, patented DIAL system that measured the data used for this study has been developed and was operated by the Lidar Group and the Insitute of Atmospheric Physics of the Deutsches Zentrum für Luft- und Raumfahrt (DLR). A detailed description of the DIAL technique in general and of the DLR-system is given in Poberaj (2001) and summarized in Appendix B.

2.6 Satellite scans

Data of coarser resolution but covering a larger area are taken routinely by EUMETSAT's Meteosat-7 satellites from the geostationary orbit about 36′000 km above the

equator and Greenwich meridian (Schmetz and Turpeinen, 1988; Eumetsat, 2001). The images are taken on a half-hourly basis and provide data on three bands:

A visible band (VIS) with a spectral range from 0.45 to 1.0 μm is available for daylight.

The infrared band (IR) in the range 10.5 to 12.5 μm corresponds to peak re-emission of radiation from the Earth's surface and atmosphere, according to their temperature. The atmospheric gases are, as with the VIS band, fairly transparent in this region.

A water vapour absorption band (WV) covers $5.7 - 7.1\,\mu$m and determines in effect the amount of water vapour in the upper troposphere. The WV channel represents an absorption measurement of terrestrially emitted radiation by the WV absorption band. This means that radiation from lower levels is absorbed by the WV in the layers above which according to the radiation laws (Kirchoff) become radiating surfaces themselves. Contribution functions describing the region of the atmosphere from which the radiation originates peak between 7 and 9 km ASL with a half-width of about 5 km, varying with temperature, humidity profiles and viewing angle (Poc et al., 1980; Fischer et al., 1981). With ancillary parameters as temperature profiles from other sources (i.e. model output) the upper tropospheric humidity field can be estimated (Schmetz and Turpeinen, 1988). Following Poc et al. (1980), the measured radiance in WV scans should correspond to the vertically integrated analysed q from around 600 hPa upwards.

Some theoretical studies also point out the proportionality to the temperature distribution on the $\rho_{H_2O} = 75\,\mathrm{mg/m^3}$ isosteric surface (i.e. constant q density) in cloud free regions (Ramond et al., 1981; Soden and Bretherton, 1993). Some applications in Appenzeller et al. (1996) exhibit promising results.

Meteosat-7 scans the full earth disc in 2500 lines of 2500 pixels for WV and IR giving a resolution of ca. 5 km at the sub-satellite point. The VIS detector operates with double resolution. The data used hereafter is labeled to be of good quality.

The satellite scans are available in a polar-stereographic projection covering Western Europe. For a comparison with other data sets, some of the satellite images are converted to a Cartesian grid, as outlined in Appendix A.2.

Chapter 3

Two Detailed Case Studies

Synoptic-scale variability at the extratropical tropopause is strongly linked to underlying weather systems and in particular to cyclones and anticyclones. Their upper-level structures can take the form of undulations of the tropopause, large amplitude meridional excursions on isentropic surfaces, vertical intrusions from the stratosphere into the troposphere and vice versa extrusions from the troposphere into the stratosphere.

In the present chapter two case studies are presented that characterize such structures – (a) downward and southward stratospheric intrusions and (b) upward and northward tropospheric extrusions over Europe (Section 3.1 resp. 3.2). The resulting analyses provide the rationale and platform for the characterization of their kinematical Lagrangian structure (Chapter 4) and the development of a 15 year climatology of certain features (Chapter 5).

3.1 Sub-structure of a stratospheric intrusion

3.1.1 The streamer project of the Mesoscale Alpine Programme

In the framework of the recent Mesoscale Alpine Programme (MAP) significant effort was devoted to the investigation of stratospheric intrusions. Initiated in 1996 with support from an international consortium of science agencies and weather services, the overall aim was to improve weather prediction in the Alpine area (Bougeault et al., 1998). The specific objectives were geared to achieve a better understanding of the interaction of atmospheric flows with the Alps and it was divided into two main components. A "dry" part focuses on unbalanced phenomena like Föhn and Mistral, whilst the "wet" part was designed to examine severe precipitation events and associated flash floods on the Alpine south-side.

MAP culminated in a large field-measurement campaign over the Alpine region in autumn 1999 – the Special Observation Period (SOP). The SOP itself was divided into Intensive Observation Periods (IOPs) dedicated to selected projects, as overviewed by Bougeault et al. (2001).

One of eight projects focussed on the role of stratospheric intrusions. The typical, fully developed form of an intrusion on an isentropic surface is a southward elongated and slender structure of stratospheric air, also referred to as a stratospheric streamer (Appenzeller and Davies, 1992) and identifiable as an upper-tropospheric positive PV anomaly. It is associated with southward advection on its western side

and northward advection on its eastern side. The typical length is about 2000 km in the north-south and 200 km in the east-west direction. In the vicinity of and within a streamer meso-scale sub-structures can be discerned (e.g. from satellite scans or lidar) or inferred using contour advection calculations based upon coarser-scaled analysed data (Appenzeller et al., 1996).

Streamers are related to numerous atmospheric processes and anomalies. The isentropic and southward displacement of cold air with high PV is linked to cyclonic vorticity and the associated enhanced gradients in temperature can lead to a strong baroclinicity on the streamers flanks Also the break-up of streamers is associated with significant amounts of STE. Strong exchange was related to diabatic and turbulent effects due to a strong cloud cell at the streamers eastern flank (Bourqui, 2001). During the decay of a cut-off radiative processe were identified (see Section 1.1 for further references).

Streamers in the vicinity of mountains can be related to intense rainfall events (Massacand et al., 1998; Morgenstern and Davies, 1999), and there are indications that the filament's sub-structure can exert a significant influence upon this process (Fehlmann et al., 2000; Fehlmann and Quadri, 2000).

The array of separate and interrelated dynamical and chemical processes are are not yet fully understood and is complicated by the interplay of a wide range of scales and the lack of detailed measurements. However the combination of specialized high-resolution measurements obtained during a field programme with state-of-the-art operational analysed fields can help provide insight into the structure and the associated dynamical processes. Earlier studies of this kind used in situ measurements of ozone and other quantities (Danielsen, 1968; Danielsen et al., 1987), radiosonde data (Vaughan et al., 1994), a ground based ozone lidar (Eisele et al., 1999) and a temperature Raman lidar and a stratosphere-troposphere radar measuring temperature and horizontal wind (Ravetta et al., 1999). The present study seeks to build on these investigations with a special focus on the humidity field and techniques that help enhance the analysis data.

3.1.2 Dataset

A case study approach is adapted here to examine an upper-level elongated PV structure that translated over western Europe during the 15^{th} IOP of MAP from 00 UTC 5 November to 00 UTC 10 November 1999. It was selected for an investigation in the framework of the upper tropospheric PV anomaly project of MAP and the DLR aircraft Falcon undertook a mission on 6 November, providing a high-resolution vertical section of WV near the tropopause across the PV streamer. In addition Meteosat WV and IR satellite scans and T319L60 analysis data, interpolated to a 0.75° grid, are available. There were indications (ECMWF, 2001) that the humidity fields of the operational analysis and forecast fields from 12 October 1999 to 10 April 2000 were seriously affected by erroneous moisture, in particular in the shallow layer above the tropopause. Therefore in this study data from a special research experiment is used excluding this error (class RD, code E12E).

In the succeeding sub-section a synoptic overview is presented of the dynamical processes during IOP-15 (Section 3.1.3). Then, the DIAL measurements are examined and compared to the ECMWF data including RDF trajectory calculations undertaken in the attempt to reconstruct smaller scale structures (Section 3.1.4). In addition, WV satellite scans provide data to complement the inferences

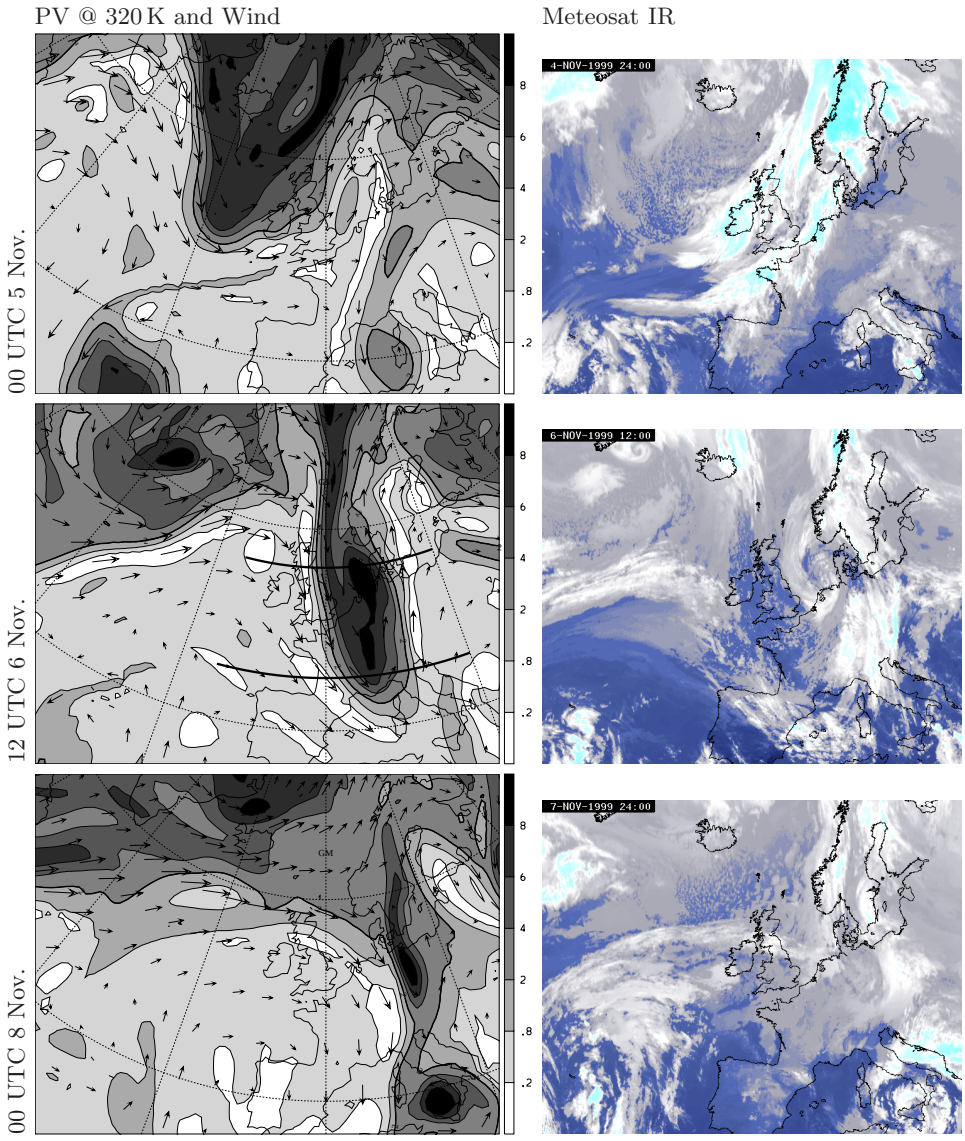

Figure 3.1: PV distribution (shaded in pvu) and wind vectors on the 320 K isentrope (left panels) and Meteosat IR channel (right panels) at 00 UTC 5 November (upper panels), 12 UTC 6 November (middle panels) and 00 UTC 8 November 1999 (lower panels).

regarding the horizontal structure (Section 3.1.6). Extensive trajectory calculations are conducted for the main phase on 6 November to further illuminate the observed structures and infer deductions on the nature of cross-tropopause transport (Section 3.1.7).

These results and interpretations are based on a preparatory work Liechtenstein (2000) and form the basis for a contribution to Project P2 of the MAP (cf. Liniger and Davies, 2003). It is a pleasure to acknowledge and thank the DLR and in particular Klaus-Peter Hoinka for the supply of the DIAL data.

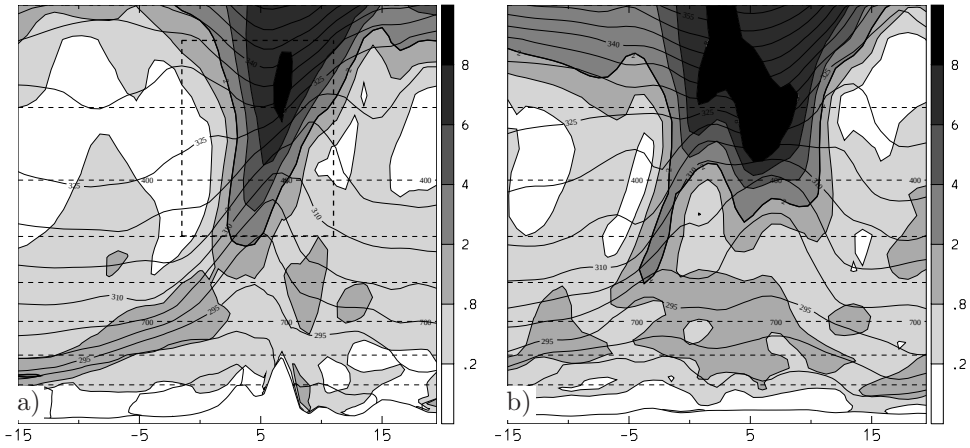

Figure 3.2: Cross-sections of PV (shaded as in Fig. 3.1) and θ (solid lines with 5K spacing) at 45°N (a) resp. 56°N (b) along bold lines in Fig. 3.1b). Dashed square in (a) denotes the region covered by the DIAL and dashed lines isobars with a spacing of 100 hPa.

3.1.3 Overview of synoptic evolution

During the period of 5 – 8 November 1999, a wide trough extended over the eastern North Atlantic and there was an associated strong front on its eastern border (Fig. 3.1a). The trough translated south-eastwards and was situated over southern France on the 6 November with a large cloud free area along its western flank (Fig. 3.1b). The PV maximum over Denmark is evident as a spiral structure in the IR and WV-satellite scan (see also Fig. 3.17). This is the stage selected for the Lagrangian investigation and comparison with measurements.

Subsequently, the streamer breaks up into two cut-off anomalies (see Fig. 3.1c), a process which is often related to the phenomenon of "Alpine Lee Cyclogenesis" and the southern anomaly as "Genovesian Cyclone". Early investigations on this topic were carried out by Ficker (1920), a PV perspective is given by Bleck and Mattocks (1984) and a detailed review in Schär (1989).

The northern cut-off subsequently reconnects to the stratospheric pool on the 9 November and has only a weak signal in surface pressure. The southern cut-off slowly disintegrates over the Mediterranean Sea and is collocated with a strong surface pressure minimum from the 7 November onwards.

Precipitation occurs in the east of the streamer as the front impinges upon the western Alps in the morning of the 6 November. Later, precipitation is found on the Alpine south-side near Locarno, in the Po valley, and in the eastern part of the Alps in Austria and Slovenia (till the morning of 7 November). During the decaying phase of the southern cut-off, from the 7 November onwards, precipitation occurs at the northern coast of Africa, south of and over southern Italy with a maximum towards Greece.

The overall evolution resembles very much the upper-level precursor described in Massacand et al. (1998), but the precipitation found south of the Alps was not anomalously intense.

3.1.4 Vertical structure at main stage of streamer

Strong horizontal gradients and high values in upper level PV and attendant diabatic processes imply a strong anomaly also in the vertical at the main stage, 12 UTC 6 November, and prompt the examination of vertical cross-sections in the analysis data. A cross-section at 45°N reveals that the upper-level structure is associated with a tropopause fold that has descended to 500 hPa (Fig. 3.2a) with a weaker PV prolongation extending down to 900 hPa and slanting strongly westwards. The near separation of the low level extension below 600 hPa makes it unclear how far it is linked directly to the upper level anomaly. The temperature front collocated with the Alps corresponds to a strong zonal baroclinicity in mid-levels and to reduced vertical stability in upper levels east of the fold. Consistently, the positive low-level and negative upper-level PV anomalies east of the Alps are expected to be diabatically induced.

To the north, the fold narrows to about one grid-point at the latitude of Denmark as illustrated in the cross-section at 56°N (Fig. 3.2b). East of the fold, the upper-level cyclone corresponding to the spiral structure is represented by a relatively broad positive PV anomaly. The weak upward deflection of the isentropes in the lower levels corresponds to the weak surface signal of this cyclone. On all levels, the baroclinicity is much weaker.

3.1.5 Streamer's subsynoptic structure

The resolution of the ECMWF fields only allows partial identification of meso-scale features that can be observed by high resolution measurements such as the lidar. In addition, the analysis (and forecast) fields can strongly differ from observations. On the other hand, the physical consistency and the spatio-temporal coverage of the analysis fields provide a basis for sophisticated diagnostics facilitating the measurement's interpretation.

Here, DIAL q data in the lower stratosphere is compared to the overall, large scale structures in ECMWF analysis and forecast fields, also employing the RDF and LFP techniques (see Section 2.4.2 and 2.4.3).

DIAL measurement across the tropopause fold

The DIAL measurements were performed over southern France with an aircraft flying eastwards from 14.45 UTC to 16.00 UTC at the same latitude and day as discussed above (see also Fig. 3.2a). The data covers a vertical slice from 1.5°W to 12°E ranging from 10.6 down to 5.5 km ASL in the center of the fold (shown e.g. in Fig. 3.3).

The DIAL data exhibits a dry intrusion reaching down to mid-tropospheric levels (6 km ASL) with a westward tilt (Fig. 3.3). The lower tip of the intrusion is folded westwards below air with higher q (around a height of 7 km ASL and 4.5°E).

Significantly different structures are found between the streamer's western and eastern flanks, i.e. for the regions west and east of 5°E: The tropopause at the western side of the fold is characterized by weak vertical gradients in q, in particular between 2 and 3.5°E. East of 6°E, strong vertical gradients are found, with meso-β scale disturbances.

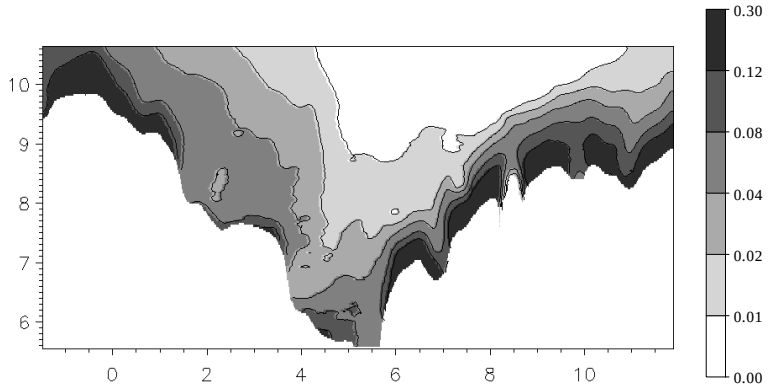

Figure 3.3: Longitude (°E) – height (km) cross-sections of specific humidity (g/kg) measured by DIAL lidar.

These observations prompt various questions that are tried to answer in the following subsections: Are there analogous structures detectable or indicated in ECMWF fields and satellite scans? What processes are related to the strong gradients and mesoscale disturbances at the streamer's eastern flank? Is the region of weak gradients at the western edge of stratospheric or tropospheric nature? What is the origin of the air within the folds lowermost tip and its surrounding, in particular the humid air masses located above the tilted fold around 4°E? Is it possible to deduce estimates for the accuracy for the measurements or the ECMWF fields?

Comparison to ECMWF fields and satellite scans

There are notable differences if comparing the ECMWF analysis at 12 and 18 UTC with the DIAL q field (Fig. 3.4a and c). At 12 UTC, the intrusion in ECMWF analysis is located more to the west than in the DIAL data and 6 hours later, the lower-most part of the intrusion is connected just weakly to the upper part. The discrepancy might in part be attributable to the differing time frame, and to explore this aspect, the two analysis fields are first interpolated linearly in time to 15 UTC (Fig. 3.4b). The resulting field resembles the 18 UTC analysis, except for the western part around 3°W, but is not closer to the DIAL measurements.

The rich spatio-temporal scale of the q distribution including the order of magnitude difference across the tropopause and the high wind velocities at that level limit the validity of the foregoing interpolation procedure. Indeed, the 3 hour forecast field for 15 UTC (Fig. 3.4d) is much more similar to the DIAL pattern with regard to the structure and amplitude at the western flank and the connection to the lowermost part of the intrusion. Also below the range of the DIAL, a very dry elongation of the fold is found in the forecast, that is much less pronounced in the analyses fields. In all ECMWF fields, the vertical q gradients are located lower in height and weaker than observed by the DIAL.

In the western part, the position of the PV tropopause is in agreement to the DIAL data inside the fold and overlap, precisely at the edge near 4°E (Fig. 3.5a). However, the low vertical gradients in the DIAL data between 2 and 3.5°E can not be found in the PV structure and is marked to be of tropospheric nature by low PV values. In the DIAL RH field[1], there is hardly no vertical gradient in this part (Fig.

[1]for the calculation pressure and temperature are employed from the ECMWF forecast

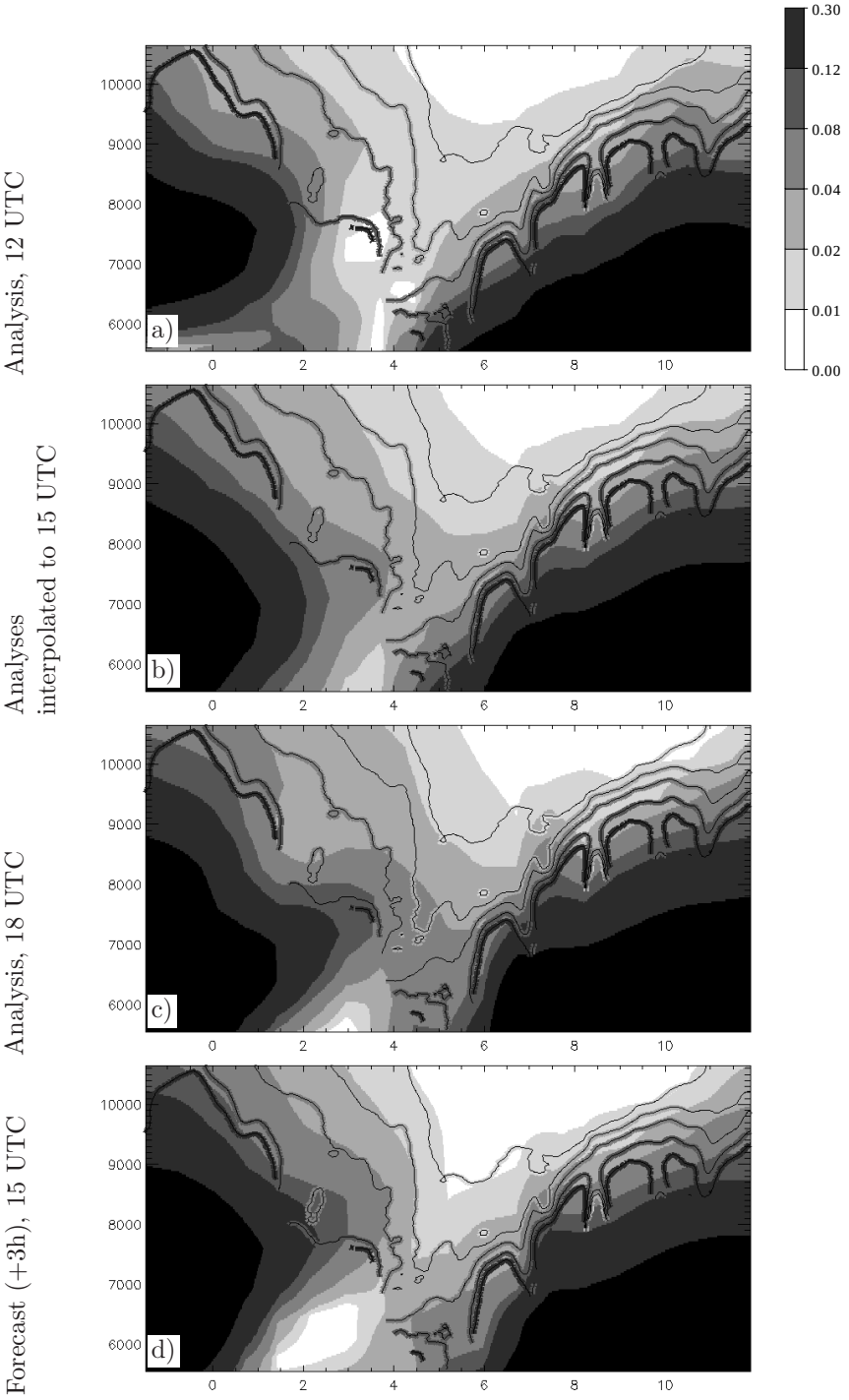

Figure 3.4: Longitude – height cross-sections of ECMWF analysis fields (shaded in g/kg) at (a) 12 UTC 6 November, (b) interpolated to 15 UTC and (c) 18 UTC, and (d) the 3 hour forecast for 15 UTC. Overlaid is specific humidity measured by the DIAL (coloured contour lines as in Fig. 3.3).

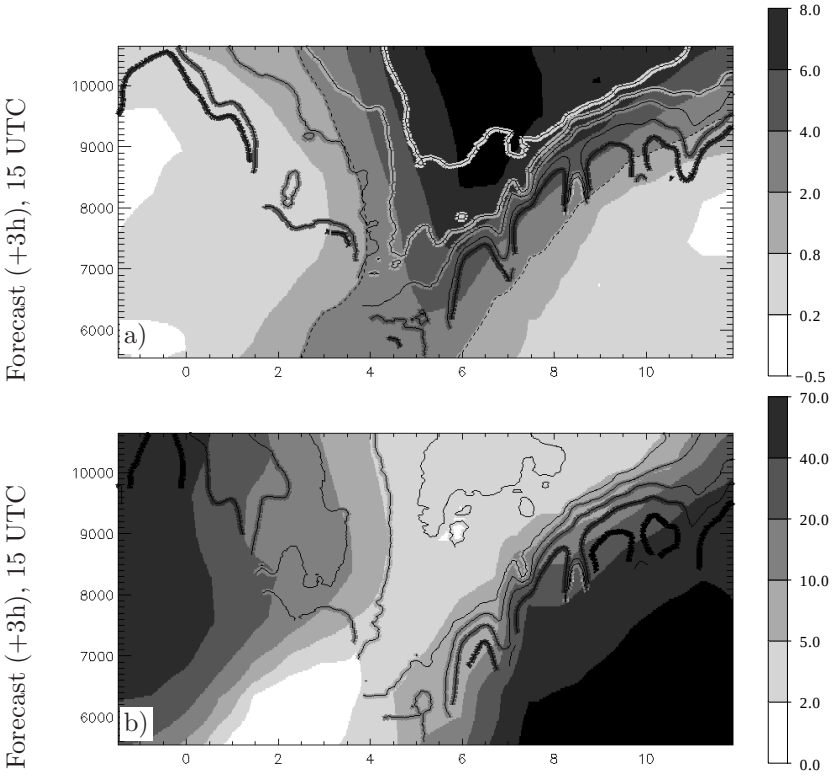

Figure 3.5: Longitude – height cross-sections of ECMWF 3 hour forecast for 15 UTC of (a) PV (shaded in pvu) and (b) RH (shaded in %). Overlaid is specific humidity measured by the DIAL (coloured contour lines as in Fig. 3.3).

3.5b). The satellite scans consulted along the same cross-section reveal low humidity (at the absence of clouds) making the western tropospheric region indistinguishable from the fold (Fig. 3.6). Theses feature can only be explained by the presence of anomalous high temperature in the upper troposphere, also indicated in the θ distribution (see Fig. 3.2a). The different temperatures in the region of maximal WV radiation compensates the horizontal gradient in humidity for the WV satellite scan.

East of the intrusion, a disparate tropopause structure is apparent between q, PV and the RH field from the ECMWF data and the observations (Fig. 3.5). The ECMWF fields exhibit a different location and weaker vertical gradients. Further, meso-scale sub-structures in the DIAL data cannot be detected. The radar observations in the Po valley indicate convective systems below the eastern part in a region between 8 and 10°E (not shown), that is processes that are not fully resolved by the ECMWF model.

The presence of local convection is confirmed by satellite data consulted along the same cross-section (Fig. 3.6) that show low cloud top temparatures and high humidity between 8 and 10°E. The meso-scale disturbances observed by the DIAL at 7 and 11°E can be identified in the IR scan by a lower cloud top and in the WV scan by drier air. In the visible channel denotes the anomaly at 7°E, but not at 11°E. The two local minima in humidity and cloud height indicate the edge of convective cells. Note, that the Alpine ridge is also located between 6 and 7°E. All mentioned features in the satellite data persist for several hours, partly propagating slowly eastwards (not shown). The DIAL disturbance at 8.25°E is not found in the

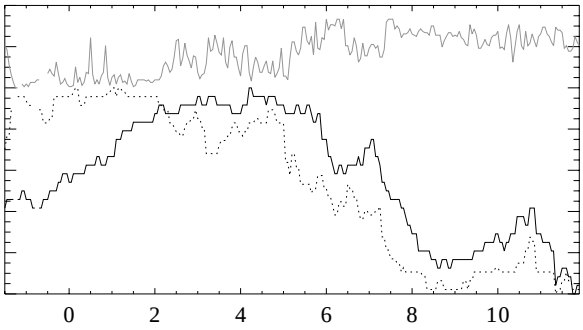

Figure 3.6: Water vapour (solid line), infrared (dotted) and visible channel (grey) satellite data along DIAL cross-section (arbitrary units, high values correspond to low q, high cloud top temperature resp. brightness) at 15 UTC 6 November along DIAL cross-section.

satellite data and the one at 10°E has only a very weak signature. The lowest cloud top temperature and maximum radar reflectivity are collocated near the center of the convective region at 8.25°E.

The convection seems to strengthen the vertical humidity gradients and induce meso-scale disturbances by diabatic heating or dynamically by the strong updrafts associated with the convection. The resolution of the ECMWF fields inhibits an appropriate representation of these partly parameterized, sub-grid scale processes.

On the other hand, parts of the differences in the eastern region could be related to an error in the DIAL by (i) anomalous atmospheric density, that is used for the calculation of the mixing ratio, or (ii) high aerosol concentration, disabling the assumption of dominating molecular scatter (see Section B.1). The most eastern dropsonde measuring the density (resp. temperature and pressure) was dropped at 4.5°E. It is therefore not unlikely that inaccurate temperatures in the eastern region also due to diabatic heating and radiative cooling aloft, have been used, but they induce only a small error, since the sensitivity by the DIAL to temperature errors is rather small, i.e. a deviation of 2 K at 8 km height results in an error of $1.5\% H_2O$ (see Poberaj, 2001, for details).

The reliability of the DIAL data is also reduced since the backscatter ratio exhibits very high aerosol concentrations east of 6°E at tropopause levels. The strong updrafts due to the convection cells raise the aerosol concentration at the top of the cells strongly. Thus, the tropopause disturbance in the DIAL data around 8.25°E and at 10°E could be due to the assumption of molecular scattering leading to a significant disagreement. The disturbances at 7 and 11°E are both identifiable in the backscatter ratio by weaker aerosol concentrations and so more reliable.

RDF reconstruction of small scale features with ECMWF data

As noted earlier, the available ECMWF analysis and forecast fields have a horizontal resolution of 0.75° (i.e. 59 km at 45°N) and are of limited usefulness in a direct comparison with features observed by the DIAL instrument with 1.8 km horizontal and 30 m vertical resolution. Under the assumption, that a large portion of the meso-scale features is produced by the synoptic and global scale flow, the RDF trajectory technique offers a way to reconstruct the unresolved resp. diffused meso-scale features (Sec. 2.4.2).

To this end backward trajectories of 75 h length are initiated at every DIAL data point tracing q and PV. For the first 3 h, the forecast fields are used and after that the analysed ones with a temporal resolution of 6 h.

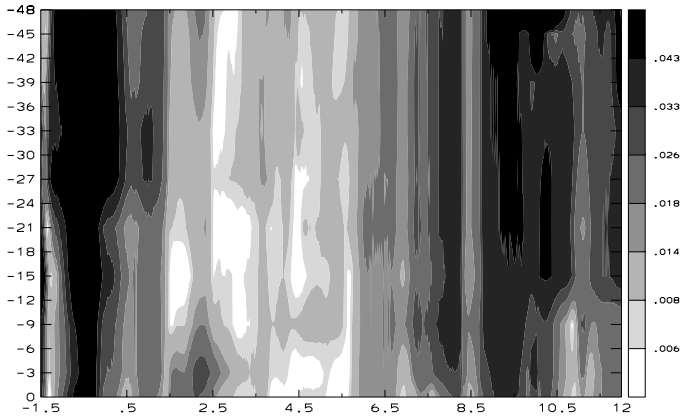

Figure 3.7: Absolute difference between measured and reconstructed q vertically averaged per longitude and trajectory length t_{RDF} in g/kg.

A quantitative comparison is made to derive a crude estimate for an optimal trajectory length t_{RDF}. For comparability between the q field observed by the DIAL and the reconstructed RDF fields, absolute differences per longitude and time (averaged over the vertical column) are calculated and shown in Fig. 3.7 as a function of t_{RDF}. Relative minima occur between 15 h and 21 h. Using short trajectories to the nearest analysis time ($t_{RDF} = -3$ h) partly produces a stronger difference than both the initial time (resp. forecast) and longer integration times.

The error is strongly dependent on the longitudinal position. Between 1°W and 5°E, the error is overall small with a miminum around $t_{RDF} = -15$ h. East of it, the difference in the vertical gradients raises the error substantially and better accuracy is achieved for $t_{RDF} = -9$ h. The band of temporal constant error around 8.5°E is a result of the previously discussed small scale disturbance. The non-conservative processes at the eastern flank obviously shorten the optimal trajectory length and limit the success of RDF.

Considering the q field for trajectory length $t_{RDF} = -15$ h in Fig. 3.8, the upper stratospheric part does not change much both in terms of amplitude and structure being consistent with quasi-adiabatic nature of the flow in the lowermost stratosphere. The smoother, less differential advection would allow much longer trajectory lengths.

Near the lower range of the DIAL though, the RDF result in significant changes. The region of low vertical gradients west of the intrusion now matches the observed field better. The fold's dry center below the height of 7.5 km matches the DIAL observation very realistic. Outside the range of the DIAL, the dry anomaly at 7 km height in the ECMWF data (see Fig. 3.4d) vanishes indicating this air mass is not of stratospheric origin, but diabatically dried.

East of the intrusion though, two layers underneath the tropopause must be considered separately. In the layer in the vicinity of the tropopause, the humidity increases backward in time. In terms of geographical position and pressure, this air shows a distinctively different behavior from the underlying air. It originates from upper levels and is likely to be subject to diffusive mixing in the jet-stream region

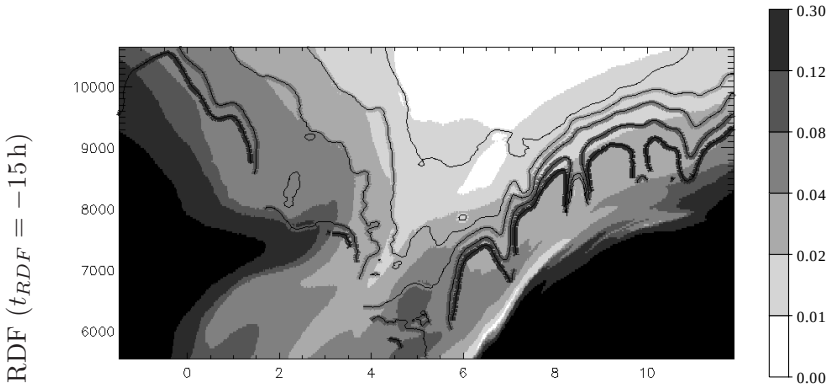

Figure 3.8: The same as Fig. 3.4d) for RDF reconstruction of q based on forecast and analysis fields with a trajectory length of $t_{RDF} = -15$ h.

along the western flank of the streamer. High variability in traced q and PV also indicate the likelihood of interpolation errors (not shown). The underlying, more humid air masses though originate from the boundary layer in the Eastern Atlantic and are subject to strong diabatic effects over the Gulf of Biscay (see also Section 3.1.7).

Although PV is not comparable quantitatively to q measurements, its quasi-conservative character (see Sec. 1.3) imply its usefullness for the RDF technique (Fig. 3.9). For coherency and robustness, the same trajectory length ($t_{RDF} = -15$ h) is used. In comparison to the cross-section from the forecast data (Fig. 3.5a), the PV structure within the region covered by the DIAL is strongly enhanced, particularly in the lowermost part of the intrusion and the western region of low vertical gradients (see also comments in Section 2.4.2).

Restriction on analysis fields for the RDF reconstruction

Measurements are not all carried out at analysis times and hence interpolated analysis fields can be used, but are usually not able to reproduce tracer structures appropriately (see Fig. 3.4b). As presented above a better agreement is found by the adaption of forecast fields, if available, for the approximate time of the observations (see Fig. 3.4d).

Alternatively, the RDF technique allows the reconstruction of tracer structures between analysis times by advecting quasi-conserved tracers by wind fields derived from interpolated analysis fields to the time and location of observation (Fig. 3.10). Trajectory lengths of $t_{RDF} = -3$ h reproduce the q distribution found in the forecast field of 15 UTC quite well (Fig. 3.4d). In comparison to the interpolated analysis field (Fig. 3.4b), the lower and upper level minima are more pronounced and collocated with the forecast field. The RDF reconstruction starting from analysis fields (Fig. 3.10) with a trajectory length of $t_{RDF} = -15$ h exhibits a structure (not shown) nearly indistinguishable from its analogon starting from the forecast wind fields in Fig. 3.8.

Thus, the combination of analysis fields with the RDF technique is sufficient to reconstruct both the intermediate forecast fields and small scale structures. Two factors contribute to this success: Wind fields exhibit a weaker spatio-temporal variability than tracers like q and iterative interpolations for the trajectory calculations

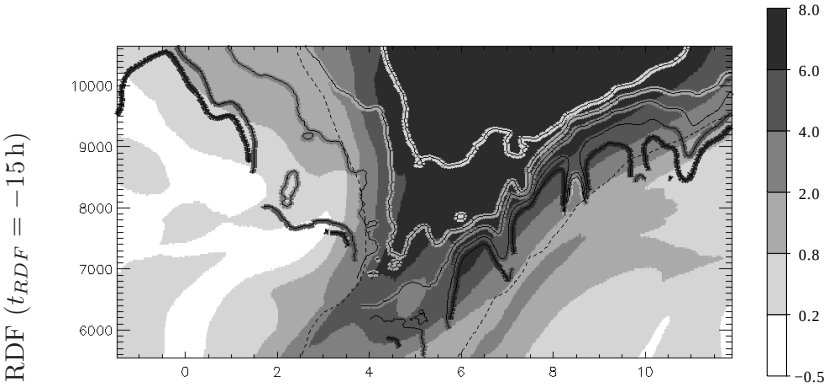

Figure 3.9: The same as Fig. 3.5a) for RDF reconstruction of PV based on forecast and analysis fields with a trajectory length of $t_{RDF} = -15$ h.

further increase the accuracy (see Sec. 2.3).

Dynamical history of air masses ending in the region of the DIAL cross-section

The RDF technique allows an efficient way to visualize the history of the air parcels, but trajectories longer than two days do not effectively reproduce a realistic q or PV field on tropopause levels. Therefore, the LFP, an extension of the RDF technique, is adopted hereafter relating Lagrangian air properties earlier in time to an Eulerian structure disregarding the question of tracer conservation (cf. Section 2.4.3 and Liniger and Davies, 2003).

In Fig. 3.11, q is advected using a trajectory length of 45 h. The region of weak vertical gradients, west of the intrusion, is quite robust and still exhibits a smooth structure. Eisele et al. (1999) detect high ozone concentrations in this region west of the intrusion by a ground based DIAL referring to it as a "secondary intrusion". Stohl and Trickl (1999) additionally use water vapour and ozone in situ measurements and trajectory calculations to show that this air mass has a boundary layer origin. In this case however, the air mass remains upper-tropospheric, its water content, PV and height do not change significantly during the precedent 3 days. Note also the extremely low backscatter ratio (corresponding to low aerosol concentration) in the same region, a further indication of its upper-tropospheric "origin" (see Fig. 3.12b). The backward trajectories stay very close to each other and to the jet-stream.

Between the region of low vertical gradients and the stratospheric intrusion, strong striation can be found in the LFP field. Regions with high q are in the immediate vicinity of very dry air. On the tropospheric side, the striation is aligned with isentropes, whereas the stratospheric part is steeper. Such a feature could correspond to an isentropic down-gliding of the stratospheric air and a diabatic up-gliding of tropospheric air. The majority of the filaments cross the tropopause where it is steepest and their thinness is an indication of mixing of the filaments by diffusion.

The striation found also in other considered quantities (PV, pressure, geographical position, θ, RH) are suspected to be formed by air masses of very distinctive origins that come very close to each other at the ending positions within the cross-

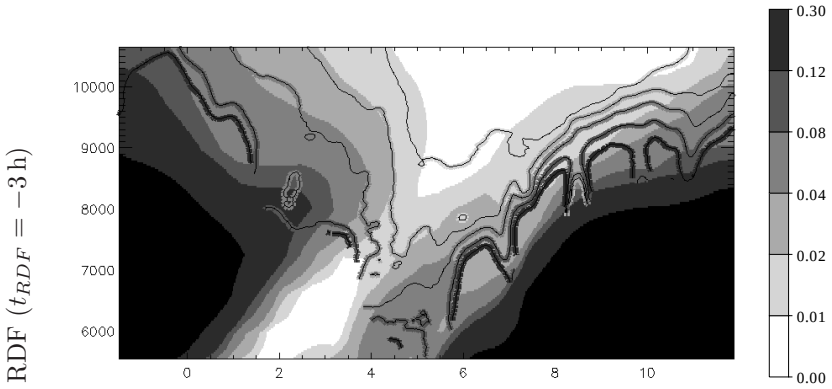

Figure 3.10: The same as Fig. 3.4d) for RDF reconstruction of q based on interpolated analysis fields with a trajectory length of $t_{RDF} = -3$ h.

section. In Fig. 3.11, one prominent filament appears as a thin elongation above the fold identifiable by very high q. To further study the emergence of the striation, this filament is selected for a more detailed investigation.

A possible history for the main striation's evolution is obtained by constructing Lagrangian backward trajectories from a region aligned with the selected filament and its adjacent dry air. The result, illustrated in the three-dimensional depiction of Fig. 3.13 shows air from three distinct source regions approaching one another in the environment of the ridge over Greenland around 00 UTC 5 November (see Fig. 3.14). The moist filament itself is traced back to boundary layer air over the American continent that underwent strong ascent, a decrease in humidity and concomitant diabatic warming within a warm conveyor belt (WCB, cf. Browning, 1990; Wernli, 1997) over Newfoundland. The dry air that finally underlies the moist filament circumnavigates a trough in the Western Atlantic at tropopause elevations before approaching the moist filament over Greenland, and the air that surmounts the filament has a pure stratospheric origin and approached Greenland from the west. Thereafter these air streams remain in juxtaposition and the ensemble advects adiabatically south-westwards with the jet-stream.

Considering the backscatter ratio(Fig. 3.12b), the filament is identifiable as a layer of higher aerosol concentration that is only a few hundred meters thick. An indication for the robustness of the measurement is a similar structure observed 3° further north (Fig. 3.12a). The lack of collocated q observations inhibits though the exact positioning of the filament in regard to the fold at this latitude.

The striation emerges with trajectory lengths of longer than -39 h indicating the formation of the structure at 00 UTC 5 November. Therefore, the upperlevel PV structure is examined closer with selected air parcel positions at 00 UTC 5 November (Fig. 3.14). The tropospheric air parcels are located in a hook-like tropospheric filament that dissolves during the following 12 h. Similar structures were also observed in other studies at the end of the WCB (Wernli, 1997; Martin, Mon. Wea. Rev.).

With respect to cross-tropopause exchange, the striation must be seen as a two way process that cannot be attributed to a spatially confined event, but is related to differential advection during the dissolution of the negative PV anomaly and within the jet-stream later.

Similar filamentary layers were observed in ozone at the western edge of a strato-

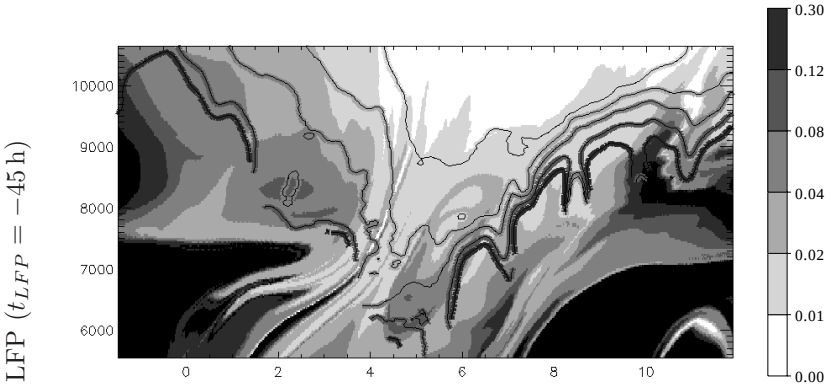

Figure 3.11: The same as Fig. 3.4d) for LFP reconstruction of q based on forecast and analysis fields with a trajectory length of $t_{LFP} = -45$ h.

spheric intrusion by Bertin et al. (2001) and by Vaughan et al. (2001) who employed additionally humidity and static stability from soundings and VHF radar data. For the latter case, the stratospheric intrusion was not represented in the ECMWF analysed fields and enhanced wind shear was found. This could be the reason for the observation with the structures formed earlier in time and then conserved better along its advection.

3.1.6 Horizontal structure at main stage of streamer

In this subsection, the horizontal structure in the analysis and forecast fields at 12 UTC 6 November is compared to the WV satellite scan to gain further insight on upper level dynamics and the tropopause structure. Various reconstruction techniques of the WV field are investigated and interpreted using LFPs.

The high horizontal resolution of satellite scans relative to that of NWP models is opposed to the difficulties to assign a specific vertical level to the WV distribution (see Section 2.6). Nevertheless, numerous studies use WV scans for the interpretation of synoptic, upper-level structures relate it quite successfully to fields as geopotential height (Ramond et al., 1981; Uccellini et al., 1985) or PV on certain isentropes (Manney and Stanford, 1987; Appenzeller and Davies, 1992; Gray et al., 1994). In the latter case, difficulties though arise, since dry air does not necessary correspond to high PV values.

The WV satellite scan is characterised by a dry intrusion over western Europe and a spiral structure over Denmark (Fig. 3.15). The contemporaneous IR scan (Fig. 3.1b) exhibits weak or low-level cloud cover in the regions corresponding to low WV. In Fig. 3.1b), PV shows partial agreement with the WV picture. The large-scale pattern of the intrusion is apparent, but the highest values in PV do not correspond to dry regions in the satellite scan and the western intrusion edge exhibits a zonal shift (see previous Section). The PV field does not form filamentary structures (e.g. the spiral structure over Denmark). CAS on isentropes partially enhances the agreement (as shown in Appenzeller et al., 1996). But, as noted by Wirth et al. (1997), local vertical displacement could be involved in the formation of small scale structures. Thus, it is not yet clear what kind of advection corresponds to small scale WV structures in satellite scans, in particular within positive PV anomalies.

An alternative to the comparison with the PV distribution is applied here-

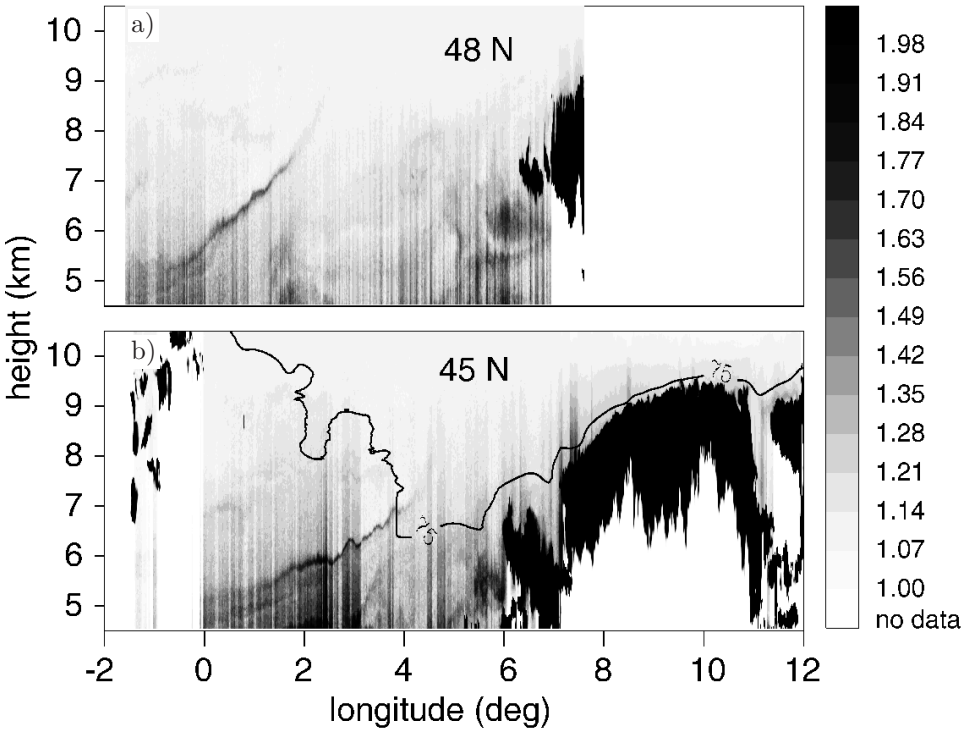

Figure 3.12: Longitude (°E) – height (km) cross-sections of backscatter ratio measured by DLR-lidar along (a) 48°N and (b) 45°N. Overlaid is the DIAL q contour of 0.05 g/kg (from Hoinka et al., 2003).

after by the direct use of the q distribution in the analysed data. Vertically integrated humidity $\int q$ and the temperature T_ρ interpolated to the isosteric surface $\rho_{H_2O} = 75\,\mathrm{mg/m^3}$ are therefore derived from the analyses (see Section 2.6 for further details).

The basic features observed by the satellite as the dry intrusion over Great Britain and France and the more humid regions over Central Europe and Scandinavia are captured by both methods (Fig. 3.16a and b). Also, the positions of most features match the observed ones. The T_ρ distribution fits better the satellite scan in the region of the Mediterranean Sea and west of the streamer, whereas the $\int q$ matches better in the region of the spiral structure. Both techniques fail to reproduce the southern tip and filamentary elongation north of 60°N, also visible in the IR scan (Fig. 3.1b), of the intrusion.

The RDF technique[2] with a trajectory length of $t_{RDF} = -24\,\mathrm{h}$ is used now for the reconstruction of smaller scale structures (Fig. 3.17a and b). The gradients are strengthened significantly. In position and geometry, the southern tip and the northern filamentary elongation both agree quite well.

The regions south of the spiral structure, over the Netherlands, and the streamer's surroundings over the Mediterranean Sea, Italy and west of the streamer are represented better by the T_ρ distribution. Better agreement in the reconstructed $\int q$ field is found at the tip of the intrusion and across the spiral structure over Denmark (denoted in Fig. 3.1b and shown in Fig. 3.2).

[2]applied before the vertical integration resp. calculation of the ρ_{H_2O}

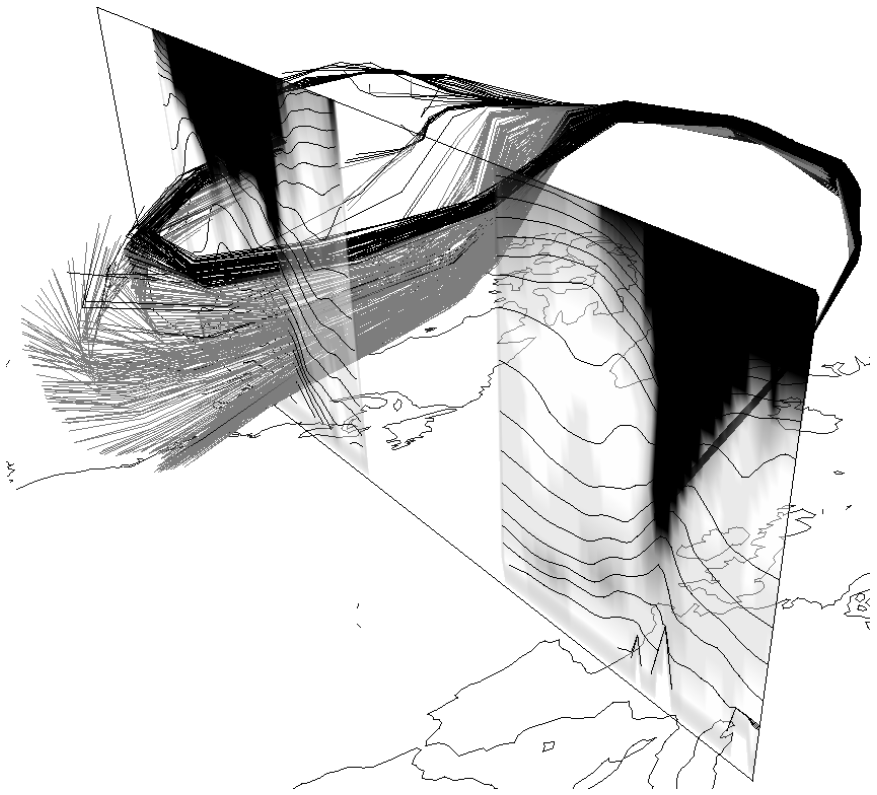

Figure 3.13: Backward trajectories from the region of the striation above the primary fold (Fig. 3.11) shown together with two vertical cross-sections pertaining to 12 UTC 6 November over Europe and 12 UTC 4 November over North America. Stratospheric (tropospheric) trajectories are indicated in black (grey), and the cross-sections display the PV distribution (shaded with dark corresponding to high values) and θ (contour lines with spacing of 5 K) (from Liniger and Davies, 2003).

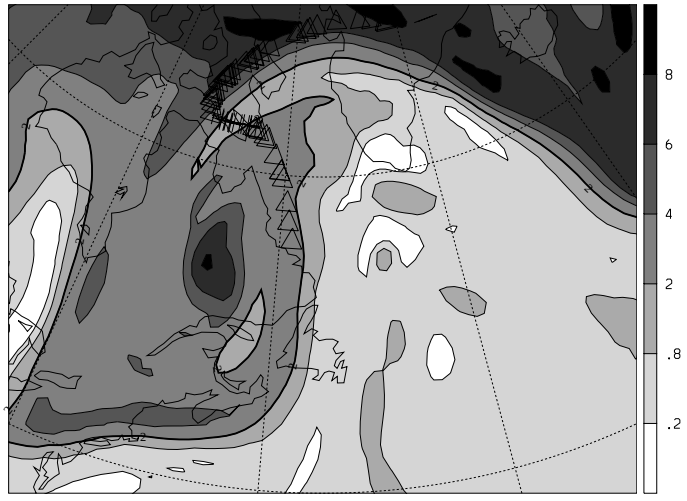

Figure 3.14: PV distribution (shaded in pvu) at the 320K isentrope at 00 UTC 5 November and selected parcel positions of stratospheric (triangles) and tropospheric (crosses) origin.

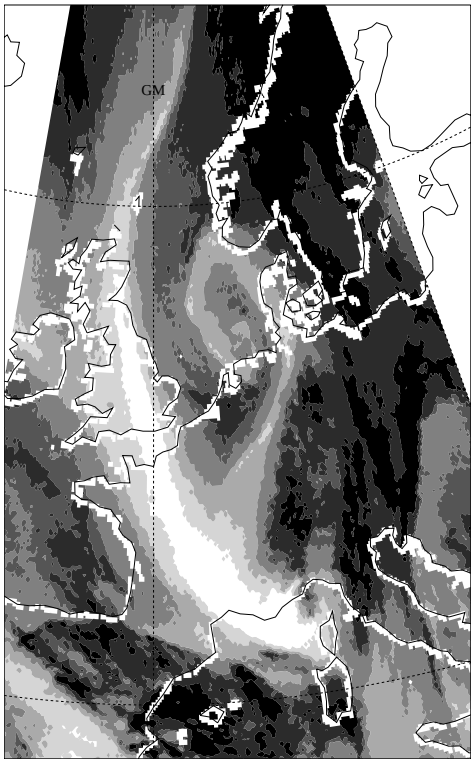

Figure 3.15: Meteosat WV channel (arbit. units).

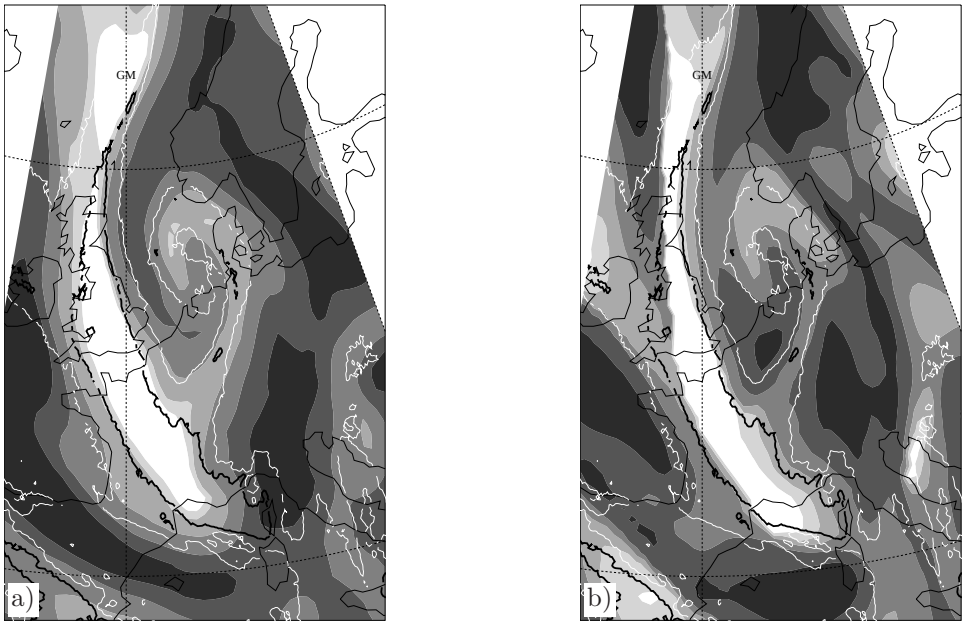

Figure 3.16: (a) ECMWF q vertically integrated from 600 hPa upwards (shaded in arbit. units) and (b) ECMWF temperature on on the $\rho_{H_2O} = 75\,\mathrm{mg/m^3}$ isosteric surface (shaded in arbit. units) at analysis time. Overlaid are two contours of the Meteosat WV channel (black and white lines, arbit. units).

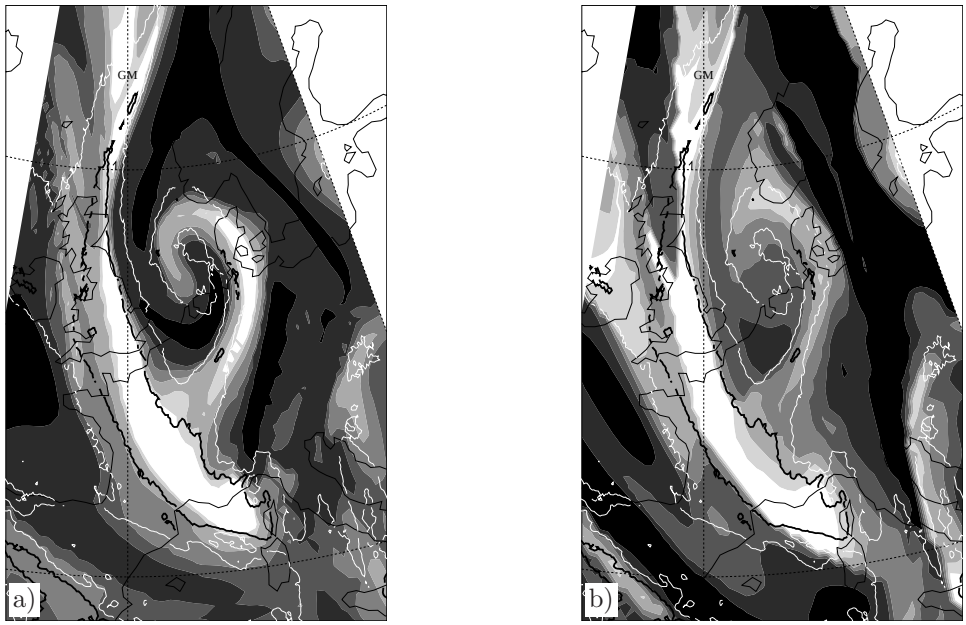

Figure 3.17: The same as Fig. 3.16 based on the RDF reconstructed q field with $t_{RDF} = -24\,\mathrm{h}$.

The partial success of the RDF technique is tried to be explained by LFP applied to the past 24 h of the involved air-masses. The spatial variations in the integrated pressure change Δp along trajectories ending at 450 hPa indicates different source regions of the air masses forming the humidity distribution (Fig. 3.18a). The change in θ ($\Delta\theta$) shows, that the descending air within the intrusion, the dry arm and the northern part of the spiral are advected under more or less adiabatic conditions (i.e. $|\Delta\theta| < 5\,\mathrm{K}/24\,\mathrm{h}$). The vertical displacement is due to meridional advection on the sloped isentropes. The ascending air south and in the center of the spiral structure though undergoes significant diabatic heating. There is also a region of strong diabatic ascent identifiable east of the streamer over Germany that corresponds to a WCB flow (see previous Section).

The small region of strong cooling over France seem to be an artefact of the data assimilation. The inspection of θ and PV along the trajectories reveal unrealistic large temporal variations on the order of 5 pvu/6 h in PV and 4 K/6 h in θ at about a height of 450 hPa over Great Britain.

The vertical section across the structure in the northern part of the streamer in Fig. 3.2a) shows low baroclinicity below the upper level PV anomaly. Together with the weak precipitation and the subsequent isentropic advection of the cut-off, this is indicative for a quasi-horizontal, adiabatic flow (see also Section 3.1.3 and 3.1.7) in the northern part of spiral.

Evidently, the spiral structure is mainly formed by synoptic-scale differential advection as suggested by Appenzeller et al. (1996), but with the involvement of diabatic processes. Secondary role seem to play effects as local vertical circulation (discussed in Wirth et al., 1997). In other investigated cases (not shown), the RDF reconstruction based on analysed data was less successfull. This indicates that these processes could be significant in other flow configurations, but not resolved in the analysis wind fields.

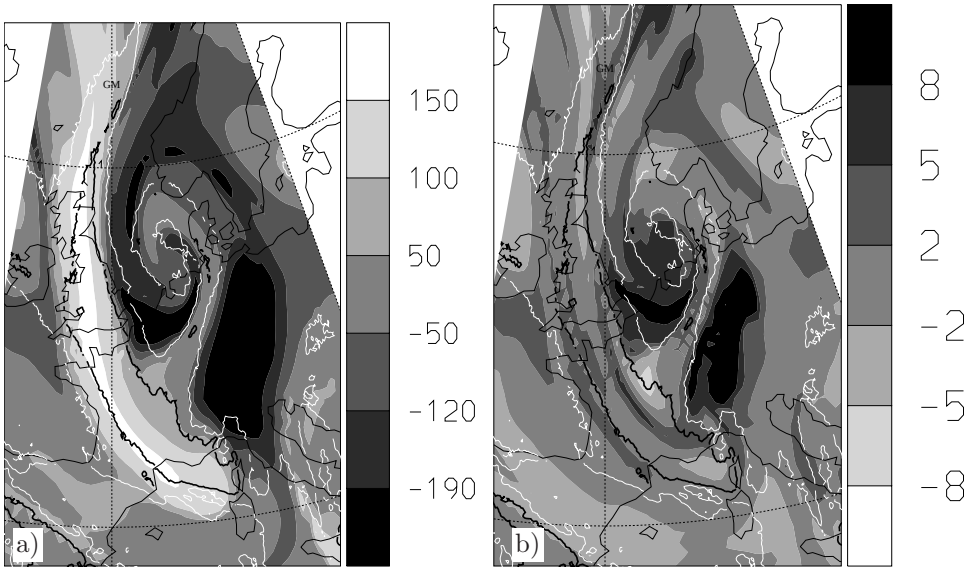

Figure 3.18: (a) $\Delta p = p(0\,\mathrm{h}) - p(-24\,\mathrm{h})$ and (b) $\Delta\theta = \theta(0\,\mathrm{h}) - \theta(-24\,\mathrm{h})$ at 450 hPa (shaded in hPa resp. K). Overlaid are two contours of the Meteosat WV channel (black and white lines, arbit. units).

To summarize, the $\int q$ and the T_ρ both show some similarities to the WV satellite scan. A more detailed view is obtained at the interior and southern tip of the intrusion and the spiral structure over Denmark by applying the RDF technique to the q field. Diabatic processes seem to be related to some of the enhanced regions, but not necessarily, as e.g. at the southern tip of intrusion. The $\int q$ distribution benefits more by the RDF technique, in particular in the diabatic regions.

3.1.7 Lagrangian evolution of the streamer

Further insight into the processes involved in the evolution of the streamer and the accompanying diabatic processes can be inferred from adopting a Lagrangian perspective. Backward trajectories can help detect the origin of the air masses in the lower and upper troposphere which is expected to be strongly related to their q content and diabatic processes. Forward trajectories can help assess the nature and impact of the streamer's break-up.

Therefore trajectories are calculated both forward and backward from the main stage at 12 UTC 6 November. The starting positions comprise a grid that covers the streamer with a horizontal resolution of 0.5° on several pressure levels with a vertical spacing of 50 hPa between 1000 and 100 hPa.

At upper levels, the stratospheric and tropospheric air mass originates over the American continent and is advected over Greenland towards Europe along the jet-stream (see also Section 3.1.4). At lower, tropospheric levels, distinctive source regions can be identified, in particular of the diabatic inflow on the eastern flank (see following subsection). Forward in time, the upper tropospheric air, starting in the vicinity of the streamer is influenced by the strong shear across the streamer and splits (Fig. 3.20b). The stratospheric air also splits and performs STE during the dissolution of the southern cut-off (see the next but one subsection). Groups of trajectories are selected by applying various objective criteria designed to locate

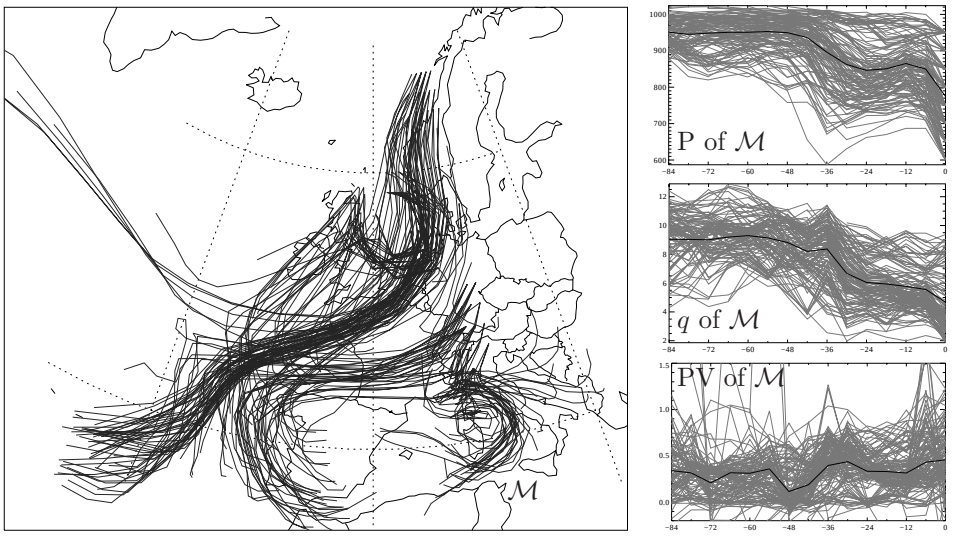

Figure 3.19: 48 h backward trajectories with $\Delta\theta > 1$ K during the last 12 hours and $q > 7$ g/kg before (see text) ending on 12 UTC 6 November (left panel). Pressure (upper right panel, in hPa), q (middle right panel, in g/kg) and PV (lower right panel, in pvu) traced along the subset of trajectories (denoted as $\mathcal{M}$) originating over the Mediterranean Sea with $q > 9.5$ g/kg and ending south of Alps.

and trace air parcels undergoing diabatic processes or STE.

Two particular flow regimes are investigated hereafter in more detail: (i) the diabatic inflow along the eastern flank of the streamer in mid-tropospheric levels adressing the influence of the Mediterranean Sea and (ii) the upper-level and stratospheric outflow, with a focus on the dissolving southern cut-off.

Diabatic processes on the eastern flank

The origin of diabatically influenced air masses on the eastern side of the streamer is identified by selecting coherent ensemble of trajectories (CETs) in the lower and middle troposphere with significant diabatic effects with similar criteria as proposed by Wernli and Davies (1997) (Fig. 3.19). The trajectories ending north of the Alps originate from the Atlantic, mostly west of the Iberian Peninsula. Most of the flow causing precipitation south of the Alps, in particular these with initial high water content emerge from the region of the Mediterranean Sea (denoted as $\mathcal{M}$ in Fig. 3.19). The presumably high SST in this area and their long residence in the lower-most levels (indicated by the shortness of their trajectories) leads to an efficient heating and uptake of humidity in the preceding days. A significant part of the humidity condensates in the vicinity of the PV cut-off over the Mediterranean Sea on 00 UTC 5 November (see Fig. 3.1a). This is indicated by ascent, high PV variability and q decrease in the phase around $t = -36$ h (Fig. 3.19b-d). The southerly flow and the associated diabatic processes south of the Alps and the observed precipitation in the Po valley are linked to the upper level streamer. The loss of humidity below the cut-off over the Mediterranean Sea though inhibits the development of a heavy precipitation event along the Alpine ridge.

After 12 UTC 6 November, the selected air parcels are advected northwards (see also Fig. 3.20b) and pass the region of PV reduction and low stability in upper

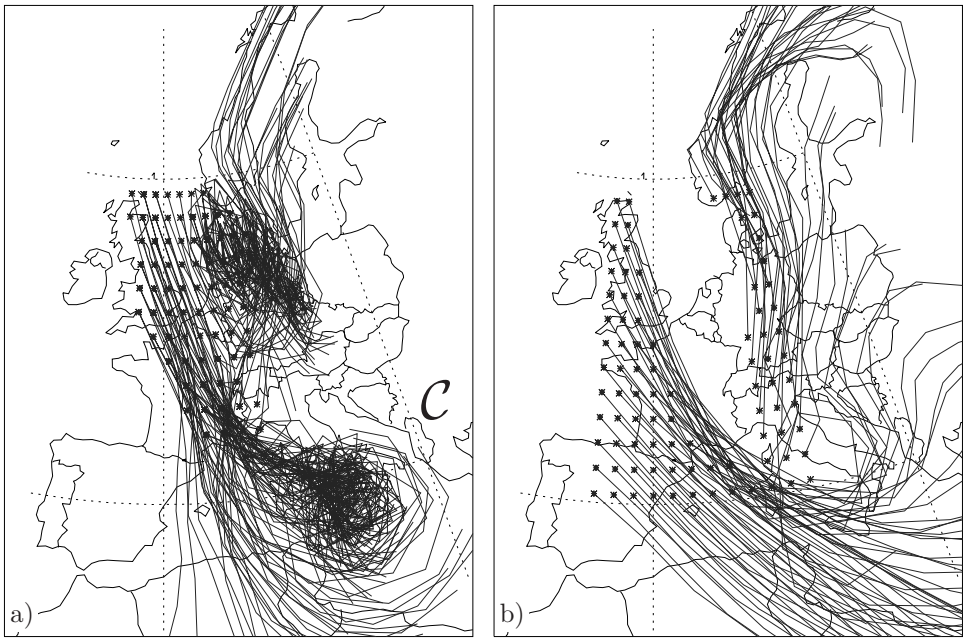

Figure 3.20: 48 h forward trajectories starting on 12 UTC 6 November with (a) initial position between 600 and 350 hPa and $PV(t=0) > 2$ pvu and (b) at 350 hPa and $PV(t=0) < 1.5$ pvu. $\mathcal{C}$ denotes the trajectories trapped in the southern cut-off.

levels that is associated with the streamer break-up during the following day.

Upper-tropospheric and stratospheric outflow

The streamer break-up is also identifiable by the lower stratospheric forward trajectories starting within the streamer (Fig. 3.20a). The air masses are separated into a northern group advected northwards towards the jet-stream and a southern one trapped in the southern cut-off.

Parts of the latter group of trajectories, denoted as $\mathcal{C}$ in Fig. 3.20a, experience STE (i.e. PV values decrease to below 2 pvu, Fig. 3.21) associated with the diabatic decay of the cut-off (Wirth, 1995; Bourqui, 2001). The behavior of the trajectories performing STE strongly depends on their vertical position: The lower air masses just above the tropopause show a faster decrease in PV and increase in q, and after 36 hours, they have performed the exchange and exhibit tropospheric properties ($\overline{q} > 0.3$ g/kg, $\overline{PV} < 2$ pvu). In contrast, trajectories at higher levels do not attain tropospheric PV values for more than 48 hours. Another major difference between the two layers concerns the θ values and their variation. Before and during the crossing of the 2 pvu surface the upper level air shows a stronger decrease in θ than air at lower levels. Later, θ of the lower level air masses even increases.

In the region of the cut-off, convective clouds are found in the IR image (Fig. 3.1) and the precipitation in the ECMWF data indicates convection underneath the tropopause level. The distinctive behaviour of the two groups performing STE is likely to be related: (i) The lower level air mass experiences diabatic heating by latent heat release associated with convection (cf. Gouget et al., 2000). The early increase in q could be related to model diffusion of the strong humidity gradient to the nearby moist, tropospheric region. (ii) The dryness of the upper level air

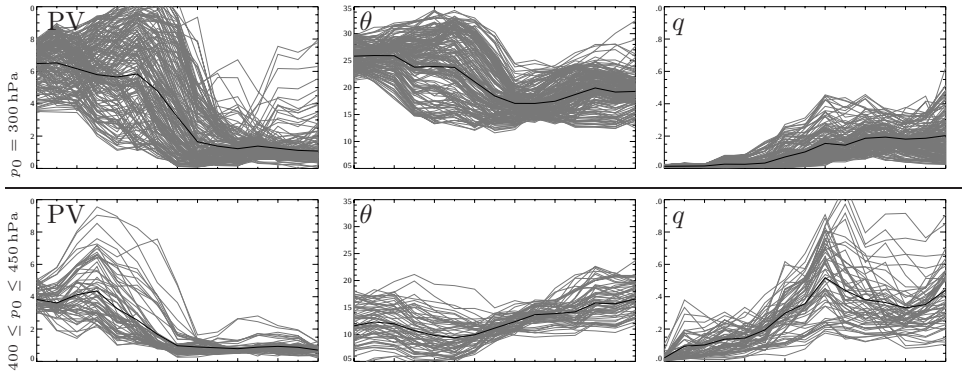

Figure 3.21: PV (left, in pvu), TH (center, in K) and q (right, in g/kg) traced along forward trajectories $\mathcal{C}$ and its average starting on 12 UTC 6 November with initial position at 300 hPa (upper panels) and between 400 and 450 hPa (lower panel) selected by $PV(t = 0) > 3$ pvu and $PV(t = 18\,\mathrm{h}) > 2$ pvu and being in the region of the cut-off over Mediterranean Sea.

and the strong decrease in θ indicate radiative cooling due to radiation at the cloud tops. Both processes, diabatic heating leading to tropopause erosion and cooling resulting in the reformation of a stronger tropopause above are proposed to induce a significant cross-tropopause mass flux (Wirth, 1995; Zierl and Wirth, 1997).

3.2 Tropospheric extrusion

Poleward incursions of tropospheric air on isentropic surfaces at stratospheric elevations take the form of synoptic-scale ridges, meso-scale filaments and cut-offs. They correspond to negative PV anomalies, are frequently associated with surface anticyclones, and can be seen as counterparts to stratospheric intrusions discussed above.

Previous studies on upper-level anomalies considered different aspects: Theoretical studies (Wirth, 2001; Muraki and Hakim, 2001) have emphasized the asymmetry between positive and negative anomalies originating mainly from the meridional temperature gradient and the Earth rotation. Diagnostic-observational studies (Wernli, 1997; Pomroy and Thorpe, 2000; Schwierz, 2001) have proposed the role of moist ascending airstreams, also referred to as WCB (cf. Section 3.1.5), that transport humid sub-tropical air masses into the mid-latitudes and induce shallow upper-level negative PV anomalies. It is further recognized in idealized simulations (Zierl and Wirth, 1997) and case studies (O'Connor et al., 1999) that the decay of negative anomalies can be related to troposphere to stratosphere exchange (TSE).

Flow regimes with geographically persistent negative upper-level PV and underlying anticyclonic anomalies are related to "blocking" that regularly occurs during winter over the eastern North Atlantic and North Pacific and which is often accompanied by anomalous weather conditions in the western continents (see Schwierz, 2001, for a detailed review).

Also, the correlation of PV to quantities as total column ozone (e.g. Danielsen, 1968; Vaughan and Price, 1991) underlines the relevance of negative PV anomalies at upper tropospheric levels to the radiation budget in the mid-latitudes.

The involved dynamical processes and the linkage to the stratospheric complement are analysed in a case study of 21 December 1979. ERA-15 fields, as introduced in Section 2.1, are used for the inspection of upper-level PV charts (Section 3.2.1) and for a Lagrangian diagnosis (Section 3.2.2).

3.2.1 Overview of synoptic evolution

The selected case on 18 - 23 Dec 1979 features a strong poleward incursion of tropospheric air over northern Europe with neighboring areas of stratospheric PV.

On the 318 K isentrope, the negative anomaly develops on the 18th (Fig. 3.22a) south of Greenland, it evolves poleward and propagates slowly eastwards until the 21th. Contemporaneously, the stratospheric air east of the negative anomaly advects southwards to form a long broad PV streamer extending south to 30°N (Fig. 3.22b). This stage is selected for the Lagrangian investigation (see below).

On the 23rd, the incursion is characterized by weak PV gradients across the tropopause and almost cuts off from the tropospheric pool over Scandinavia (Fig. 3.22c). Subsequently, parts of the anomaly disconnect, advect eastwards and dissolve within the stratosphere over Siberia. The remnant of the anomaly reconnects to the tropospheric pool at the end of December.

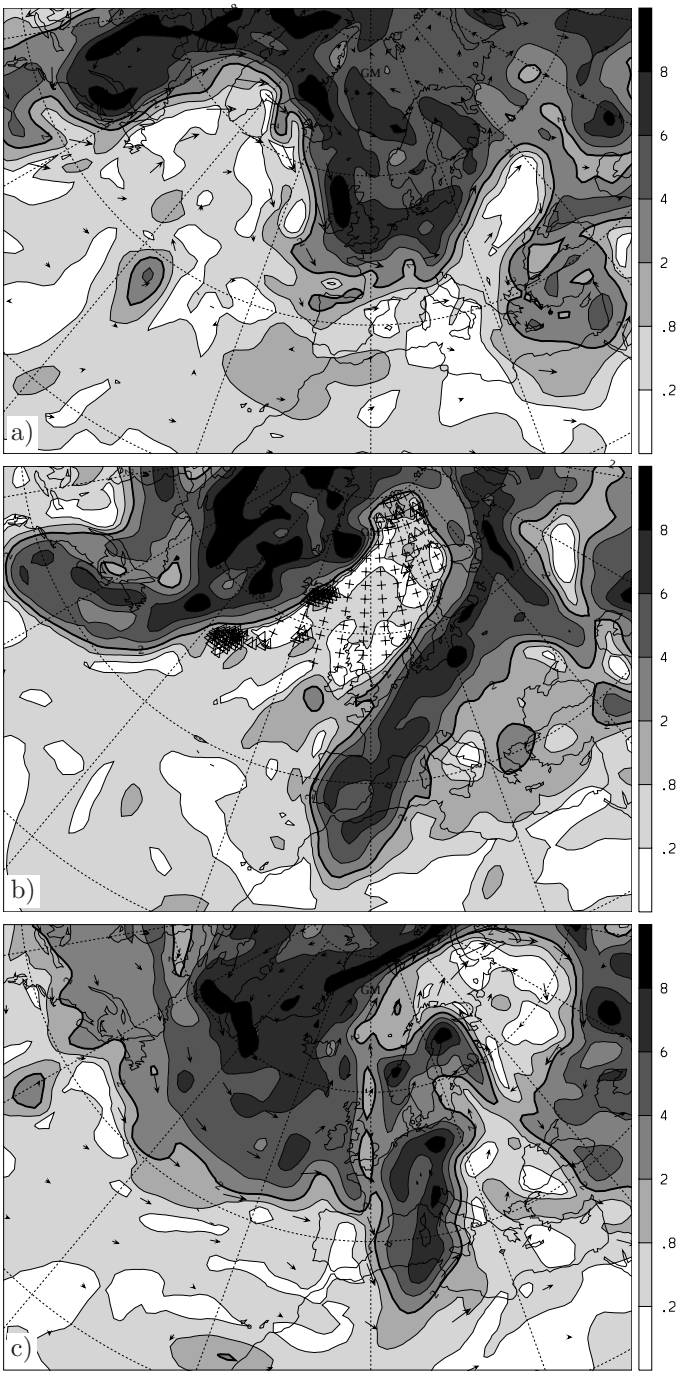

Figure 3.22: PV distribution (shaded in pvu) and wind vectors on the 318 K isentrope at (a) 12 UTC 18 December, (b) 00 UTC 21 December and (c) 06 UTC 23 December 1979. Every 50th trajectory starting point is denoted as cross, every 2nd TSE trajectory starting point as triangle in (b).

3.2.2 Lagrangian perspective

Back- and forward trajectories of 120 h length are initiated on a grid of 0.5° on the 318 K isentrope in the region of $PV < 2$ pvu north of the climatological tropopause

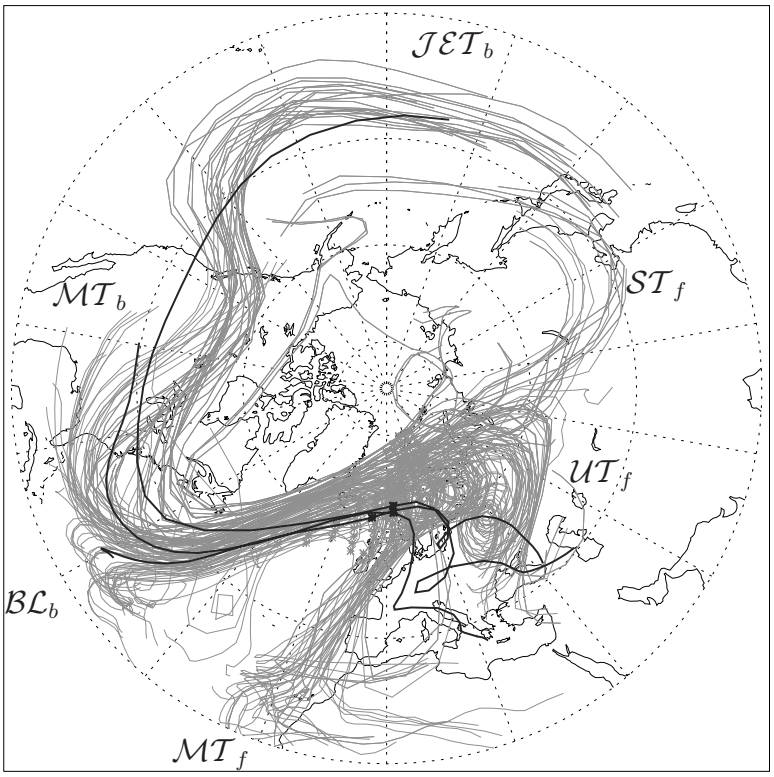

Figure 3.23: Every 50th 240 h trajectory passing the negative PV anomaly on 00 UTC 21 December (grey) and average positions of three subsets, denoted as $\mathcal{BL}_b$, $\mathcal{MT}_b$ and $\mathcal{JET}_b$ in black (see text).

at 00 UTC 21 December (Fig. 3.23, starting points denoted in Fig. 3.22b).

Originating from roughly three different regions, the air masses enter the anomaly from south-west. Emanating from the anomaly, they split into a part trapped within the anticyclone, a part advected southwards and small part moving rapidly to the east. The different groups of trajectories are discussed in the following two subsections in detail.

Origins of air masses

Subsets of the trajectories are selected based upon their height and latitude before 00 UTC 21 December. A set of 1500 trajectories with a position below 900 hPa originates from the Atlantic boundary layer (denoted as $\mathcal{BL}_b$ in Fig. 3.23). The rest of the backward of trajectories are separated by having their origin to the west resp. east of 150°W and consist of 1170 resp. 1350 trajectories ($\mathcal{JET}_b$ resp. $\mathcal{MT}_b$).

All three groups exhibit characteristic behaviour not only with respect to the differing geographical origin, but also to the history of their physical parameters (pressure, PV and q, cf. Fig. 3.24).

The ensemble $\mathcal{BL}_b$ has a sub-tropical boundary layer source located in a region of high sea surface temperatures. An uptake of q can be observed during the first two days. Subsequently, $\mathcal{BL}_b$ experiences a rapid and strong ascent and a strong decrease in q, indicative of strong cloud condensation. The synchronous increase in PV to

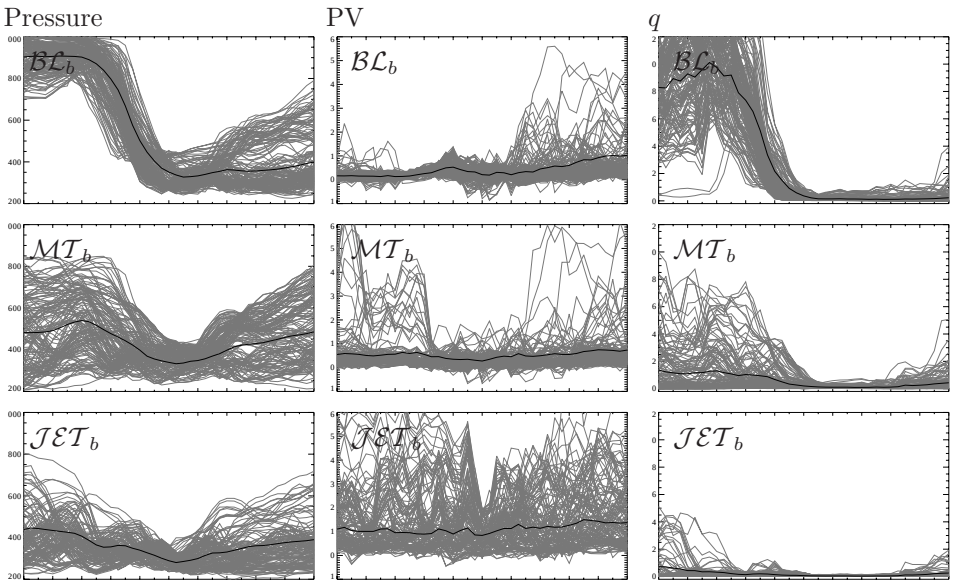

Figure 3.24: Pressure (left, in hPa), PV (center, in pvu) and q (right, in g/kg) traced along every 10th trajectory of subsets denoted as $\mathcal{BL}_b$, $\mathcal{MT}_b$ and $\mathcal{JET}_b$ in Fig. 3.23. The average is shown as black line. $t = 0$ corresponds to 00 UTC 21 December.

more than 1 pvu and successive decrease to negative PV values of some trajectories indicates the PV tendency induced by the diabatic heating, qualitatively in good agreement with the suggestion for the WCB by Wernli (1997). The weakness of the PV tendency can be related to several independent factors: (i) the trajectories are initiated on a single two-dimensional isentrope, not in a whole volume, and do not cross the region of maximum heating; (ii) the gradients of diabatic heating are weak, since the heating is widely distributed in the vertical; (iii) and the spatial resolution of ERA-15 is not fully sufficient to resolve the details of this moist ascending airflow (see Section 2.1).

The second group, $\mathcal{MT}_b$ originates from mid-tropospheric levels with corresponding lower q. The weak descent and subsequent ascent is due to the meridional advection on the sloped isentropes by the positive PV anomaly located west of the negative anomaly.

The third subset, $\mathcal{JET}_b$ is of upper-tropospheric jet-stream origin. High variability in PV indicates the vicinity to the tropopause. Most of the air masses cross the 2 pvu-tropopause several times and thus do not undergo true STE. $\mathcal{JET}_b$ contains very dry air and the variations in pressure are mainly due to meridional adiabatic advection.

Destination of air masses

After 00 UTC 21 December, the air masses separat into three distinct destination regions, that also correspond to their evolution in height: (i) a mid-tropospheric group that is advected out of the anomaly southwards into the subtropics with an associated increase in pressure to about 600 hPa ($\mathcal{MT}_f$ in Fig. 3.23); (ii) a group trapped within the negative PV anomaly for the following 120 h, remaining at upper-tropospheric levels ($\mathcal{UT}_f$); (iii) and a third, less numerous group that is

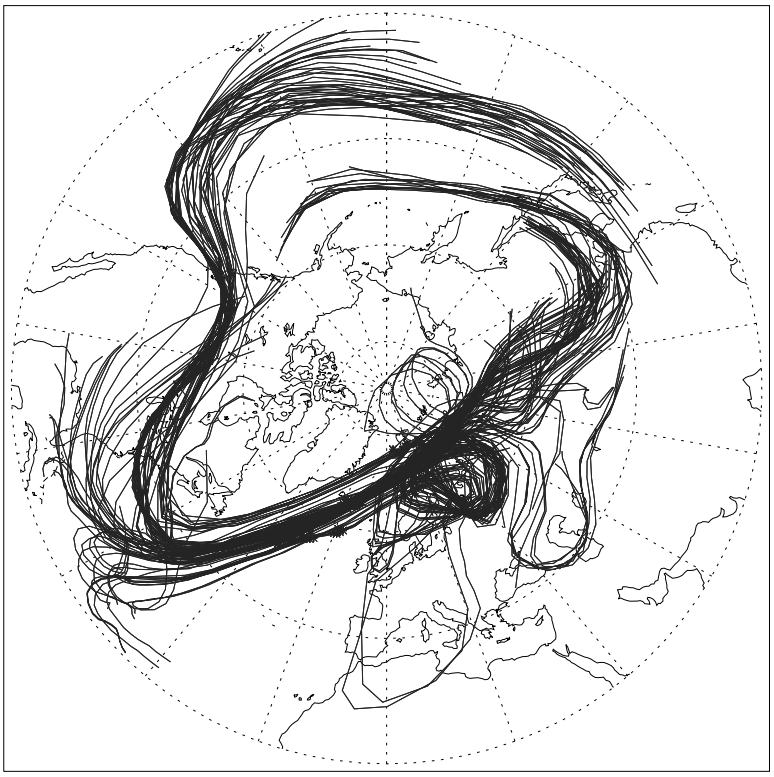

Figure 3.25: Every 2nd 240 h trajectory passing the negative PV anomaly at 00 UTC 21 December and later undergoing troposphere to stratosphere exchange (see text).

rapidly advected eastwards and also stay at upper levels ($\mathcal{ST}_f$).

These three groups are only weakly related to the regions of origins by inspecting the pressure evolution of the three subsets in Fig. 3.24. Most of $\mathcal{JET}_b$ stay at upper levels, whereas $\mathcal{BL}_b$ are separated into a descending and a non-descending group. No single deduction can be made for the destination of $\mathcal{MT}_b$ parcels that is split equally among the three outgoing airflows.

The traced q and PV values reveal that the higher elevation groups are drier and a significant portion, mainly of $\mathcal{ST}_f$, has PV values substantially larger than 2 pvu, i.e. they undergo troposphere-stratosphere exchange.

For a more detailed examination of TSE, trajectories are selected by having PV values < 2 pvu during the day before 00 UTC 21 December, and PV values > 2 pvu from 00 UTC 25 December onwards (Fig. 3.25). Thus, in contrast to Bourqui (2001), where a "residence time" of typically 48 h is applied, a threshold value of 24 h is used before and after a transition time of 4 days (instead of 6 h). Such a criterion does not exclude trajectories that stay close to the tropopause for several days as during the slow diffusion and dissolution of negative PV anomalies. The air masses could change their chemical properties during the long transition time and are therefore undesired by Bourqui (2001) that concentrates on the quantification of cross-tropopause transport. The focus of this study though is the Lagrangian analysis of negative PV anomalies.

The air parcels performing TSE originate from all three source regions described above (Fig. 3.25). Particularly noteworthy is the boundary layer origin of some of

the trajectories (cf. deep exchange events, as introduced in Wernli and Bourqui, 1999, and discussed in Stohl, 2001, and Wernli and Bourqui, 2002). At 00 UTC 21 December, the exchange parcels are located at the north-western flank of the extrusion in the jet-stream (Fig. 3.22b). Afterwards, TSE occurs in the scope of a diffusing filament and later in a dissolving tropospheric cut-off, indicated by the cirular path over Finland in Fig. 3.25, that corresponds to trapped parcels advected anticlockwise along the edge of the negative anomaly. The Lagrangian variability of traced PV is much higher before and after the exchange events.

To summarize, three distinct origins can be identified, the jet stream at upper tropospheric levels, mid-tropospheric levels and the sub-tropical oceanic boundary layer. Air masses from the latter have a high water content that is reduced during strong diabatic effects before entering the anomaly at the western flank. The origin or initial PV values of the trajectories does not give a clear indication of their destination and subsequent evolution after 21 December, in particular not for TSE. Preferred positions for TSE within the negative anomaly are along its edge. Then, small scale generation (filamentation) and subsequent diffusion in combination with radiative processes indicated by the steady dissolution of low PV (as proposed by Zierl and Wirth, 1997) lead to slow exchange during quasi-horizontal motion accompanied by high Lagrangian variability of PV.

3.3 Further remarks

Quasi-two-dimensional Rossby wave breaking has been analysed in two case studies of a stratospheric in– and tropospheric extrusion. Both exhibit special Lagrangian and Eulerian structures that can be summarized as follows:

Intrusion: High PV values and low q inferred from DIAL measurements, satellite scans and ECMWF analysis are associated with the streamer's stratospheric origin and a significant vertical extent into the troposphere and an overhanging western edge.

The western edge features a region of strong striation across the near vertical tropopause and an upper tropospheric dry anomaly located west of the intrusion that both stress the recent confluence of differing air masses. On its eastern edge, a spiral structure indicates the presence of strong chaotic advection, more pronounced though in a quasi-horizontal perspective. Humidity inflow was identified both from the south (Mediterranean sea) and the west (Atlantic ocean) and causes diabatic effects at the streamer's eastern edge, partly prompted by the Alps.

Subsequently a huge amount of air from the stratospheric pool is separated into two cut-off systems. One of these dissolutes diabatically resulting in significant STE.

Extrusion: A much broader, but less pronounced upper level signal is associated with the negative PV anomaly. The PV gradients along the tropopause weaken during the subsequent development

Subtropical boundary layer air gets together with mid-tropospheric and upper level air at the western edge of the tropospheric filament. The ascending part from the boundary layer can be considered as outflow of the WCB. Within the low PV anomaly, a part of the air masses is separated from the tropospheric

pool and in parts performs TSE that is likely to be in connection with radiative diabatic processes. A second part of the low PV anomaly is advected southwards back into the subtropics. There appeared no direct link between the in- and outfow regions.

Beside the pronounced asymmetry in geometry and PV values, both representations of Rossby wave breaking stir the middleworld flow irreversibly and thus have a significant impact on the upper troposphere transport processes.

Chapter 4

Statistical Properties of Lagrangian Flow Structures

There has been growing interest in transport processes of the middle- and overworld during the last decades. Features like stratosphere–troposphere exchange (Holton et al., 1995) or isolated flow structures like the stratospheric polar vortex (Juckes and McIntyre, 1987) are of central importance for the atmospheric composition of the involved air masses. Aspects with implications for climate are the permeability of transport barriers and the relevance of localized aerosol ingestions by air traffic (e.g. Schumann et al., 1996; Brasseur et al., 1998; Kärcher, 1999) or volcano eruptions (e.g. Robock, 2000). The stirring of tracers plays a key role in the linking of spatio-temporal scales and the understanding of the dynamics and chemistry (Tan et al., 1998). The aim of this chapter, is to explore a new kinematical perspective of the middle- and overworld in order to link the aforementioned phenomena with structures as discussed in the previous chapter. In the following the focus is on time scales of less than two weeks and therefore the global and synoptic-scale dynamical processes can be assumed as two dimensional resp. isentropic (Holton et al., 1995).

Isentropic forward trajectories are initialized for various prototypes flow structures on a regular hemispheric 0.5° grid on several isentropes and advected by ECMWF analysed wind fields. This large number of trajectories can provide an enormous amount of information. The desired reduction of information is achieved by the use of relative dispersion $\sigma(t)$ as a single value representing the kinematic history of an air parcel between its initialization and the time t (Section 2.4.4).

First, the dispersion of trajectories is examined on selected isentropes for selected dynamical structures (Section 4.1). The findings are then used for a statistical analysis (Section 4.2) leading to the definition of a characteristic time scale and the inspection of the seasonal variability (Section 4.3).

4.1 Horizontal dispersion structures

The global distribution of $\sigma(48\,\mathrm{h})$ on 320 K is shown in Fig. 4.1 at a particular time instance in March 2000. It is richly structured and exhibits features closely related to chaotic behavior, band-like structures of high dispersion, island-like regions of low values and high variability particularly near the tropopause, similar to the Lyapunov exponent distribution observed by Pierrehumbert and Yang (1993).

The bands are often located (almost) parallel to the tropopause. Regions of strong undulations, as over America, are associated with particularly high values.

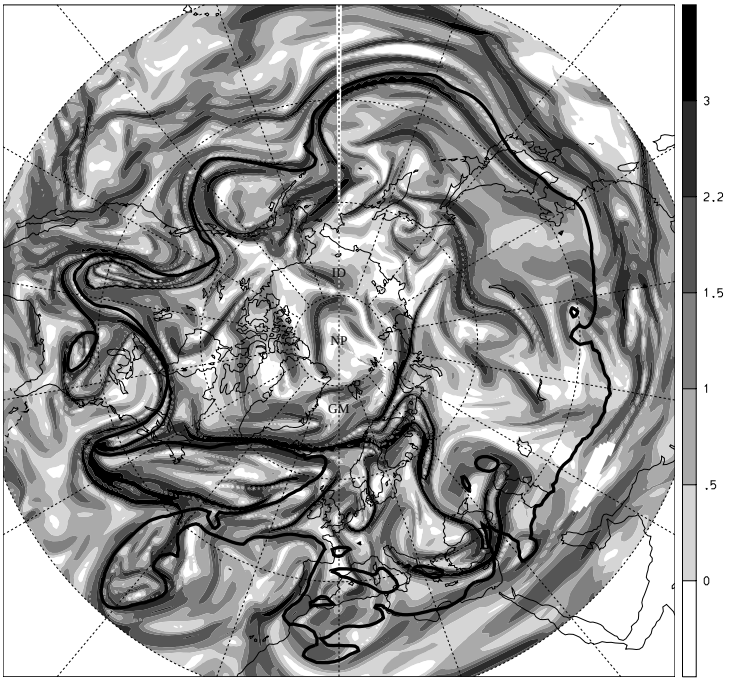

Figure 4.1: $\sigma(48\,\mathrm{h})$ (shaded) and tropopause on the 320 K isentrope at 12 UTC 18 March 2000.

But also other structures, as the low values within the ridge over the Northern Atlantic, suggest a relation to the instantaneous Eulerian PV field.

The high complexity of the global distribution complicates the interpretation, and therefore a closer look is taken at specific dynamical structures that partly have been discussed in the previous Chapter. As archetypical structures a cut-off cyclone, a strong jet stream, stratospheric and tropospheric streamers and the stratospheric polar vortex are chosen.

4.1.1 Cut-off cyclone

The relatively simple quasi-horizontal flow configuration is presented that is associated with a stratospheric cut-off cyclone and a jet-stream not too far from it. The system can be seen as a small vortex structure that decays in a near stationary strongly sheared background flow.

After a synoptic description of the selected 2 day time period, the dispersion structure is studied and explained by the inspection of specific trajectories.

Synoptic description

From a streamer breakup over the North American continent, a cut-off cyclone emerged over Baja California on 00 UTC 01 February 1997 with a very pronounced cyclonic velocity field (Fig. 4.2a). Subsequently, the cut-off was advected eastwards crossing Mexico and eroded synchronously (Fig. 4.2b). The cut-off is clearly separated from the strong and straight jet-stream over the USA during the whole period.

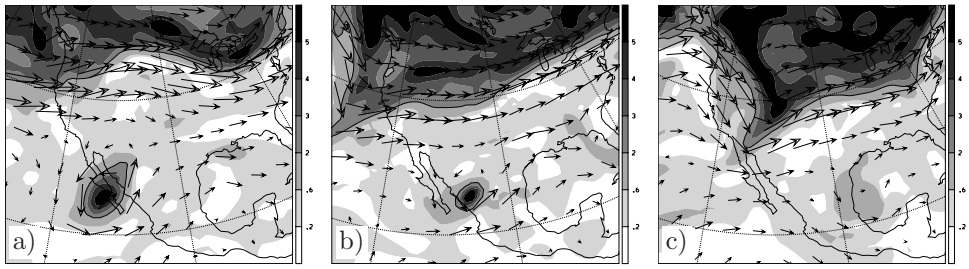

Figure 4.2: PV distribution (shaded in pvu) and wind vectors on the 320 K isentrope at (a) 00 UTC 01 February 1997, (b) 00 UTC 02 February 1997 and (c) 00 UTC 03 February 1997.

At 00 UTC 03 February, only a weak signal in PV and the associated wind field can be identified on the 320 K isentrope over the east coast of Mexico (Fig. 4.2c).

Dispersion

The $\sigma(24\,\mathrm{h})$ distribution exhibits several striking features (Fig. 4.3a). Band like structures of high dispersion dominate the structure forming a double spiral around the cut-off. Also, the center of the cut-off features a relative minimum. The dispersion of the 48 h trajectories $\sigma(48\,\mathrm{h})$ is very similar, but associated with higher values (Fig. 4.3b). Regions of high values in $\sigma(24\,\mathrm{h})$ also have high values in $\sigma(48\,\mathrm{h})$.

Associated trajectories

Three regions of low dispersion are chosen for a closer inspection of the associated trajectories: (i) The center of the cut-off; (ii) both sides of the northern band and (iii) the southern band (as denoted in Fig. 4.3b).

The center of the cut-off is expected to trap parcels during its advection if it does not (entirely) decay. Arbitrary 72 h trajectories with an initial stratospheric signature within the cut-off are shown in Fig. 4.4a). Due to the eroding, some of the parcel paths disperse before the vanishing of the cut-off. The selection of parcels with low dispersion ($\sigma(48\,\mathrm{h}) < 1$) reveals the air masses that stay trapped within the cut-off till its dissolution (Fig. 4.4b).

The region across the northern band is chosen to include the location where a third band branches eastwards (cf. Fig. 4.3b). The three groups of low dispersion (i.e. $\sigma(48\,\mathrm{h}) < 1$) can be seen as representative for the three associated pools of low dispersion. The southernmost group is advected cyclonically around the cut-off, whereas the other two ensembles are influenced by the jet-stream and advected eastwards (Fig. 4.4c). The cause of the secondary branch is inferred from the inspection of the parcel positions: Whereas the northern group is rapidly advected eastwards, the second group travels only about 10° in longitude during the first 24 h. On the next day, the southern group is also rapidly advected, when it approaches the jet-stream.

The region across the southern band of high dispersion separates two areas of different wind direction and strength (Fig. 4.4d). The eastern group is in a westerly regime whereas the western group exhibits anticyclonic behaviour with

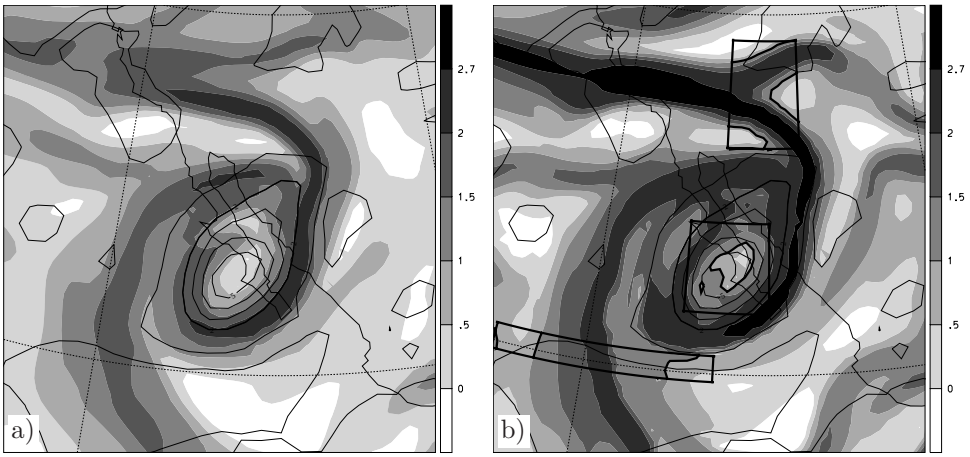

Figure 4.3: (a) $\sigma(24\,\mathrm{h})$ and (b) $\sigma(48\,\mathrm{h})$ (shaded) and PV (thin contour lines, spacing as in Fig. 4.2) on the 320 K isentrope at 00 UTC 01 February 1997. Bold lines in (b) denote regions used to select ensembles of trajectories (see text).

weak winds. The low PV in this region (see Fig. 4.2a) indeed indicates remnants of an anticyclone.

4.1.2 Jet-stream

Along with vortices, the jet-stream is one of the most prominent Eulerian quasi-stationary structures in mid-latitudes at tropopause levels. In contrast to vortices however, the air masses usually reside only for a short period of time in the neighbourhood of the jet. A typical jet-stream is therefore chosen that is relatively long and persistent for several days over the North Atlantic (Fig. 4.5a-c). At 12 UTC 10 January 1999, a strong jet can be identified along the tropopause over the American east coast with a maximum in velocity south of Greenland (Fig. 4.5a). During the following day, the anticyclone over the eastern North Atlantic expands and intensifies yielding high velocities along the neighbouring tropopause (Fig. 4.5b). Contemporaneously, the trough over Europe is distorted towards southwest and starts forming a streamer at 12 UTC 12 January with high velocities on both of its flanks (Fig. 4.5c). The anticyclone exhibits a slightly broader structure than the one discussed in Section 3.2.

The dispersion in the region of the jet-stream is calculated with trajectories starting at 12 UTC 10 January (Fig. 4.5d). Evidently the high velocities and the associated strong shear at the jet's flanks cause bands of very high dispersion. At first sight, the high dispersion bands appear parallel to the tropopause. In the south-western part the 2 pvu isoline is collocated with the northern dispersion band, further east though, in particular in the region of the northerly flow, it is collocated with the southern band. A thin band of low dispersion can be identified in between the two high dispersion bands along the jet axis. Analogous the previous subsection, examples of low dispersion trajectories are selected for further analysis in a region located across the jet axis.

The inspection of the three groups of trajectories reveals very distinctive behaviour (Fig. 4.6). The stratospheric group is advected northwards away from the tropopause, the tropospheric group follows the jet-stream slightly longer and then

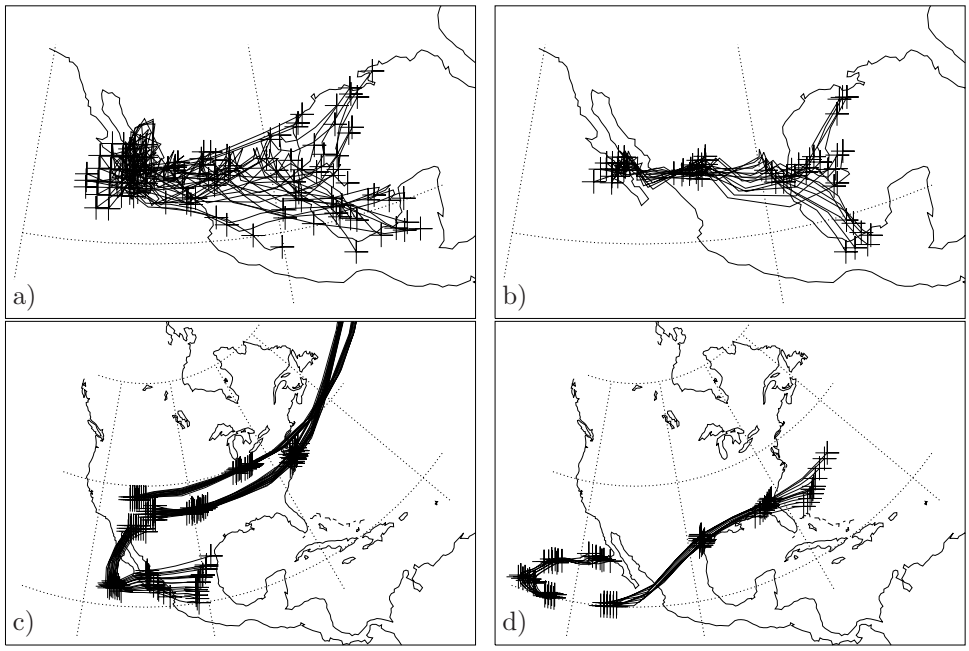

Figure 4.4: Trajectories starting at at 00 UTC 01 February 1997 selected by (a) PV(0 h) > 2.2 pvu in the cut-off, (b) $\sigma(48\,\mathrm{h}) < 1$ in the cut-off (c) $\sigma(48\,\mathrm{h}) < 1$ around a band of high dispersion north of the cut-off and (d) $\sigma(48\,\mathrm{h}) < 1$ around a band of high dispersion south-west of the cut-off (see Fig. 4.3 for the locations). Crosses correspond to positions at 00 UTC.

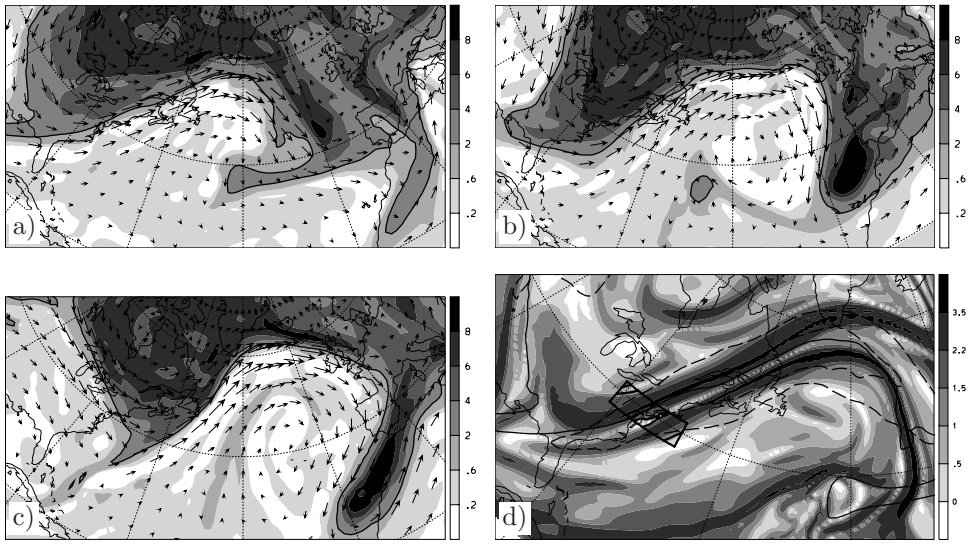

Figure 4.5: PV distribution (shaded in pvu) and wind vectors on the 320 K isentrope at (a) 12 UTC 10 January 1999, (b) 12 UTC 11 January 1999 and (c) 12 UTC 12 January 1999. (d) $\sigma(48\,\mathrm{h})$ (shaded), tropopause (bold line), and velocity (dashed contours of 50 and 70 m/s) on the 320 K isentrope at 12 UTC 10 January 1999. Bold lines in (d) denote region used to select ensembles of trajectories (see text).

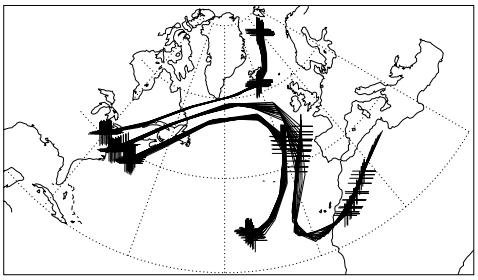

Figure 4.6: Trajectories starting at at 12 UTC 10 January 1999 selected by $\sigma(48\,\mathrm{h}) < 1$ in a region across the jet-stream (see Fig. 4.5 for the locations). Crosses correspond to positions at 12 UTC.

gets advected towards the subtropics around the anticyclone. The centered group however stays trapped within the jet and surrounds the streamer over Europe. The structure of sandwiched air masses of low dispersion neighboured by two bands of high dispersion indicates the presence of (confined) barrier inhibiting transport across a collocated jet (see discussion in Section 4.4).

4.1.3 Tropospheric extrusion

The dispersion of trajectories starting within the upper-tropospheric extrusion discussed in Section 3.2 is shown in Fig. 4.7. Whereas high dispersion bands are aligned with the north-western and south-eastern margins, the northernmost region of the extrusion is separated only weakly from the stratosphere. In contrast, a band along the axis of the extrusion separates air masses with a subtropical destination east of it from air masses staying in northern latitudes (see Fig. 3.23). The lower dispersion within the eastern part is due to the low velocities these air masses experience in the subtropics. The western part is richly structured reflecting the strong deformation and near disruption of the extrusion during the the subsequent days (see Fig. 3.22c). There is a noteworthy blob of high dispersion over Iceland collocated with air masses that perform TSE later in a diffusing filament (see Fig. 3.22b), resp. Section 3.2.2).

4.1.4 Streamer

As a counterpart of a tropospheric extrusion a stratospheric intrusion, the streamer over Europe at 12 UTC 06 November, is used hereafter for a dispersion analysis on the 320 K isentrope. Its synoptic and Lagrangian development was discussed in detail in Section 3.1.

The interior of the streamer exhibits three regions of low dispersion that are examined using selected trajectories (Fig. 4.8b). A first coherent air mass $\mathcal{C}_1$ is initially aligned with the western edge and collocated with the southerly flow and will be trapped in the southern Mediterranean cut-off (see Fig. 3.20a). A second region $\mathcal{C}_2$ is collocated with the PV maximum in the northern part that later forms the center of the northern cut-off. The destination of the air masses starting in the third region $\mathcal{J}$ at the southeastward tip is not directly evident from the knowledge of the streamer's future evolution. Figure 4.8b) shows that these trajectories are advected northwards towards the jet-stream (crossing the path of $\mathcal{C}_2$).

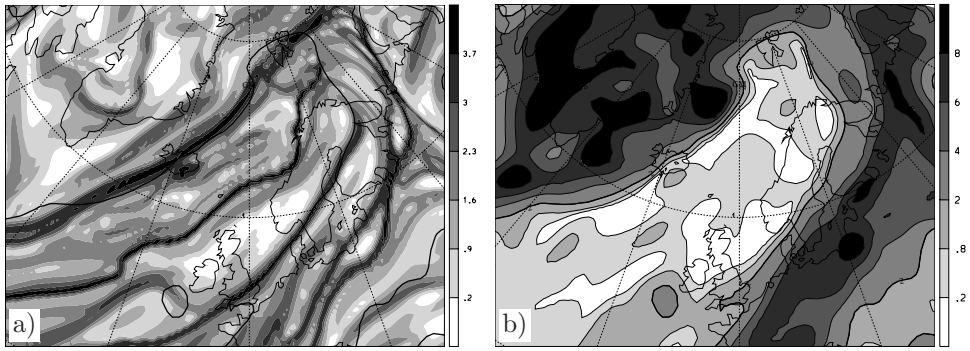

Figure 4.7: (a) $\sigma(48\,\mathrm{h})$ (shaded) and (b) PV (shaded) on the 318 K isentrope at 00 UTC 21 December 1979. In both panels, the PV = 2 pvu tropopause is denoted as bold contour

The northernmost part of the streamer features a band of high dispersion crossing the PV isolines. It is a signature of the subsequent disconnection of the air masses within the streamer from the masses remaining within the main stratospheric pool. Within the streamer itself, a meridionally aligned band of high dispersion represents the axis of the streamer located between the northerly and southerly flow where the shear is strongest. The western edge is confined by a third band of strong dispersion that disconnects from the streamers tip southeastwards over the Mediterranean sea and separates the air from within the streamer and east of it from the air that is slowly advected towards the subtropics (see Fig. 3.20b). This band emerged by the same reason as the southern band described in Section 4.1.1.

4.1.5 Polar vortex

The polar vortex example is investigated to test the dispersion as a diagnostic for the well documented large-scale quasi-stationary structure. The degree of impermeability of the polar vortex edge, and the strong stirring in the surf zone is studied for the southern hemispheric vortex during September 1999. This phase is chosen because of the presence of an anomalously strong zonally symmetric polar vortex, associated with near-record low stratospheric temperatures and an exceptionally strong gradient in the geopotential height field between 60° and 80°S (Bell et al., 2000).

At 00 UTC 01 September, the southern polar vortex has an almost zonally symmetric geometry with a strong meridional PV gradient around 60°S resp. at a PV value of -40 pvu (Fig. 4.9a). The intense PV gradients are collocated with a strong polar night jet (rotating clockwise around the vortex). Further equatorwards, the surf zone is clearly discernible by weak and unorganised PV gradients. In the regions of strongest curvature along the vortex edge, equatorward bands of relatively higher PV indicate vortex erosion due to Rossby wave breaking (McIntyre and Palmer, 1983). Subsequently, the vortex develops a wave-number 3 structure with a region of particular strong erosion over the Pacific (Fig. 4.9b). The wave number 3 structure persists for the following days (Fig. 4.9c).

The center of the jet that follows the vortex edge can be identified by a band of very low dispersion calculated with 120 h trajectories (Fig. 4.10a). There are bands of high dispersion along both flanks, but narrower and of higher values on the equatorward side. The equatorward bands disconnect from the jet in the regions of highest curvature and accentuate the regions of subsequent wave number 3 structure

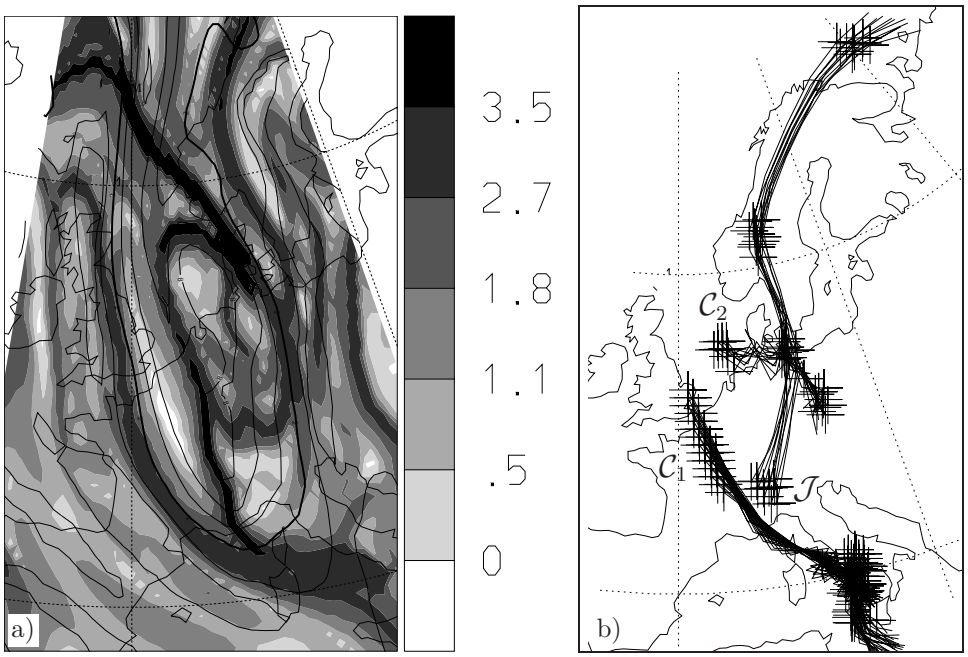

Figure 4.8: (a) $\sigma(48\,\mathrm{h})$ (shaded) and PV (thin contour lines, spacing as in Fig. 4.5a) on the 320 K isentrope at 12 UTC 06 November 1999. (b) Trajectories starting within the streamer and selected by $\sigma(48\,\mathrm{h}) < 0.5$. Crosses correspond to positions at 12 UTC, labels denote starting positions (see text).

development. On the inner side of the high dispersion bands the air is advected around the troughs and ridges and stays close to the jet whereas on the outer side, the air gets disconnected from the jet region at the crests, i.e. eroded equatorwards (cf. Waugh and Plumb, 1994). Within the rest of the surf zone and the innermost of the vortex, the dispersion seems not to be directly related to the initial PV field.

Although trajectories of 120 h are used for the dispersion calculation, the values are not higher than for the previously discussed cases with 48 h trajectories within the middleworld. With longer trajectories, of 282 h (11.75 days) length, the overall values increase significantly, in particular in the surf zone. But the band of low dispersion in the jet core is still present emphasizing the stability and impermeability of the barrier structure (Fig. 4.10b).

4.2 Meridional and vertical characteristics

The diverse structures investigated in the previous Section imply a relationship between dispersion and initial PV resp. PV gradients. Also, a strong dependency of the absolute values to the height (in θ) was found. It remains unclear, whether there are generally valid interrelations, in particular since the inspection of the global distribution reveals highly complex structures (see Fig. 4.1).

In Figure 4.11 the averaged dispersion of trajectories initialised at 00 UTC 01 March 2000 is shown as a function of equivalent latitude for the middle– and overworld. The concept of equivalent latitude is employed hereafter to explore the link between initial PV and the subsequent dispersion. Equivalent latitude allows the inspection of statistical quantities as mean or variance along PV contours and

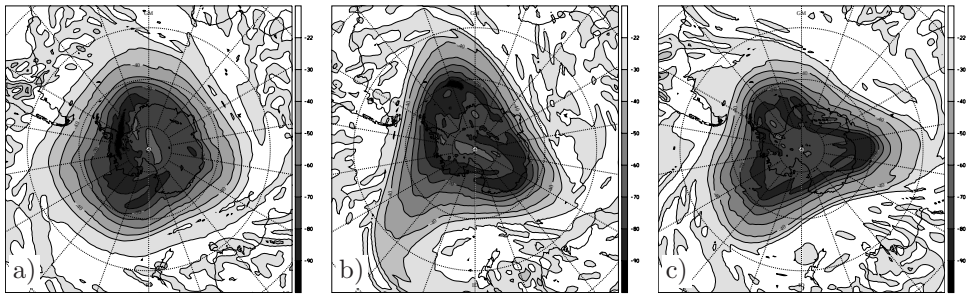

Figure 4.9: PV distribution (shaded in pvu) on the southern hemispheric 500 K isentrope at (a) 00 UTC 01 September 1999, (b) 00 UTC 06 September 1999 and (c) 00 UTC 11 September 1999.

retains a pseudo-meridional perspective (see Section 2.2).

The following analysis is carried out separately for the middleworld and several characteristic global configurations of the overworld, that include a disrupting polar vortex during northern hemispheric late winter and a stationary vortex in the southern hemisphere.

4.2.1 Middleworld

The dispersion values are quite high[1] (Fig. 4.11a). The extratropical tropopause is clearly signaled by a region of high dispersion, in particular for $\sigma(48\,\mathrm{h})$. Within the tropospheric part of the extratropical middleworld, the dispersion seems not to be related to the small range of PV values (from 0 to 2 pvu) and within the stratospheric part, slightly weaker dispersion can be found towards the pole.

In the middleworld, variance of the dispersion is clearly correlated to the mean dispersion value and shows high values along the tropopause for the 48 h trajectories. For longer trajectories of 5 days length, the correlation between PV and dispersion resp. variance becomes weaker (Fig. 4.11b) resp. Fig. 4.12b).

To provide an alternative perspective, selected PV contours are shown at several characteristic levels at the time the trajectories have been initialised (Fig. 4.13). The extratropical tropopause exhibits undulations in the western hemisphere and a relative undisturbed region over eastern Asia. This is typical for late winter and not discussed further within this context.

The subtropical tropopause (contours on 360 K) is undisturbed and zonally aligned, except for a region over the western Pacific, and features strong isentropic PV gradients. A local minimum in dispersion and variance is collocated in the equivalent latitude representation (cf. Fig. 4.11 resp. Fig. 4.12).

4.2.2 Overworld ($\theta > 380\,\mathrm{K}$)

In the overworld, both the dispersion values and its variance increase uniformly with longer trajectories (Fig. 4.11b) resp. Fig. 4.12b). Low dispersion values from

[1] The anomaly at the north pole of very low dispersion and high PV values is caused by high PV values occurring within the planetary boundary layer.

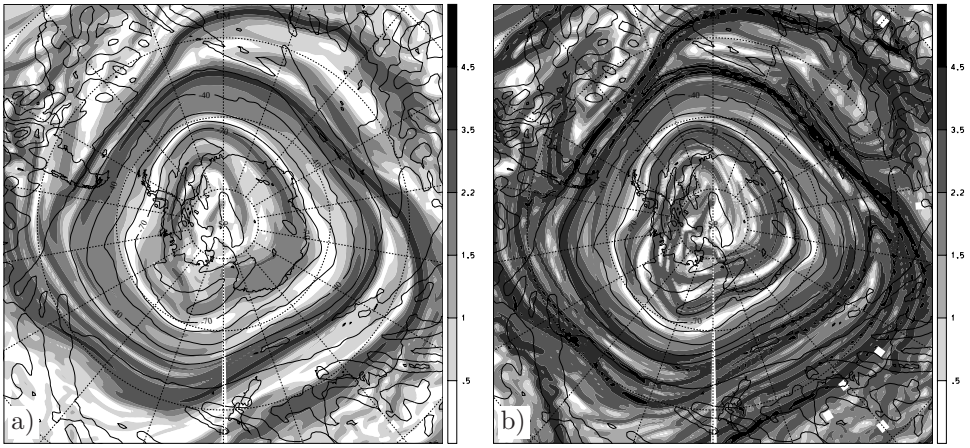

Figure 4.10: (a) $\sigma(120\,\mathrm{h})$ and (b) $\sigma(282\,\mathrm{h})$ (shaded) and PV (thin contour lines, spacing as in Fig. 4.9) on the southern hemispheric 500 K isentrope at 00 UTC 01 September 1999. Greenwich Meridian points upwards.

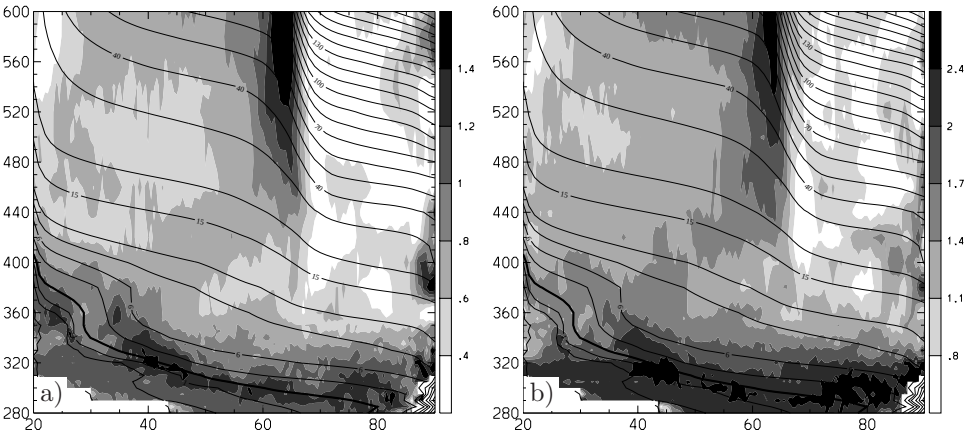

Figure 4.11: (a) $\sigma(48\,\mathrm{h})$ and (b) $\sigma(120\,\mathrm{h})$ (shaded) and PV (contours as in 2.1b) at 00 UTC 01 March 2000 in an equivalent latitude – θ representation.

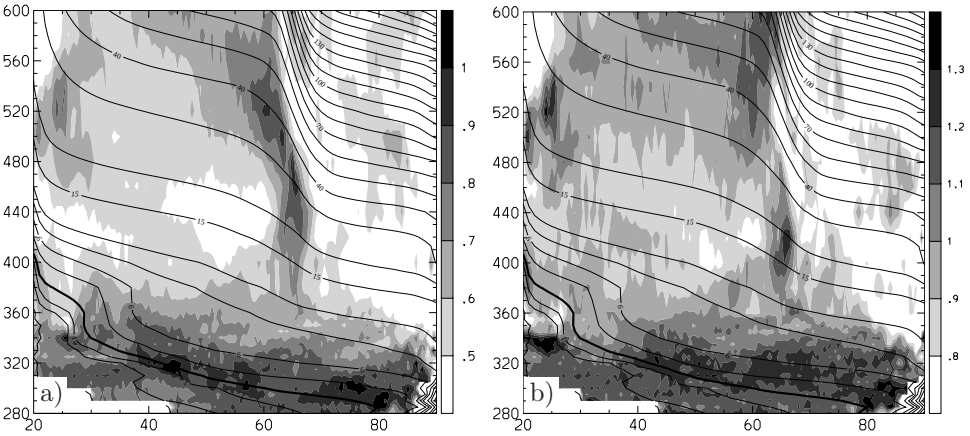

Figure 4.12: The same as 4.11 for dispersion variance (shaded).

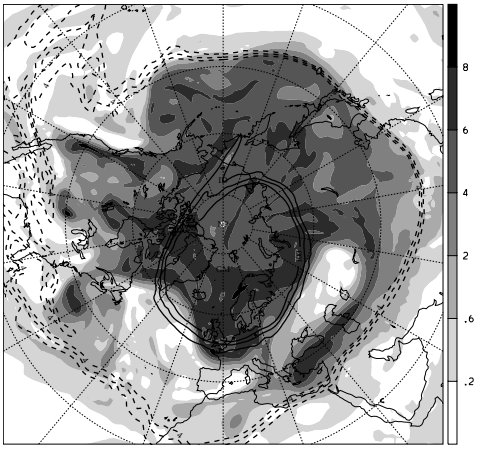

Figure 4.13: PV distribution on 320 K (shaded in pvu), on 360 K (dashed contours of 2,3 and 4 pvu) and on 560 K (solid contours of 60, 80 and 100 pvu) for 00 UTC 01 March 2000.

70°N polewards signal the polar vortex (Fig. 4.11). The outer vortex edge exhibits strong dispersion above 450 K that decreases equatorwards within the surf zone.

The variance of the dispersion values corresponds only partially to the dispersion mean and PV values observed above (Fig. 4.12a). The low variance within the polar vortex reaches further south into the vortex edge, with a high variance at its outermost edge that also decreases towards the tropics. At heights around 400 K where only a weak edge is identified in the dispersion mean, the vortex seems clearly confined by a region of high variance.

Equatorwards, the surf zone is characterised by lower dispersion and, beside the most equatorward region of lowest PV values, of weak meridional PV gradients. That corresponds to lower velocities and a weak link between the dispersion structure and initial PV values. The subtropical tropopause and the polar vortex edge are connected by a region of slightly stronger dispersion (between 40 and 60°N from 380 to 440 K). The dispersion variance is very low in this region.

In the corresponding horizontal PV distribution the polar vortex is found to have a quite stationary geometry apart from a filament indicating vortex erosion in progress at 00 UTC 01 March 2000 (Fig. 4.13).

Polar vortex breakup

The polar vortex disrupts into two vortices on 12 UTC 18 March (Fig. 4.14a). The two vortices get separated and evolve differently. The eastern one is weaker and is strongly distorted whereas the western vortex recovers to a quasi-stable, but small vortex.

The inspection of the corresponding horizontal dispersion structure demonstrates the subsequent disruption by a band of very high dispersion between the connecting filament (Fig. 4.14a). The band of low dispersion along the Pacific side of the filament indicates, that this air mass remains within the western vortex. The overall higher dispersion values within the eastern vortex indicate its subsequent erosion.

Averaged along equivalent latitude, the dispersion reflects the vortex splitting

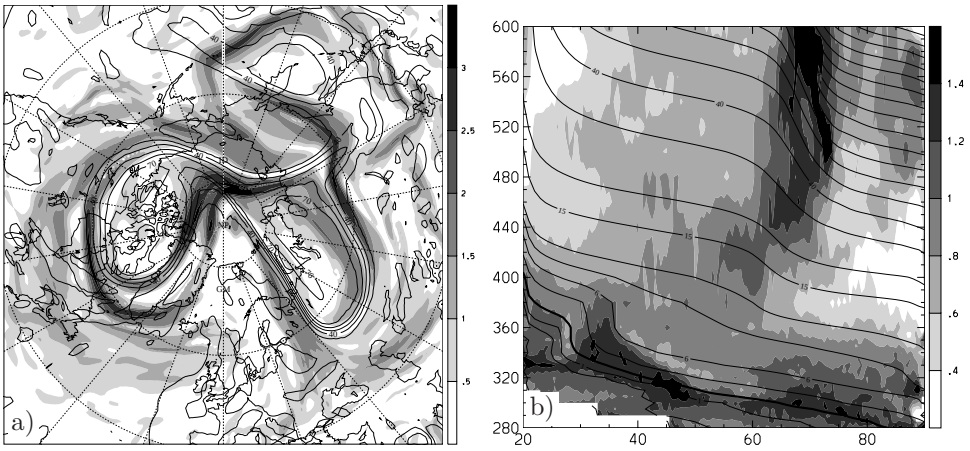

Figure 4.14: $\sigma(24\,\mathrm{h})$ (shaded) at 12 UTC 18 March 2000 (a) at the 500 K isentrope and PV (contour lines reversed from Fig. 4.9) and (b) in equivalent latitude, as 4.11a).

by significantly higher values within the vortex (Fig. 4.14b). The vortex edge is much broader at 500 K because of the dissolution of the PV filaments that still connect the two vortices and the interior of the eastern vortex.

Stable polar vortex

Finally, the stable southern hemispheric polar vortex discussed in Section 4.1.5 is briefly discussed.

In Figure 4.15a), the dispersion minimum at the vortex edge can be discerned clearly now as a function of equivalent latitude. The band of higher dispersion between the vortex edge and the subtropical tropopause as found for the northern hemispheric case is not present and the minimum within the subtropical jet at the tropopause is significantly weaker. The structures of the outer edge and the surf zone are very similar to the cases previously discussed.

Despite the zonal symmetry of the vortex, the dispersion in the zonal mean exhibits a vague structure. The vortex edge is broader, a second maximum of dispersion is found polewards and within the surf zone, and the dispersion decreases not monotonically equatorwards.

4.3 Characteristic time scale and seasonal variability

The comparison of dispersion distributions and averaged values of different trajectory length reveals a pronounced increase of dispersion for longer trajectories (see e.g. Figs. 4.3, 4.10 and 4.11). This fact is employed to assign a characteristic time τ to each isentrope describing a mean mix-down time of a tracer ingestion or a generation rate for small-scale features.

Probability distribution functions (PDFs) of area weighted dispersion for several isentropes demonstrate how the values increase more slowly with increasing θ (Fig. 4.16). For the middleworld, i.e. 320 K, dispersion values > 4 are found already after

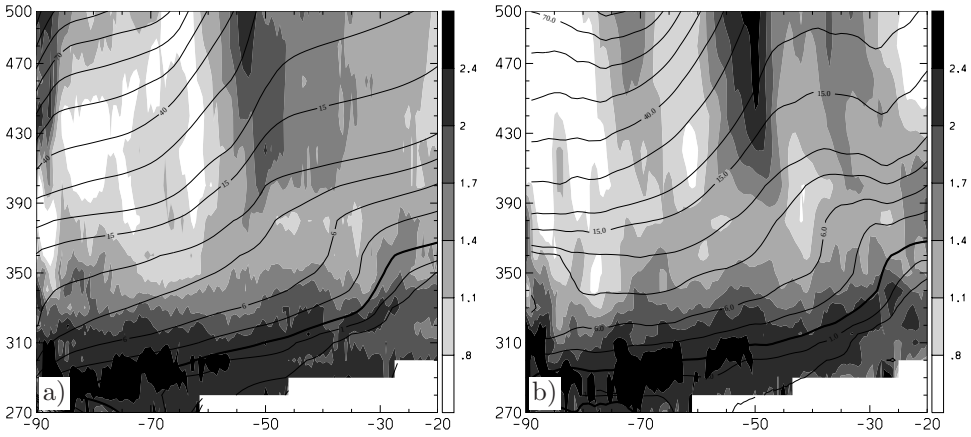

Figure 4.15: (a) As 4.11a) for the southern hemispheric $\sigma(120\,\mathrm{h})$ at 00 UTC 1 September 1999 and (b) zonal mean of the same quantities.

3 days and with increasing time, a saturation around 5.5 can be identified that is caused by the sphericity of the earth. An estimate for typical particle separations that correspond to $\sigma = 5.5$ can be easily obtained by the assumption of an ensemble of n trajectories starting on a 0.5° grid in mid-latitudes (e.g. with an initial distance of $\sim 20\,\mathrm{km}$ to the mean position).

$$\begin{aligned} \sigma &= \log \sqrt{\frac{n(X)^2}{n(20\,\mathrm{km})^2}} = 5.5 \text{ , thus} \\ X &= 20\,\mathrm{km} \cdot e^{5.5} \simeq 5'000\,\mathrm{km} \end{aligned}$$

corresponding to a uniform distribution along 45°N and a mean position at the pole for an ensemble of three trajectories.

To circumvent a significant impact of the saturation effect on the PDF, a mean value of $\langle\sigma(\tau)\rangle = 1.5$ is used to define a characteristic time τ for the corresponding isentrope. For $\langle\sigma(\tau)\rangle > 1.5$, the right part of the PDFs is affected by the upper bound discussed above (cf. Fig. 4.16). At several time instances, τ is calculated on various isentropes and shown in Fig. 4.17.

In the overworld, τ increases with height to 7 to 8 days consistently for all cases. The strength of increase with height seems to be related to the stability of the vortex. For heights above the maximum though, a stable vortex results in a slightly smaller τ because of the stronger shear at the vortex edge.

In the middleworld, the higher dispersion reduces τ to synoptic time-scales of three to four days. The shift of about one day between the two cases in March 2000 (solid and dotted lines) and the other northern hemispheric one in September (dashed lines) is difficult to interpret, but could indicate a seasonal cycle.

The seasonal variability within the middleworld is therefore examined using forward trajectories initialized two times twice monthly on selected isentropes from 1979 to 1993 (see Chapter 5.4 for description of the dataset and the isentrope selection approach). The monthly mean dispersion as a function of equivalent latitude exhibit a clear seasonal cycle with a more confined region of high dispersion at the tropopause in winter than in summer (Fig. 4.18a). The corresponding variance implies a weaker relationship with PV in summer (Fig. 4.18b), similar to the structure

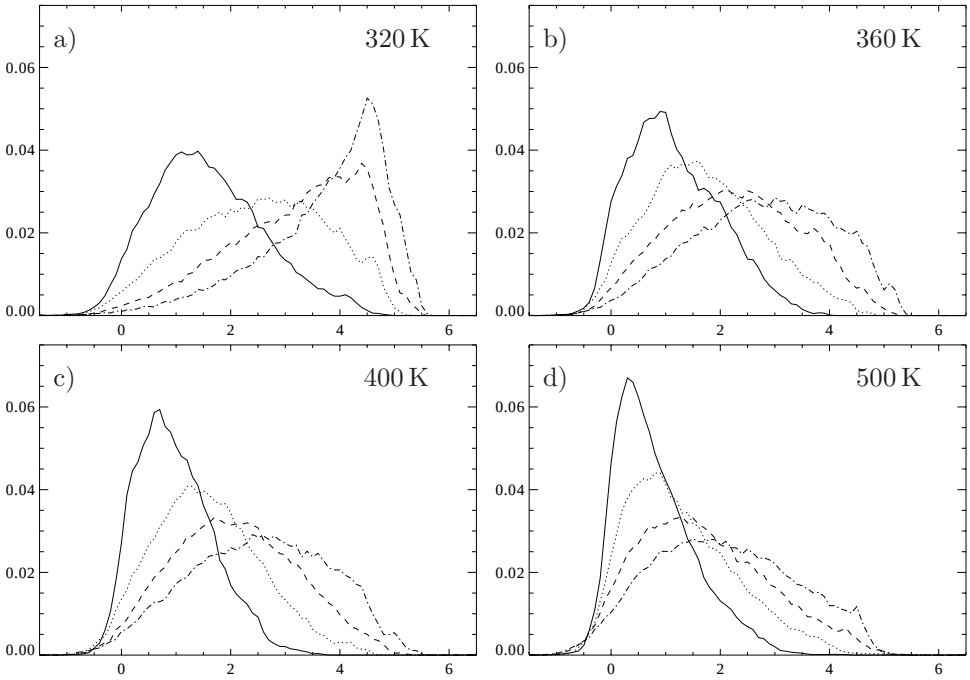

Figure 4.16: PDFs of area weighted $\sigma(3d)$ (solid), $\sigma(6d)$ (dotted), $\sigma(9d)$ (dashed) and $\sigma(12d)$ (dash-dotted) for the (a) 320 K, (b) 360 K, (c) 400 K and (d) 500 K isentropes.

observed for longer trajectories in the previous section. The broader region of high dispersion in summer results in a smaller τ, but note that higher isentropic levels were chosen during summer (see Fig. 5.2a).

The geographical distribution for the winter and summer months (Fig. 4.19) confirms the above picture. The winter distribution is more confined along the tropopause and to the regions associated with the storm track (see next Chapter). It exhibits a pronounced minimum over Eastern Asia and a weaker one over Northern America. Some isentropes cut the boundary layer in the Himalayan region causing anomalously high dispersion.

In summer, high dispersion values are distributed meridionally in a broader band and exhibit less variation along the PV contours. A relative minimum can be detected over Eastern Europe and a maximum is found over Eastern Asia in the same regions where a miminum occurred during in winter.

4.4 Synthesis

The distribution of relative dispersion is dominated by bands of high values around the mid-latitude tropopause. Lyapunov exponents exhibit a similar distribution with a tropopause maximum (Pierrehumbert and Yang, 1993; Stohl, 2001). The inspection of individual features in the richly structured horizontal dispersion distribution reveals that:

- The bands of high dispersion separate pools of air masses that subsequently exhibit a coherent behavior (i.e. of low dispersion).

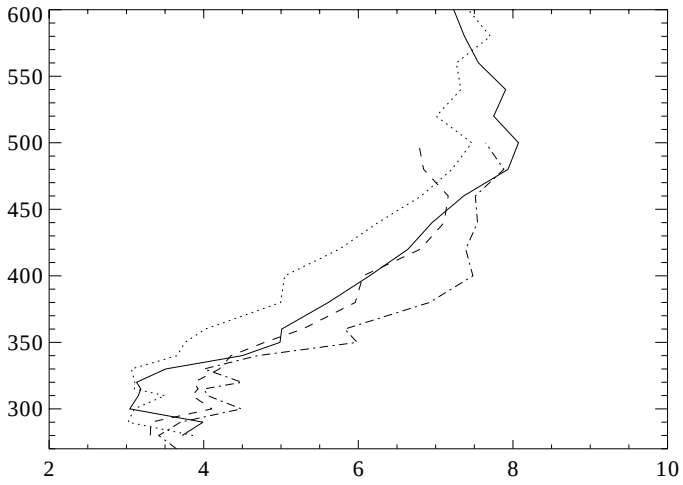

Figure 4.17: Characteristic time (horizontal axis, in days) for different isentropes (vertical axis, in K) for the cases of 00 UTC 1 March 2000 (solid), 12 UTC 18 March 2000 (dotted), 00 UTC 01 January 1999 (dashed) on the northern hemisphere and 00 UTC 01 September 1999 on the southern hemisphere (dash-dotted).

For example, the juxtaposition of a mesoscale vortex and a jet-stream leads to a disruption of the air masses between the jet and the vortex: one part is advected around the cut-off, whereas the other one remains influenced by the jet-stream. Likewise, the air masses within a disrupting polar vortex are clearly marked according to their subsequent separation.

- There is a close relationship to the PV values of the corresponding trajectories.

  A mesoscale cut-off with high PV values is associated with particle trapping in the center and enclosed by a ring of high dispersion and this dispersion pattern can even outlive the PV signature. On the global scale, the interior of a stationary polar vortex is characterized by low dispersion.

A statistical evaluation shows that there are three regions in the over- and middle-world with differing characteristic behavior:

Polar vortex: The overworld reveals a systematic correlation between PV and dispersion. High dispersion is found at the outer edge of the polar vortex that continuously decreases towards the equator and low values characterize the interior. A subsequent disruption of the vortex is identifiable by higher values and the absence of a line of separation. The dispersion patterns are not highly sensitive to the trajectory length in the overworld, characteristic features can still be recognized with lengths of up to 12 days.

A continuous band of low dispersion along the polar vortex edge neighboured by two high dispersion bands are identified. This structure can be associated with the trapping of particles within the continuous jet forming a barrier for transport across the edge (Bowman and Chen, 1994). This is consistent to a minimum in contour lengthening rate, also referred to as “line of separation”, observed in other studies (Pierce and Fairlie, 1993; Chen et al., 1994). Similar result were also found in a barotropic model with a minimum of Lyapunov exponents at the vortex edge by Bowman and Chen (1994). Due to the alignment with the jet core, this kind of barrier is also referred to as “central barrier” (del Castillo-Negrete and Morrison, 1993; Yang, 1998) and is the

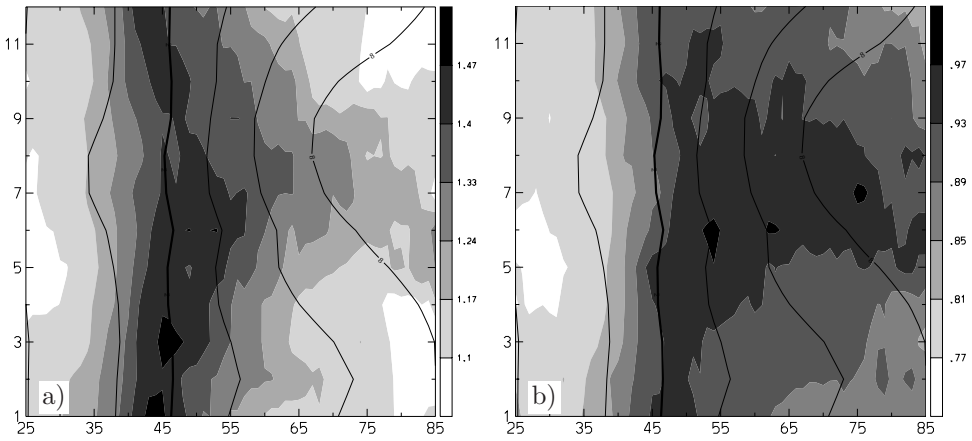

Figure 4.18: 1979 to 1993 monthly mean of (a) $\sigma(48\,\mathrm{h})$ (shaded) and (b) corresponding averaged variance (shaded) in equivalent latitude on northern hemispheric isentropes within the middleworld and corresponding PV values (contour lines, spacing as in Fig. 4.5a).

basis for the identification of transport barriers using "effective diffusivity" (Haynes and Shuckburgh, 2000a,b). All theses studies deal with bands that are continous around the globe.

Filamentation at the outer vortex edge, also referred to "stripping", is associated with stirring and erosion of the outer edge and has been identified by high dispersion bands from the edge reaching into the surf zone. The vortex stripping is located equatorward from barrier region within the polar vortex edge.

Subtropical tropopause: In one case, a relative minimum in dispersion is found at around 350 K collocated with the region of strong PV gradients that is associated with a very regular subtropical jet-stream. It could be the signature of a line of separation indicating the presence of a sub-tropical tropopause barrier. CAS calculations and contour lengthening rates at 330 K also indicate a transport barrier at the sub-tropical tropopause (Bithell and Gray, 1997). Further, a minimum in the contour lengthening rate at the tropopause can be identified in sub-tropics using the effective diffusivity technique (Haynes and Shuckburgh, 2000b).

Extra-tropical tropopause: On tropopause levels, the line of separation is only found in confined regions along elongated synoptic-scale jets. Further, the line is not exactly parallel to the PV contours, sometimes located on the stratospheric, sometimes on the tropospheric side. This indicates that the tropopause is of much higher permeability with permanent exchange in both directions. In contrast to higher levels, the absence of a transport barrier at 310 K was also described by (Bithell and Gray, 1997). The authors also note, a particular single PV value does not represent a global barrier at any particular instant, it may only serve well for a given local synoptic development. Further, a Lyapunov exponent analysis at 315 K based on coarse (T35) resolution model winds shows little evidence for a mid-latitude transport barrier Pierrehumbert and Yang (1993).

In contrast to this results, the minimum of effective diffusivity found in the sub-tropics is also present for the tropopause in mid-latitudes (Haynes and Shuckburgh, 2000b). The authors argue, that the time-scale for a particle to leave the barrier region is less than the time-scale necessary to define the

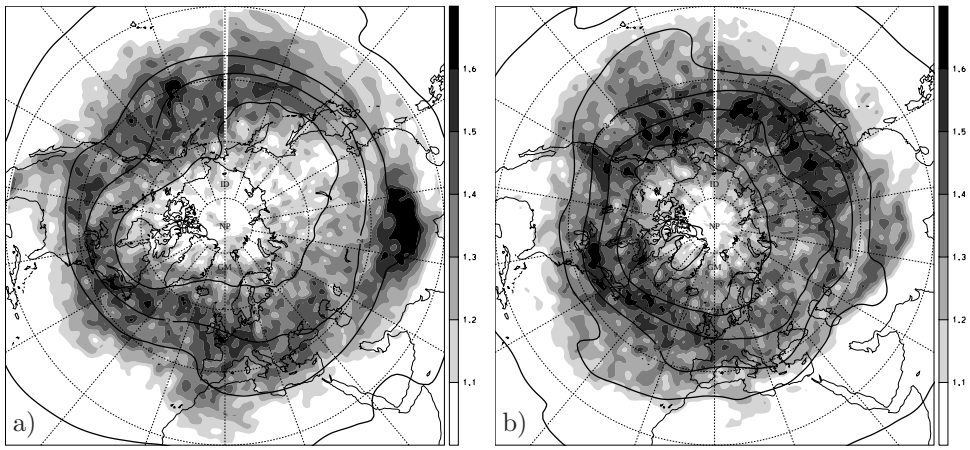

Figure 4.19: Seasonal mean of $\sigma(48\,\mathrm{h})$ (shaded) for (a) winter and (b) summer and monthly averaged PV as isolines (0.2, 0.8, 2, 4, 6 and 8 pvu) for (a) January and (b) July from 1979 till 1993.

stretching rate, but the effective diffusivity would not be affected by this since it is based on the instantaneous length of the tracer contour. Also, the use of coarse wind fields of T42 and T106 resolution to drive the advection-diffusion model for the effective diffusivity diagnosis could result in differing characteristics of the tropopause, since the dispersion of trajectories of only 48 h length does not exhibit the expected minimum.

The methodology applied within this study is able to resolve the zonal distribution of transport characteristics and points to a high permeability of the mid-latitudinal tropopause with only localized barrier structures.

Quasi-horizontal tropopause erosion at the tip of a stratospheric intrusion and at the edge of a stratospheric cut-off indicate analogous stirring processes acting at tropopause levels as for the polar vortex edge. This is consistent to the filamentation of stratospheric air within the troposphere that was found around a streamer by CA simulations (Appenzeller et al., 1996) and was also documented for a cut-off low using measurements, analysis fields and trajectories Gouget et al. (2000). Rossby wave breaking in idealized model simulations suggest the waves sharpen and maintain the extra-tropical tropopause break (Ambaum, 1997). Other studies emphasize the role of baroclinic wave breaking resp. eddies in particular (Haynes et al., 2001). For the real atmosphere though, the PV gradient at the tropopause is presumed to be formed by the interaction of various processes including diabatic ones.

In contrast to the polar vortex edge, the vortex stripping and the barrier structures along the extra-tropical tropopause are located along the same PV contours. The intermittent features of barriers and stirring are related to the localized nature of PV frontogenesis (Davies and Rossa, 1998).

From the examination of instantaneous horizontal distributions, strong tropopause undulation are associated with particular high dispersion values (see Fig. 4.1). Hence, the high dispersion values at tropopause levels are related to regions with intrusions, extrusions and strong jet-streams. A similar relationship for Lyapunov exponents was documented by Stohl (2001). The seasonal cycle with a broader maximum with weak zonal variation in summer and slightly higher values confined to the tropopause regions of the storm tracks in winter indicate that the statistical results of the present study should be

reflected in the tropopause variability.

Although wind speed and PV gradients are significantly lower at tropopause levels than at the polar vortex edge, the dispersion values are considerably higher. The correlation between PV and dispersion was found to decrease much stronger with increasing trajectory length.

Implications for the CA and RDF techniques are that the skill of the reconstruction may be highly sensitive to the trajectory length on tropopause levels and that they must be undertaken with care in this region. The characteristic time scale indicates a maximal length of around 3 days (see Section 3.1.4). However, at higher levels, the reconstructions are expected to be much less sensitive to the integration time. In fact, stratospheric RDF calculations carried out with trajectories of 7 to 8 days length are compatible with the characteristic time scale for this levels (see Section 2.4.2).

Chapter 5

Rudiments of a Climatology of Eulerian Structures

5.1 Introduction

The relevance of tropopause level anomalies in mid-latitudes for the underlying weather systems and transport processes is indicated by the previously presented case studies and dispersion analyses. This PV anomalies of synoptic temporal and spatial scale are associated with undulations of the tropopause and mainly emerge from Rossby waves and their breaking. It is not fully clear however, when and where the maximum upper-level variability occurs in climatological sense. In this chapter, a climatology of isentropic PV variability is developed that treats positive and negative anomalies separately. It provides a unique dataset to address various aspects of the geographical and seasonal variability of near-tropopause anomalies.

In the mid-latitude troposphere, regions with a high frequency of cyclones are often referred to as "storm tracks" (Petterssen, 1956). Diagnostic analysis of 500 hPa geopotential height fields reveals the existence of confined regions of large 2-6 day band-pass filtered variance across the northern Atlantic and Pacific that can be associated with a high rate of alternation between cyclones and anticyclones (Blackmon, 1976). The variability can be interpreted in terms of finite-amplitude baroclinic waves whose structure and evolution varies with the geographical location (Wallace et al., 1988). Although both low and high pressure systems contribute to the variance, the cyclonic disturbances dominate the variance maxima due to the smaller scale, but larger amplitude and higher traveling speed of the cyclones (see Bresch, 1998, also for a detailed review).

The strong link of tropopause level PV variability with the underlying structures is documented in various studies (e.g. Hoskins et al., 1985; Davis and Emanuel, 1991; Morgan and Nielsen-Gammon, 1998). An early climatology of this variability for the winter seasons over 25 years uses the reconstruction of the velocity field on the 315 K isentrope from twice-daily temperature and geopotential fields (Brunet et al., 1995). They locate the low and high frequency contributions of the dynamical and residual transient forcing of the PV variability. As an extension, a 10-winter investigation on 25 isentropes from 275 - 490 K was carried out by Edouard et al. (1997) using daily ECMWF analysed wind fields. They decomposed the flow temporally and dynamically to assess the diabatic, divergent and rotational PV budget on these surfaces with respect to the vertical and geographical location and show that, by calculating pseudo-momentum wave activity, PV can be linked to (conservative) Rossby waves. Some of these techniques were then applied to 39 winters of NCEP reanalysis data with an additional focus on low-frequency variability by Derome

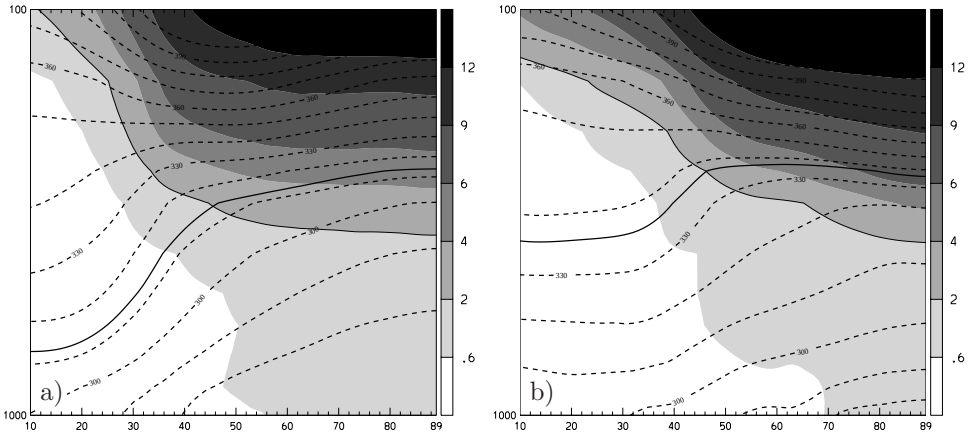

Figure 5.1: Latitude – height cross-sections of northern hemispheric zonal mean of PV (shaded, in pvu) and θ (dashed lines from 280 to 400 K with a spacing of 10 K) for (a) January and (b) July from 1979 till 1993. The solid lines denote the isentropes cutting the PV = 2 pvu at 45°N.

et al. (2001).

The isentropic PV distribution derived from NCEP monthly mean wind and temperature fields are utilized for the study of the low frequency variability and the correlation with Atlantic and European precipitation patterns by Massacand (1999); Massacand and Davies (2001a,b). The results of principal component analysis (PCA) corresponds to low frequency indices as the Northern Atlantic Oscillation (NAO) and Pacific North American pattern (PNA) and leads to the definition of a third index that is linked to European precipitation, the Mid-latitude Anomaly Train index (MAT). But statistics of local PV values are related to technical difficulties because of the bimodal structure found in temporal PDFs of PV (Swanson, 2001). How far the structures inter-annual and geographical variation affects the physical interpretation of PV statistics remains unclear. It is further to note, that also other diagnostics have a non-gaussian distribution.

Specific upper-level processes need not be identified not by PV value but by its structure or alternative quantities. For instance, the seasonal and geographical variability of tropopause folds in mid-latitudes is discussed using Q-vector diagnosis on isobaric surfaces by Elbern et al. (1998). The variability of Rossby wave breaking on the 350 K isentrope is analysed by the meridional PV structure for the sub-tropics (Postel and Hitchman, 1999).

After a description of the data set used for this study (Section 5.2), the conventional approach of mean and standard deviation is presented (Section 5.3). Then, the technique for a climatology of positive and negative upper-level PV anomalies is developed (Section 5.4) and the seasonal variation of the geographical anomaly distribution and its variability is examined (Section 5.5). A closer description of the statistical PV distribution (Section 5.6) and the special case of strong positive anomalies are investigated (Section 5.7). The results are then compiled and interpreted (Section 5.8).

5.2 Data set

The ERA-15 dataset, introduced in Section 2.1 and available on a 1° grid, is used hereafter for the calculation of PV and its interpolation onto isentropes. In place of considering all winter and summer months (as in the studies reviewed in Section 5.1), January (July) is used for winter (summer) as a representative month. This restriction results in sharper patterns.

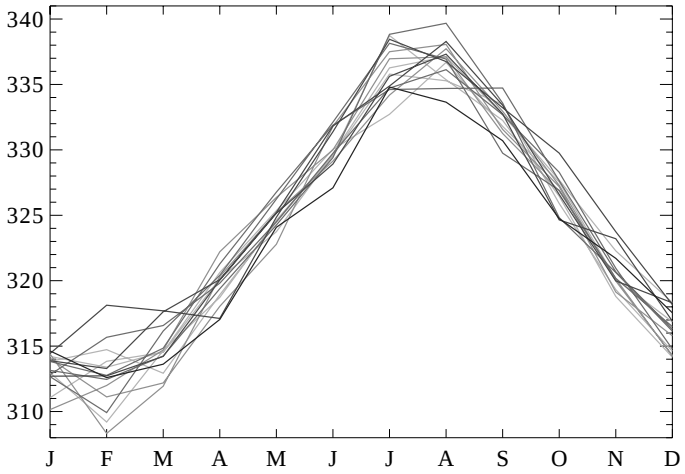

Figure 5.2: θ (in K) of isentrope that cuts $PV = 2\,\mathrm{pvu}$ isosurface in monthly zonal mean at 45°N in dependency of month. Each line represents a year from 1979 till 1993, with earlier years brighter.

An inspection of θ and PV in the zonal monthly mean reveals a strong seasonal variation (Fig. 5.1). The study of one particular isentrope (e.g. $\theta = 330\,\mathrm{K}$) for the whole year would result in a strong meridional shift of the dynamical tropopause on the selected isentrope (from 35°N in January to 65°N in July). Therefore, a separate isentrope is selected for each month based on the criterion that in the zonal monthly mean it crosses the PV = 2 pvu surface at 45°N. This permits a focus on the tropopause variability in the mid-latitudes. The resulting θ values vary from 308 K in winter to 338 K in summer (Fig. 5.2).

5.3 Conventional approach

The climatological PV mean for January resembles and relates to the typical stationary wave pattern (Fig. 5.3a). Strong troughs and PV gradients are found over eastern North America and, less pronounced, over eastern Asia. They can be associated with the beginning of the corresponding storm tracks. The ridges are positioned downstream of the troughs, about 90° further east over the Pacific and about 60° over the Atlantic. A weakening of the meridional gradients on the tropospheric side is found close to the negative ridges over California and Spain at the end of the storm tracks. The Eurasian continent is characterized by weak gradients. Some isentropes cut the boundary layer in the Himalayan region where anomalous PV values can be caused by frictional processes. A region of significant lower meridional gradients is found between the trough and the ridge over Alaska only for the Pacific storm track. In opposition, the gradients of Atlantic storm track weaken downstream of the ridge at the end of the storm track. Also, the maximum in

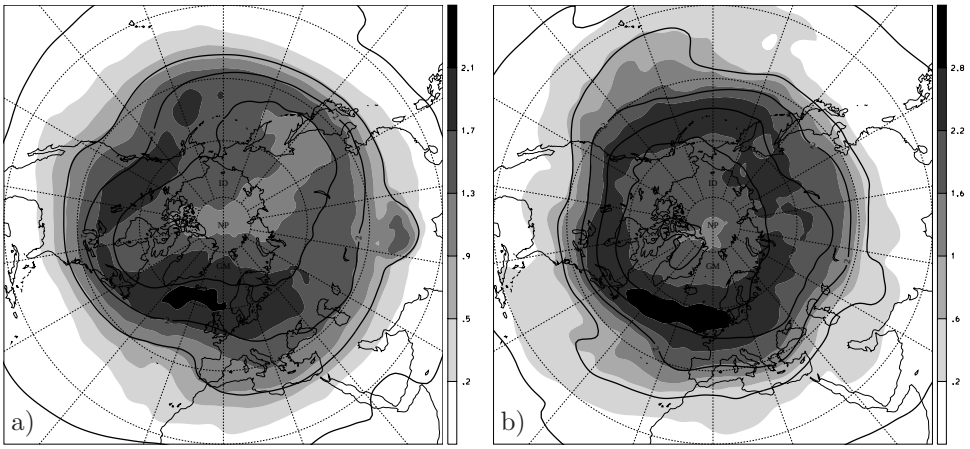

Figure 5.3: Monthly averaged PV (contour lines of 0.2, 0.8, 2, 4, 6 and 8 pvu) from 1979 till 1993 for (a) January and (b) July and standard deviation (shaded, note the different contour spacing between (a) and (b)).

variability at the end of the storm track is much stronger and broader over Europe.

The overall structure of the January standard deviation is similar to the winter PV values calculated in several studies (e.g. Derome et al., 2001). The highest variability is located between the 2 and 4 pvu mean PV values. i.e. it is meridionally shifted towards stratospheric values. Zonally, the maxima are collocated with the storm track. The Pacific storm track is weaker, narrower and there are indications that it consists of two relative maxima, one collocated with the trough over the western North America and a weaker one over the North Pacific upstream of the trough. Within the climatological troposphere, the variance is rather small. The standard deviation correlates well with the mean PV value, as noted and utilised for a description of the PV variability as a function of the PV value in Swanson (2001).

In July, the PV mean exhibits a less pronounced wave structure (Fig. 5.3b). In particular, the Eastern Asian trough and the ridges over the mid-Atlantic and eastern Pacific are not clearly identifiable anymore. Nevertheless there are some noteable deviations from the zonal mean: Over the Pacific and North Atlantic there is southward extension towards the sub-tropics.

The standard deviation is significantly higher than in January and exhibits a weak zonal variability. Again, there is a good correlation between PV mean and variance with the maximum located between 4 and 6 pvu.

5.4 Methodology

As an alternative approach to the standard deviation describing the PV variability a methodology is assessed hereafter to define PV anomalies as a deviation by a certain threshold value ΔPV from the climatological mean $\overline{\mathrm{PV}}$. This technique is designed to identify positive (PA) and negative (NA) anomalies separately with the same weighting for January and July. Therefore, the PDF of PV for the different months is first investigated in detail in order to objectively define appropriate threshold values. Further, positive (negative) PV anomalies are only considered within the

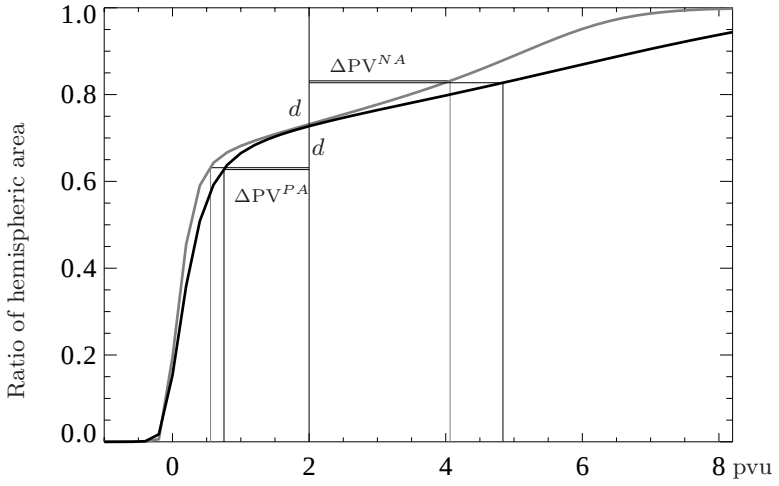

Figure 5.4: $\mathrm{CDF}_{Jan}(\mathrm{PV})$ (grey) and $\mathrm{CDF}_{Jul}(\mathrm{PV})$ (black), see text for further explanations.

climatological troposphere (stratosphere).

In the zonal mean, the vertical stratification $\partial\theta/\partial z$ in the stratosphere is significantly stronger in July and a corresponding larger vertical PV gradient can be observed (Fig. 5.1). To quantify this feature, cumulative distribution functions CDF(PV) are calculated for the corresponding months by integrating the PDF of PV PDF(PV) over the whole Northern Hemisphere (A) on the selected isentropes:

$$\begin{aligned} \mathrm{PDF(PV)} &= \frac{1}{A}\int_A \cos(\Phi)\,\delta(\overline{\mathrm{PV}'(\Psi,\Phi)} - \mathrm{PV})\,d\Phi d\Psi \\ \mathrm{CDF(PV)} &= \int_0^{\mathrm{PV}} \mathrm{PDF}(\mathrm{PV}')d\mathrm{PV}' \end{aligned}$$

Ψ denotes longitude, Φ latitude and δ the Dirac delta function. The result for every January $\mathrm{CDF}_{Jan}(\mathrm{PV})$ and every July $\mathrm{CDF}_{Jul}(\mathrm{PV})$ from 1979 till 1999 is shown in Fig. 5.4). The weak gradients of PV within the troposphere can be clearly recognized by the steep slope of CDF(PV) for both January and July. The distribution in January is consistent with both instantaneous CDF(PV) (Ambaum, 1997) and localized PDF(PV) in mid-latitudes in a winter climatology (Swanson, 2001). A significant seasonal difference is found in the stratosphere: There are no PV values > 8 pvu in January and the stratospheric PV gradient is constantly weaker than for July.

Now threshold PV values ΔPV are determined for the identification of anomalies in such a way that the area enclosed by the 2 pvu + ΔPV contour deviates by $d = 0.1A$ from the area enclosed by the 2 pvu contour. This approach insures an equal weighting of both NA and PA in January and July. The determination of the threshold values is illustrated in Fig. 5.4 by the horizontal lines at a distance d below (above) the ratio of the hemispheric area enclosed by 2 pvu for the PA (NA) threshold.

The conditions and corresponding threshold values for NA and PA are summarized in Table 5.1. Note, that all PV values with a difference to the climatological mean $\overline{\mathrm{PV}}$ greater than the threshold ΔPV are considered, e.g. a PV value of 3 pvu is counted as a NA, if it is located where the climatological PV value is 6 pvu.

	NA	PA
Condition 1	$\mathrm{PV} < \overline{\mathrm{PV}} + \Delta\mathrm{PV}^{NA}$	$\mathrm{PV} > \overline{\mathrm{PV}} + \Delta\mathrm{PV}^{PA}$
Condition 2	$\overline{\mathrm{PV}} < 2\,\mathrm{pvu}$	$\overline{\mathrm{PV}} > 2\,\mathrm{pvu}$
January threshold	$\Delta\mathrm{PV}^{NA}_{Jan} = -2.1\,\mathrm{pvu}$	$\Delta\mathrm{PV}^{PA}_{Jan} = 1.4\,\mathrm{pvu}$
July threshold	$\Delta\mathrm{PV}^{NA}_{Jul} = -2.8\,\mathrm{pvu}$	$\Delta\mathrm{PV}^{PA}_{Jul} = 1.2\,\mathrm{pvu}$

Table 5.1: Conditions and resulting threshold values for January and July for negative stratospheric (NA) and positive tropospheric anomalies (PA).

The threshold values for the NA (PA) are now applied to every grid point of instantaneous, isentropic PV distributions within the climatological stratosphere (troposphere). A geographical frequency of occurrence is then constructed by counting all grid points fulfilling the outlined conditions for every January resp. July from 1979 to 1993 at the same location.

The method is further illustrated by PDF(PV) along $\Psi = 40°\mathrm{W}$. The technique outlined above considers the part above (below) the black solid line within the climatological troposphere (stratosphere) in Fig. 5.5. Stratospheric PV values dominate the PA, whereas for the NA, tropospheric PV values contribute only in the region from 50 to 75°N in winter and from 50 to 65°N in summer significantly. Due to the sparseness of PV values of less than 0 pvu, a narrow band with very low frequency results directly north of the climatological tropopause. The higher threshold value for the summer stratosphere results in a wider band.

5.5 Positive and negative anomalies

The frequency of positive and negative anomalies are examined hereafter to assess the distribution of their occurrence and their seasonal and geographical variability.

In January, the pattern for the NA frequency is characterized by maxima between 2 and 4 pvu (Fig. 5.6a). The maxima are zonally confined to the climatological ridges with a broad maximum over the middle North Atlantic and a weaker one over the western American continent. The Atlantic maximum broadens towards Europe and separates from the tropopause slightly northwards over Eastern Europe and Siberia. The American one consists of two relative maxima, collocated with the ones observed for the standard deviation (cf. Fig. 5.3a). The minimum over the pole is extended equatorwards towards Eastern Asia and, much less pronounced, towards Eastern North America. The overall structure is very similar to that of the stratospheric part of the standard deviation (cf. Fig. 5.3a).

Qualitatively, the PA frequency on the tropospheric side is also very similar to the standard deviation. But the separate treatment of NA and PA results in more pronounced features. The maxima of PA occurrence are closely aligned with the tropopause and are zonally more elongated than their NA counterpart. The highest frequency is found along the storm tracks, broadening downstream, collocated with the weaker meridional gradients in the PV mean.

In the summer stratosphere, there is a shift of the NA frequency towards higher PV values to around 4 or 5 pvu, depending on the longitude (Fig. 5.6b). The anomaly maxima are found more upstream than in January, both maxima are now

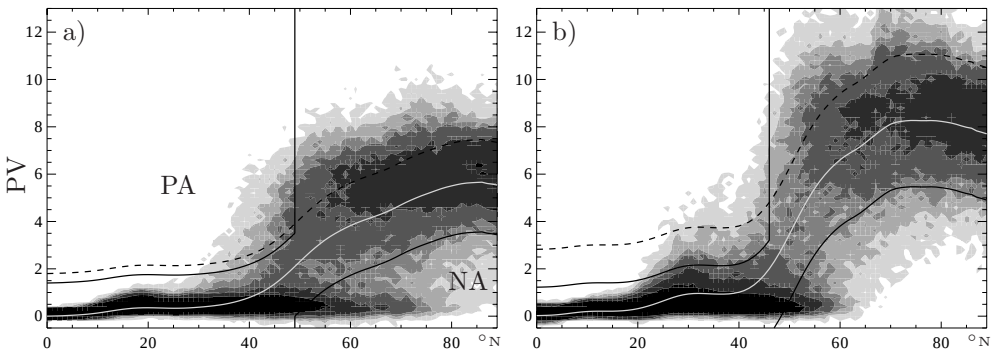

Figure 5.5: Local PV value histograms (vertical axis) along 40°W for (a) January and (b) July (contour values of 0.16, 0.5, 1, 3 and 6%, bin size of 0.2 pvu) for all latitudes (horizontal axis). The grey line denotes the climatological mean $\overline{\mathrm{PV}}$, black solid lines correspond to the threshold $\overline{\mathrm{PV}} + \Delta\mathrm{PV}$ used for positive (negative) anomalies within the climatological troposphere (stratosphere). The black dashed line denotes the same for strong positive anomalies discussed in Section 5.7.

collocated with the oceans. I.e. the Atlantic maximum is shifted only slightly, but the American one is located 60° eastwards over the central Pacific. Again, the Atlantic maximum separates from the tropopause northwards over Eastern Europe.

Over the central North Atlantic and eastern North Pacific, a pronounced southward expansion high PV mean values at the end of the storm tracks can be identified that are accompanied by high frequency of PA stretching westwards along 30°N. A small ridge in the PV mean over Eastern Asia can be identified downstream of the region of weaker meridional PV gradients and the local minimum in anomaly frequency over Eurasia.

5.6 PDF structures

Here the results from the objective PV anomaly identification technique are compared with the mean and standard deviation by consulting local PDF(PV). Skewness and variation of the PDFs are then shown as another perspective to describe the PV value distribution.

Characteristic tropospheric and stratospheric PDFs are shown along a meridian across the Atlantic storm track in winter (Fig. 5.5) and across the trough of weak variability over China (Fig. 5.7).

In general, the tropospheric PDF structure is very narrow (between 0 and 2 pvu) and has a broad tail towards positive values. Within the stratosphere, the characteristics are inversed with a wider distribution (from 2 up to 10 pvu) and a confined tail towards low PV values. Across the Atlantic ridge, the meridional mean PV gradient in the stratosphere is much stronger in summer than in winter (Fig. 5.5). That is due to to the higher PV values in the summer stratosphere and because the tropospheric and stratospheric values overlap over a smaller region. Over Asia, the overlap is very small in winter resulting in a much stronger PV gradient (5.7).

In January the found similarity between anomaly and standard deviation structure is supported by the inspection of the local PDF over the North Atlantic for the tropospheric winter (Fig. 5.5a). With regard to the NA, the structure of the

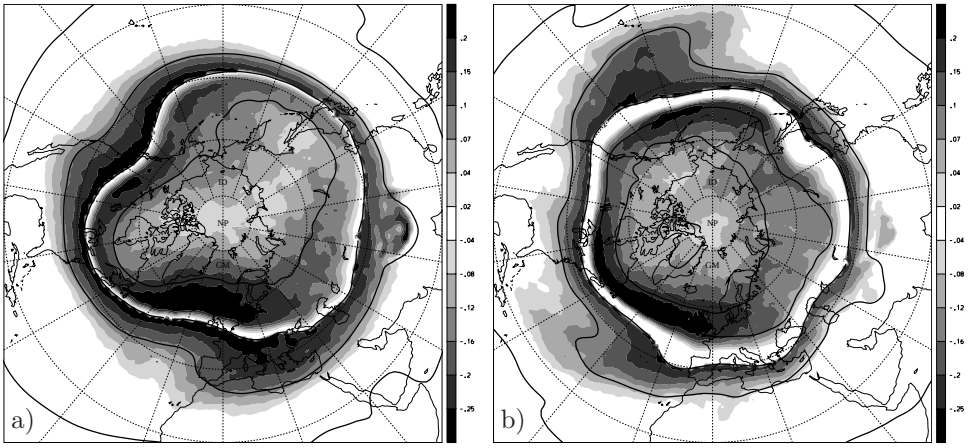

Figure 5.6: Frequency of positive and negative anomalies (shaded) and monthly averaged PV as isolines (0.2, 0.8, 2, 4, 6 and 8 pvu) for (a) January and (b) July from 1979 till 1993. Positive (negative) anomalies are shown only within the climatological troposphere (stratosphere).

PDFs towards higher values from the climatological mean (i.e. the positive tail) is quite independent of the latitude, but strong meridional differences can be seen for the part of the PDFs towards lower values. The same characteristic is found in the local PDFs across the Asian minimum (Fig. 5.7a). For the PA, the similarity is caused by the low variability within the troposphere, that is therefore very sensitive to stratospheric anomalies with high PV values. Further note the weak overlap of tropospheric and stratospheric PV values over the Asian PDFs corresponding to the low anomaly frequencies found in this region.

For July, it was previously observed that the NA maxima are shifted towards higher PV values. Nevertheless, a significant portion of the anomaly frequency is contributed from tropospheric PV values (up to 60°N resp. 6 pvu in Fig. 5.5b). This is possible because of the the overall stronger meridional PV gradient in summer. From the PDFs over the North Atlantic it can be further inferred that for the southward expansion of the PA a large portion of the anomalies are caused by PV values above 2 pvu. The local NA maximum observed around 60°N north of the small ridge (cf. Fig. 5.6b) can further be attributed to a significant portion of tropospheric PV values by the inspection of the PDFs along around 130°E.

Evidently, the PDFs are subject to a strong variability in regard to the location and season. The mean $\overline{\mathrm{PV}}$ and the standard deviation s do not capture all the observed features or their values are strongly affected by some features, as the different range of values north and south of the tropopause. Therefore, the skewness C_s and the variation[1] C_v are employed to describe the characteristics of the PDF structures:

$$C_s = \frac{1}{N}\sum_t \left(\frac{\mathrm{PV}-\overline{\mathrm{PV}}}{s}\right)^3$$

$$C_v = \frac{s}{\overline{\mathrm{PV}}}$$

The skewness C_s describes the asymmetry of the PDF. Accordingly, it is strongly

[1] also referred to as "normalised standard deviation"

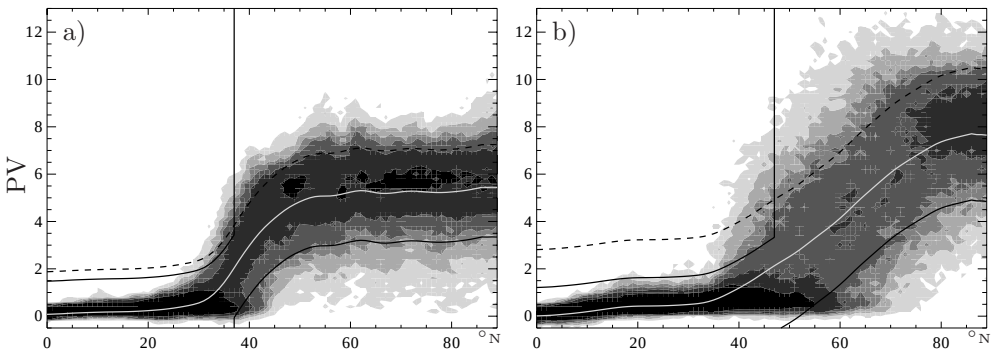

Figure 5.7: The same as 5.5 along 130°E for January and July.

positive within the troposphere. The highest values are associated with PV mean values below 0.8 pvu and a low but not equal zero frequency of positive anomalies (Fig. 5.8). The skewness decreases northwards to zero in the region of the highest variability where the tropospheric and stratospheric values build a symmetric PDF (cf. Fig. 5.5a). North of it, in particular north of the winter troughs, the skewness exhibits moderate negative values. An inspection of local PV PDFs reveals a lack of strong positive values and more tropospheric values (e.g. north of 50°N in Fig. 5.7a and less pronounced in Fig. 5.5a). The weaker negative skewness in the summer stratosphere is related to a higher number of positive values and fewer tropospheric values (as e.g. north of 70°N in Fig. 5.5b).

The meridional shift of the maxima in the standard deviation away from the tropopause towards higher PV mean values is inversed by the calculation of the variation C_v (Fig. 5.9). The PA within the troposphere are weighted much stronger. In winter, the maxima are located south of the ridges along the 0.8 pvu PV mean isoline. The summer maxima are found more upstream, with an extension towards the sub-tropics over both the Atlantic and Pacific. Although the structure is similar to the PA distribution, the strong sensitivity to low PV mean values seems to cause a high spatial variability towards the sub-tropics. The overall difference in magnitude between the winter and summer standard deviation disappears.

5.7 Strong positive anomalies

In the lowermost stratosphere, precursors of surface cyclogenesis can often be identified by anomalous high PV values in the order of 4 to 6 pvu in mid-latitudes. These strong positive anomalies (SPA) within the climatological stratosphere play an important role for cyclonic activity in mid-latitudes and the location and strength of the storm track.

As outlined above, it is likely however, these anomalies contribute only weakly to the standard deviation and since SPA are expected mainly within the climatological stratosphere, they are not considered in the PA frequency. Hence, a new anomaly selection criterion is defined to identify the SPA directly.

The same technique used for the determination of the threshold value for PA within the troposphere (see Section 5.4) is applied now to define SPA within the stratospheric. As a reference PV value not 2 pvu, but 4.8 pvu is chosen. The threshold PV value $\Delta\mathrm{PV}^{SPA}$ is now determined for the identification of anomalies in such

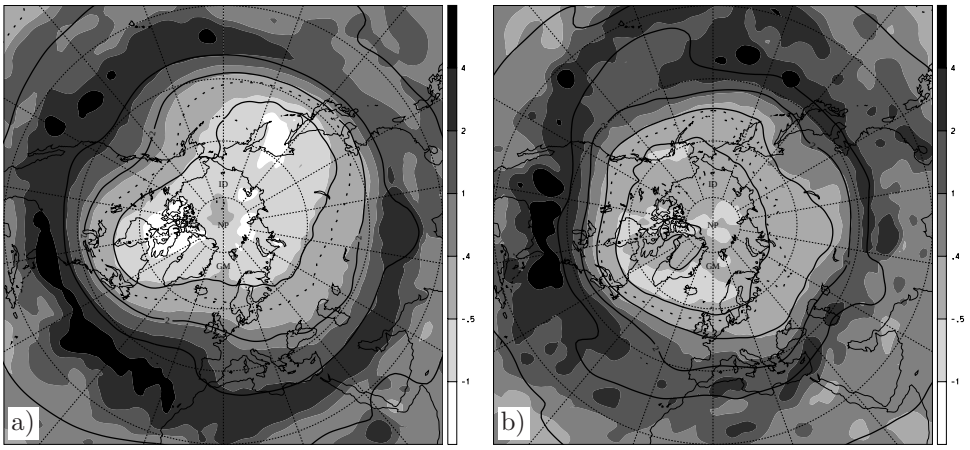

Figure 5.8: As Fig. 5.3 for skewness (shaded).

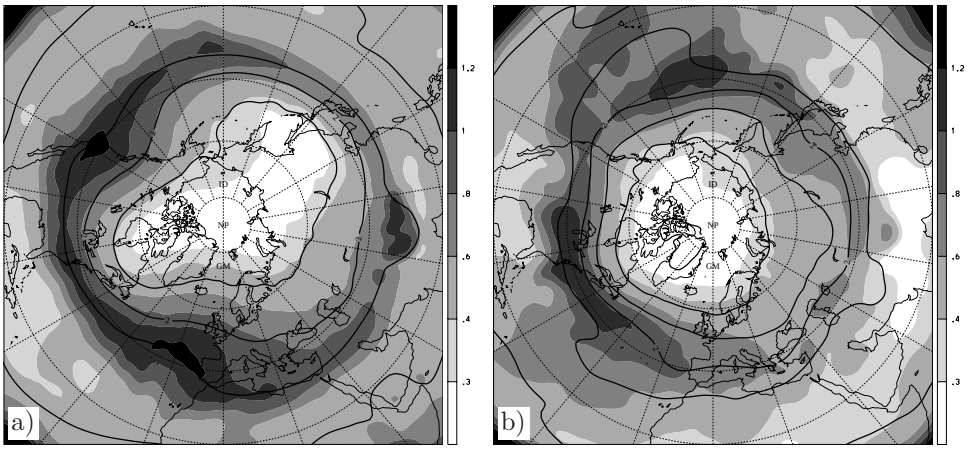

Figure 5.9: As Fig. 5.3 for normalized standard deviation (shaded) .

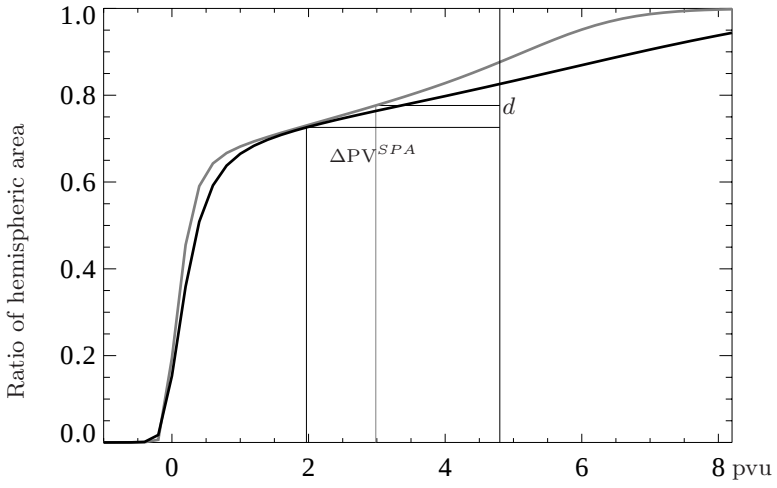

Figure 5.10: The same as Fig. 5.4 with labels for strong positive anomalies (SPA), see text for further explanations.

a way that the area enclosed by the 4.8 pvu + ΔPV contour deviates by $d = 0.1A$ from the area enclosed by the 4.8 pvu contour. This procedure results in in a threshold values of $\Delta PV^{SPA}_{Jan} = 1.8$ pvu for January and $\Delta PV^{SPA}_{Jul} = 2.8$ pvu for July (as illustrated in Fig. 5.10).

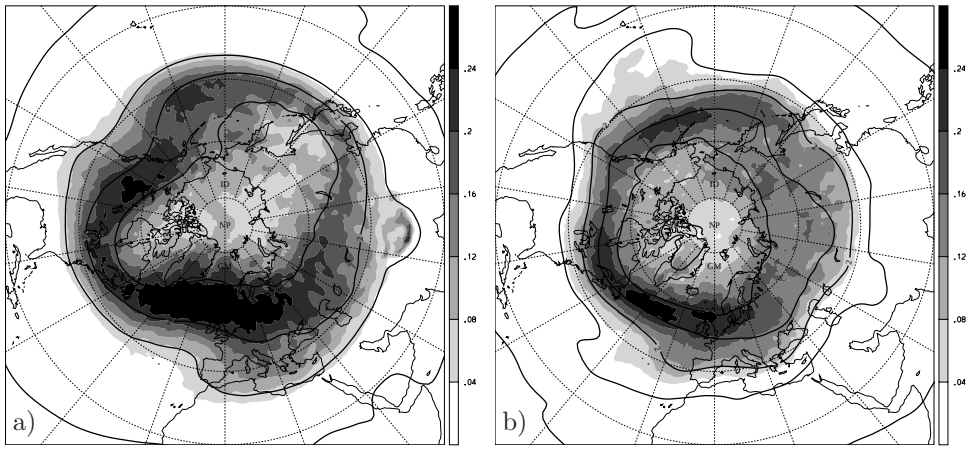

Figure 5.11: Frequency of strong positive anomalies (shaded) and monthly averaged PV as isolines (0.2, 0.8, 2, 4, 6 and 8 pvu) for (a) January and (b) July from 1979 till 1993.

The structures are very similar to the standard deviation and NA distribution both for January and July (cf. Fig. 5.3 resp. 5.6). In particular, the Pacific maximum consists again of two relative maxima, one over western North America and a weaker one over the central North Pacific. Both in January and July, the differences between the Atlantic and Pacific maximum are similar for SPA and for NA. The detailed structure of the storm tracks though reveals some differences: (i) the SPA Atlantic maximum is extended further eastwards into the Eurasian continent than the NA maximum; and (ii) during July, the SPA maxima are clearer confined.

The overall similarity between the stratospheric NA and SPA frequency both in magnitude and pattern, underline the appropriateness of the chosen threshold values with respect to the PV mean values and is strongly related to the structure of the stratospheric local PV PDFs within the climatological stratosphere.

5.8 Synthesis and further comments

The combination of conventional statistical measures, the inspection of climatological, local PDFs of PV and a subjective positive and negative anomaly identification technique enables a comprehensive study of the Eulerian PV variability near the tropopause. The chosen isentropes allow a focus on mid-latitudes for winter and summer.

In January, the region of lowest variability is located upstream of the Pacific storm track separating the two storm tracks over eastern Asia. The Atlantic storm track however is directly connected to the Pacific storm track.

The Pacific storm track differs significantly from the Atlantic one, it is less confined and three regions can be associated with it: (i) over eastern Asia, there is a region of extremely low variability and strong meridional PV gradients that are zonally aligned; (ii) downstream over the central Pacific, the PV gradients are re-

duced on the stratospheric side. Close to the tropopause, a secondary maximum can be identified in all fields describing the stratospheric variability; (iii) and the climatological ridge further downstream over western North America is then associated with maximal variability both within the climatological stratosphere and troposphere. This observed structure for the Pacific storm track could be related to a separation between several regions of Rossby wave developing and breaking. An indication for such a separation is also found by tracing backwards the genesis region of cyclones ending over western North America (Hoskins and Hodges, 2002). The found genesis region is clearly confined and collocated with the region identified as secondary maximum of variability over the North Pacific in this study.

For the Atlantic storm track, these three regions can not be distinguished clearly. The trough over eastern America is more pronounced and exhibits stronger meridional PV gradients. It is directly followed by a slightly less strong ridge over the North Atlantic. The maximum in variability extends from the American east coast all over the Atlantic as far as eastern Europe or even Siberia. It is significantly broader within the climatological stratosphere than its Pacific counterpart. On the tropospheric side, the maximum (of positive variability) is located slightly downstream towards Europe and the Mediterranean Sea.

The July hemisphere features shorter storm tracks with a weaker meridional and zonal variability within the stratosphere. The minimum of variability along the tropopause is not located over eastern Asia but over central Siberia. The Pacific maximum is shifted significantly from western North America to the central North Pacific, both maxima are now collocated with the oceans. There is a stronger asymmetry between the land and ocean domains in the mid-latitudinal upper-levels, although the stronger baroclinicity by the land-sea contrast is supposed to have a particularly strong impact on the atmospheric variability in winter (Hoskins and Valdes, 1990).

Two regions of high variability in the sub-tropical troposphere over the Oceans are found, identifiable clearly in the PA frequency and, weaker, the PV mean and standard deviation. As indicated in Fig. 5.1b), the selected isentropes are located above 500 hPa in the zonal mean. Indeed, an inspection of individual events reveals that these PV anomalies are not located in the lower troposphere, but at upper levels around 200 hPa and thus not related to diabatic effects but rather to sub-tropical Rossby wave breaking. The origin and path of the anomalies can not be captured by the method employed in this study. For the Pacific though, the strong monsoon anticyclone could advect anomalies from western America towards the sub-tropical central Pacific associated with an anticyclonic path. Over the Atlantic, there is no similar anticyclone documented in summer, but the PV mean and the PA frequency indicate an analogous structure of Rossby wave breaking.

Sub-tropical Rossby wave breaking over the oceans was also identified along the tropopause at 350 K in Postel and Hitchman (1999). The authors find the maxima are located slightly more to the west in the regions of the sub-tropical Atlantic and Pacific during summer and their Pacific maximum is twice as strong as the Atlantic one. The westward shift and stronger bias in strength could be related to their method that focuses strictly on the meridional direction of the PV structure, thus a meridional alignment of the anomalies in the form of streamers would reduce the number in their survey.

A small ridge in the PV mean north of China is accompanied by a weak local maximum in NA, SPA and variance. Therefore, the overlap of tropospheric and stratospheric PV values in this region could be a signature of enhanced Rossby

wave breaking. Negative PV cut-offs have been observed in this region and were attributed to the Asian summer monsoon (Popovic and Plumb, 2001). Although the center of monsoon activity is located significantly more to the south, the observed feature could be a signature of variability at higher isentropes.

The local PDFs of PV exhibit a wide heterogeneity. The strong seasonal variation within the stratosphere and the fundamental difference between the tropospheric and stratospheric PDF structure complicates the derivation and use of physically meaningful quantities for statistics. As example, the bimodal structure in the storm track regions is not symmetric. This results in negative anomalies dominating positive anomalies. Nevertheless, the stratospheric variability structure is represented very well by the standard deviation. On the tropospheric side however, features as the sub-tropical extension over the Oceans are not clearly discernible. Thus, the interpretation of local fields of PV standard deviation, skewness or variation has to be carried out very carefully by also considering the corresponding PDF structure directly or employing additional measures.

The results also have implications for the determination of a background PV mean state, as it is necessary for PV inversion (cf. Section 1.3). A strong meridional variability in January (that is more pronounced as the conventional DJF depiction) and a significantly different structure in July for the same latitude is found. Therefore, it is of advantage to assess a spatially and seasonally confined background mean state.

Chapter 6

Concluding remarks

In this study, various characteristics of transport within the middleworld are addressed by employing a case study approach, a Lagrangian perspective and Eulerian statistics. All three approaches resulted in a variety of conclusions that are discussed at the end of the corresponding Chapters. Here, some of these aspects are assembled to draw further conclusions on: (i) the permeability of the tropopause; (ii) and Rossby wave breaking and its relation to stirring.

- There is no continuous line of separation along the extra-tropical tropopause, but only localized along synoptic-scale jets. Further, the bands of high dispersion found in the tropopause region are not exactly parallel to the PV contours. These findings support the thesis that the extra-tropical tropopause can not be seen as a transport barrier and is of much higher Eulerian and Lagrangian heterogeneity than the polar vortex edge in the overworld and thus of a fundamentally different nature in regard to transport processes. Indeed, significantly higher mixing ratios of tropospheric tracers are measured within the lowermost stratosphere than in the overworld (Lelieveld et al., 1997; Fischer et al., 2000). The case studies and inspected dispersion structures in this study indicate that the tropopause is characterized by intermittent regions of cross-tropopause transport and barriers. The intermittency exhibits a high variability in space and time and is strongly related to synoptic-scale structures.

  Indications were found that the subtropical tropopause exhibits a barrier like structure in case of a zonal alignment and a strong jet.

- For equatorward Rossby wave breaking, associated with a stratospheric streamer, strong shear and strong PV gradients, a relatively short life-time with a rapid break-up, and the generation of small-scale structures in its vicinity are some of the observed features. In terms of transport, the streamer rapidly disrupts air streams in a confined region.

  The dynamical counterpart, a tropospheric extrusion, is of wider scale, less striking PV signature in the sense of absolute values and slower evolution, in particular during its disintegration. Within the extrusion, the air masses are stirred strongly in the sense, that there is no link between in– and outflow.

  Although there is this observed asymmetry with respect to transport of poleward and equatorward Rossby wave breaking at tropopause levels, both processes feature bands of anomalously strong dispersion representing the loss of memory of the air mass origin in regard to their destination.

  The rudiments of a dispersion climatology exhibits that high dispersion is linked to the climatological tropopause position and variability in winter. The

correlation with Rossby wave breaking can also be inferred from the geographical distribution. Further, the dispersion is not biased towards the tropo– or stratosphere in January. In summer though, high dispersion occurs mainly within the stratosphere and it is not correlated with the climatological PV structure, in particular not over the Pacific.

This study reveals several implications for localized ingestions of tracers as aerosols and, the analogue backward in time, in situ measurements of conserved tracers:

The rate of tracer dispersion depends strongly on the vertical position. The overworld is associated with more coherent transport and a global dispersion is not expected before eight days, whereas in the middleworld, the same can take place within three to four days. The geographical location within the middleworld itself is of secondary importance, but the vicinity to the tropopause, in particular in winter, favours a rapid dispersion. In respect of measurements, a probed volume of air represents a much larger air mass within the middleworld than for higher levels. Further, the tracers evolution is much more difficult to predict within the middleworld, in particular for the storm track regions in winter, since it is associated not only with high values but also with highest variability of dispersion.

Appendix A

Geometrical Considerations

A.1 Spherical Distance

The conversion of geographical coordinates (λ, Φ) to three-dimensional Cartesian coordinates (x, y, z) provides an efficient way to calculate spherical distances D between two points $\vec{x}_1$ and $\vec{x}_2$ by equation A.1.

$$\begin{aligned} \vec{x} &= \begin{pmatrix} \cos\Phi\cos\lambda \\ \cos\Phi\sin\lambda \\ \sin\Phi \end{pmatrix} \\ D &= R\arccos\left(\frac{\vec{x}_1\vec{x}_2}{|\vec{x}_1||\vec{x}_2|}\right) \end{aligned} \tag{A.1}$$

A.2 Polar Stereographic Projection

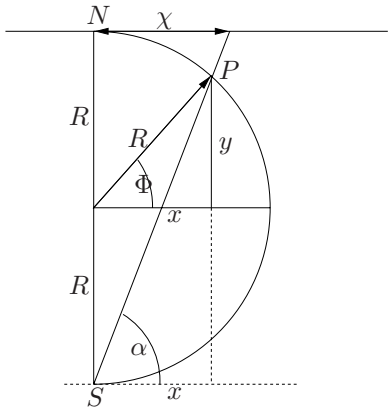

Figure A.1: Cross-section of globe.

The polar stereographic projection, attributed to Hipparchus (2nd century BC), is a perspective projection on a plane tangent to the North (resp. South) Pole. It is conformal, being free from angular distortion. Additionally, all great and small circles are either straight lines or circular arcs on this projection. The projection is not equal area (nor equidistant).

Following Fig. A.1, the geographical point $P(\lambda, \Phi)$ is projected from the South Pole S to a plane, that is tangential to the North Pole N. The geographical latitude Φ is converted to a stereographic latitude χ by the equation A.2.

$$\begin{aligned} \tan\alpha = \frac{y+R}{x} &= \frac{2R}{\chi} \\ x &= R\cos\Phi \\ y &= R\sin\Phi \end{aligned}$$

$$\chi = \frac{2Rx}{y+R} = 2R\frac{\cos\Phi}{\sin\Phi+1} \tag{A.2}$$

(χ, λ) builds a polar representation of the stereographic plane with its origin at the tangential point. A conversion to Cartesian coordinates with the negative ordinate as Greenwich meridian is obtained by:

$$\begin{aligned} \hat{x} &= \chi\sin\lambda = 2R\frac{\cos\Phi}{\sin\Phi+1}\sin\lambda \\ \hat{y} &= -\chi\cos\lambda = -2R\frac{\cos\Phi}{\sin\Phi+1}\cos\lambda \end{aligned}$$

The polar stereograpic projection can be generalized by choosing a different tangent point (resp. the opposing projection origin).

Appendix B

DIAL Technique

After an introduction to the process and measurement of backscattering by a lidar, the priciples of the DIAL in general and the technical specifications of the used DIAL are given.

B.1 Principles of the lidar method

The optical analog of a short-pulse radio frequency radar is called LIDAR (light detection and ranging). The shorter optical wavelengths also interact with scatterers as small as molecules. In the simplest configuration of a LIDAR, a pulse created by a laser is backscattered by molecules or aerosols and collected by a telescope and measured by the detector.

The mean number of backscattered photons received from the range interval $[R - \Delta R/2, R + \Delta R/2]$ during the sample interval $\Delta t = 2\Delta R/c$, can be calculated by the lidar equation (Measures, 1984)

$$S(\lambda, R) = C(\lambda, R) E_0 \beta(\lambda, R) \Delta R \frac{A}{R^2} \exp\left(-2 \int_0^R \alpha(\lambda, r) dr\right), \qquad \text{(B.1)}$$

where $C(\lambda, R)$ is a system function, E_0 is the energy of the emitted monochromatic laser pulse, $\beta(\lambda, R)$ is the total volume backscattering coefficient at range R, $\Delta R = c\Delta t/2$ is the range resolution of the lidar signal, A/R^2 is the acceptance solid angle of the receiving optics with a collecting area A and the last term describes the round-trip transmittance to the range R and back. $\alpha(\lambda, r)$ is the total atmospheric extinction coefficient.

Above a height of 4 km, molecular scattering dominates the scattering by aerosols. Assuming pure molecular scattering, the backscatter coefficient β is due to Rayleigh backscattering and proportional to the Rayleigh extinction α_{Ray}:

$$\beta = \beta_{Ray} = \frac{3}{8\pi} \alpha_{Ray} \ .$$

For light of wavelength λ in the atmosphere below 100 km, α_{Ray} can be calculated by (Collis and Russel, 1976)

$$\alpha_{Ray}(\lambda, r) = N(r) \sigma_{Ray}(\lambda) = N(r) 4.56 \left(\frac{\lambda}{550nm}\right)^{-4} \cdot 10^{-31} m^2$$

with $\sigma_{Ray}(\lambda)$ denoting the Rayleigh cross section resp. absorption coefficient.

B.2 Conventional DIAL technique

The measuring of the concentration of one particular molecular species requires two different wavelengths tuned "online" and "off-line" a selected absorption line, e.g. a peak in $\sigma_{Ray}(\lambda)$. The extinction properties of all other atmospheric constituents can be taken as nearly constant in this small wavelength interval. Following Poberaj (2001), the logarithm of the proportion of equation (B.1) for two wavelengths is taken, the result is differentiated with respect to the range R. The average over the range interval then forms the DIAL equation (Schotland, 1974):

$$\overline{N}(R) = \frac{1}{2\Delta\sigma(R)\Delta R} \ln \frac{S_{off}(R+\Delta R/2)S_{on}(R-\Delta R/2)}{S_{on}(R+\Delta R/2)S_{off}(R-\Delta R/2)}$$

Having available the differential absorption cross section $\Delta\sigma(R)$, the number density can be calculated without the knowledge of the system function $C(\lambda, R)$. For the conversion to the volume mixing ratio given in ppmv, $\overline{N}(R)$ is divided by the ambient atmospheric number density.

To compare it with ECMWF analysed specific humidity, ppmv_{H_2O} can be converted to g/kg using the factor (Liechtenstein, 2000):

$$\begin{aligned} 1\,\mathrm{ppmv}_{H_2O} &= \frac{1\,\mathrm{M}_{H_2O}}{10^6\,\mathrm{M}_{air}} &= \frac{18.016\,\mathrm{g}}{28.964\cdot 10^3\,\mathrm{kg}} \\ &&= 0.622\cdot 10^{-3}\,\mathrm{g/kg} \end{aligned}$$

B.3 DIAL system of DLR

The airborne DIAL system has been developed and operated by the Lidar Group and the Institute of Atmospheric Physics of the Deutsches Zentrum für Luft- und Raumfahrt (DLR). The airborne platform was a Falcon 20E aircraft, operated by the DLR. The Falcon has a typical air speed of 200 m/s and can reach an altitude up to 13.5 km.

Detailed descriptions of the particular system are given by Kiemle et al. (1997), Ehret et al. (1999) and Poberaj (2001) and their comparisons with a meso-scale model and ECMWF analyses show good agreement.

The transmitter is a solid-state pulsed laser. It consists of a tunable optical parametric oscillator (OPO) based on a potassium titanyl phosphate crystal. Basically, an OPO is an optical frequency converter that can convert radiation from a pump laser into tunable light in the desired wavelength region. The OPO is pumped by the second harmonic of a Nd:YAG laser with a wavelength of 1064 nm with a frequency of 100 Hz. This wavelength is additionally used for backscatter measurements directly. A single mode external cavity diode laser serves as injection seeding for the wavelength control of the OPO. The receiver system consists of a Cassegrain telescope with an aperture of 35 cm, filters and silicon avalanche photo-diodes as detectors.

The DLR DIAL operates in the 940 nm water vapor band, containing strong

lines suitable for the dry air in the lower stratosphere.

Instead of using a second wavelength, as a conventional DIAL would, a new, patented technique is used (Fix and Ehret, 1997; Fix et al., 1998): The spectral bandwidth of the unseeded OPO is nearly three orders of magnitude larger and experiences only 3% of the absorption cross section compared to the narrow-band seeded OPO signal. Thus, the unseeded signal can be used as "off-line" pulse.

B.4 Measurement errors of DLR - DIAL

From Poberaj (2001):

> "The estimated systematic measurement errors are 5 %. An accuracy of the evaluated water vapour fields depends mainly on the knowledge of the water vapour absorption line-parameters, spectral properties of the OPO and atmospheric parameters, such as the temperature, pressure and backscatter ratio."

The relevant line-profile parameters were determined in the laboratory using a high resolution spectrometer (bandwidth < 20 MHz) and the spectral purity was controlled in-flight for each on-line shot by means of a multi-pass absorption cell filled with water vapour. And proceeding:

> "Spectral purity higher than 99 % could be maintained. ... The vertical temperature and pressure profile were measured by dropsondes. Backscatter ratio profiles for the Rayleigh-Doppler correction were obtained from the lidar channel at 1064 nm. Generally, this correction can be very accurately performed in clean atmospheric regions as they were found inside the stratospheric intrusions"

Appendix C

Low Frequency Variability of the Winter Tropopause

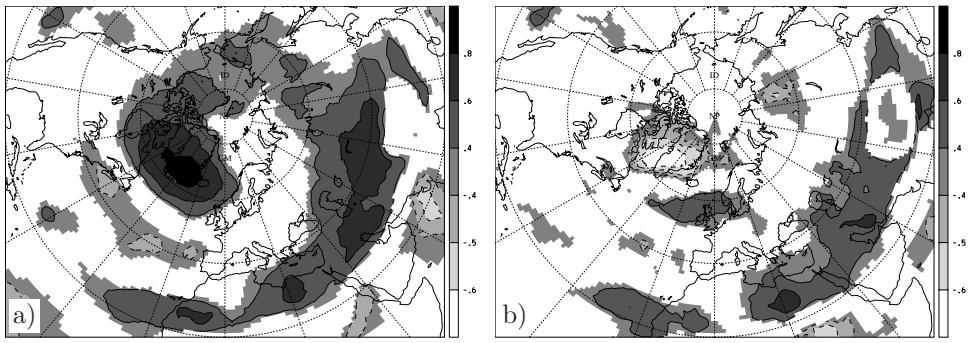

Figure C.1: Spearman's correlation of wintertime monthly NAO index to (a) monthly average and (b) monthly standard deviation. Only correlation with a significance over 90% are shown.

The winter monthly PV values on the corresponding isentrope reveal significant correlation with the corresponding NAO values (Fig. C.1). The monthly mean values exhibit a positive correlation over northern most Atlantic and northern Africa with an extension towards east (Panel a). A weaker negative correlation is found over the Atlantic located along the southern edge of the storm track. The dominance of the positive correlation is due to the non-normal distribution of PV (see Section 5.6).

The winter monthly PV standard deviation exhibits also patterns of correlation with the NAO index (Fig. C.1b). Over Greenland a significant negativ correlation is found indicating the lower variability during phases of positive NAO. The opposite is found over Great Britain and southern Scandinavia what is related to the enhanced storm activity in these regions during high NAO. Again, a band of positive NAO can be found over northern Africa and towards east. It is not clear however, why these structures emerge. Note, that the chosen isentropes are very steep in this region or even close to the ground. A high NAO index could have a subtropical surface signal in this region or correlate with the steepness of the isentropes (resp. baroclinicity) in mid-tropospheric levels. The eastern region could be very sensitive on the strength of the variability over Western Europe. During low NAO, the cyclones are weaker and usually desintegrate much more rapidly over the European continent and Mediterranean. Also, the correlation of the NAO with the annular mode indicates, that the value of the chosen isentrope could correlate with the NAO itself. The low correlation in the other subtropical regions though does not strengthen this thesis.

Bibliography

Ambaum, M., 1997: Isentropic formation of the tropopause. *J. Atmos. Sci.*, **54**, 555–568.

Andersson, E., et al., 1998: The ECMWF implementation of three-dimensional variational assimilation (3D-Var). III: Experimental results. *Quart. J. Roy. Meteor. Soc.*, **124**(550), 1831–1860.

Appenzeller, C., and H. C. Davies, 1992: Structure of stratospheric intrusions into the troposphere. *Nature*, **358**(6387), 570–572.

Appenzeller, C., H. C. Davies, and W. A. Norton, 1996: Fragmentation of stratospheric intrusions. *J. Geophys. Res.*, **101**(D1), 1435–1456.

Aref, H., 1984: Stirring by chaotic advection. *J. Fluid Mech.*, **143**, 1–21.

Baker, M. N., and D. M. Cunnold, 2001: The uses and limitations of contour advection as a technique for examining arctic vortex dynamics. *J. Atmos. Sci.*, **58**, 2210–2221.

Bell, G. D., et al., 2000: Climate assessment for 1999. *Bull. Amer. Meteor. Soc.*, **81**(6), S1–S50.

Bertin, F., B. Campistron, J. L. Caccia, and R. Wilson, 2001: Mixing processes in a tropopause folding observed by a network of ST radar and lidar. *Ann. Geophys.*, **19**, 953–963.

Bishop, C. H., and A. J. Thorpe, 1994: Potential vorticity and the electrostatics analogy - quasi-geostrophic theory. *Quart. J. Roy. Meteor. Soc.*, **120**(517), 713–731.

Bithell, M., and L. J. Gray, 1997: Contour lengthening rates near the tropopause. *Geophys. Res. Let.*, **24**(22), 2721–2724.

Blackmon, M. L., 1976: A climatological spectral study of the 500 mb geopotential height of the Northern Hemisphere. *J. Atmos. Sci.*, **33**, 1607–1623.

Bleck, R., and C. Mattocks, 1984: A preliminary analysis of the role of potential vorticity in Alpine lee cyclogenesis. *Contrib. Atmos. Phys.*, **57**(3), 357–368.

Bougeault, P., P. Binder, and J. Küttner, 1998: MAP Science Plan, [Available from MAP Data Centre, ETH, Zürich, CH-8093, Switzerland or `http://www.map.ethz.ch`].

Bougeault, P., P. Binder, A. Buzzi, R. Dirks, R. Houze, J. Küttner, R. B. Smith, R. Steinacker, and H. Volkert, 2001: The map special observing period. *Bull. Amer. Meteor. Soc.*, **82**(3), 433–462.

Bourqui, M., 2001: Stratosphere - troposphere investigations, Ph.D. thesis, Swiss Federal Institute of Technology (ETH), Dissertation Nr. 14054.

Bowman, K. P., and P. Chen, 1994: Mixing by barotropic instability in a nonlinear model. *J. Atmos. Sci.*, **51**(24), 2416–2427.

Brasseur, G. P., et al., 1998: European scientific assessment of the atmospheric effects of aircraft emissions. *Atmos. Envir.*, **32**(13), 2319–2418.

Bresch, D. N., 1998: Coupled flow and SST patterns of the north Atlantic: A statistical and dynamical study, Ph.D. thesis, Swiss Federal Institute of Technology (ETH), Dissertation Nr. 12878.

Brewer, A. W., 1949: Evidence for a world circulation provided by the measurements of helium and water vapor distribution in the stratosphere. *Quart. J. Roy. Meteor. Soc.*, **75**, 351–363.

Browning, K. A., 1990: *Organisation of clouds and precipitation in extratropical cyclones*, pp. 129–154, Extratropical cyclones. The Erik Palmen Memorial Volume, ed. by C. Newton and E. O. Holopainen, American Meteorological Society.

Brunet, G., R. Vautard, B. Legras, and S. Edouard, 1995: Potential vorticity on isentropic surfaces: Climatology and diagnostics. *Mon. Wea. Rev.*, **123**, 1037–1058.

Butchart, N., and E. E. Remsberg, 1986: The area of the stratospheric polar vortex as a diagnostic for tracer transport on an isentropic surface. *J. Atmos. Sci.*, **43**(13), 1319–1339.

Chen, P., 1995: Isentropic cross-tropopause mass-exchange in the extratropics. *J. Geophys. Res.*, **100**(D8), 16,661–16,673.

Chen, P., J. R. Holton, A. O'Neill, and R. Swinbank, 1994: Quasi-horizontal transport and mixing in the Antartcic stratosphere. *J. Geophys. Res.*, **99**(D8), 16,851–16,866.

Collis, R. T. H., and P. B. Russel, 1976: *Lidar Measurements of Particles and Gases by Elastic Backscattering and Differential Absorbtion*. in "Laser Monitoring of the Atmosphere", Springer.

Courtier, P., E. Andersson, W. Heckley, J. Pailleux, D. Vasiljevic, M. Hamrud, A. Hollingsworth, E. Rabier, and M. Fisher, 1998: The ECMWF implementation of three-dimensional variational assimilation (3D-Var). I: Formulation. *Quart. J. Roy. Meteor. Soc.*, **124**(550), 1783–1807.

Danielsen, E. F., 1968: Stratospheric-tropospheric exchange based on radioactivity, ozone and potential vorticity. *Quart. J. Roy. Meteor. Soc.*, **25**(3), 502–518.

Danielsen, E. F., R. S. Hipskind, S. E. Gaines, G. W. Sachse, G. L. Gregory, and G. F. Hill, 1987: Three-dimensional analysis of potential vorticity associated with tropopause folds and observed variations of ozone and carbon-monoxide. *J. Geophys. Res.*, **92**(D2), 2103–2111.

Davies, H. C., and A. M. Rossa, 1998: PV frontogenesis and upper-tropospheric fronts. *Mon. Wea. Rev.*, **126**, 1528–1539.

Davis, C. A., and K. A. Emanuel, 1991: Potential vorticity diagnostics of cyclogenesis. *Mon. Wea. Rev.*, **119**(8), 1929–1953.

del Castillo-Negrete, D., and P. J. Morrison, 1993: Chaotic transport by Rossby waves in a shear flow. *Phys. Fluids A*, **5**, 948–965.

Derome, J., G. Brunet, and J. H. Wang, 2001: On the potential vorticity balance on an isentropic surface during normal and anomalous winters. *Mon. Wea. Rev.*, **129**(5), 1208–1220.

Dessler, A. E., and S. C. Sherwood, 2000: Simulations of tropical upper tropospheric humidity. *J. Geophys. Res.*, **105**(D15), 20,155–20,163.

Dobson, G. M. B., 1956: Origin and distribution of the polyatomic molecules in the atmosphere. *Proc. Roy. Soc. London*, **A236**, 187–192.

Dritschel, D. G., 1989: Contour dynamics and contour surgery: Numerical algorithms for extended, high-resolution modelling of vortex dynamics into two-dimensional, inviscid, incompressible flows. *Computer Phys. Rep.*, **10**, 77–146.

ECMWF, 2001: `http://www.ecmwf.int`.

Edouard, S., R. Vautard, and G. Brunet, 1997: On the maintenance of potential vorticity in isentropic coordinates. *Quart. J. Roy. Meteor. Soc.*, **123**(543), 2069–2094.

Ehret, G., K. P. Hoinka, J. Stein, A. Fix, C. Kiemle, and G. Poberaj, 1999: Low stratospheric water vapor measured by an airborne DIAL. *J. Geophys. Res.*, **104**(D24), 31,351–31,359.

Einstein, A., 1905: Über die von der molekularkinetischen Theorie der Wärme geforderte Bewegung von in ruhenden Flüssigkeiten suspendierten Teilchen. *Ann. Physik*, **17**(8), 549–560.

Eisele, H., H. E. Scheel, R. Sladkovic, and T. Trickl, 1999: High-resolution lidar measurements of stratosphere-troposphere exchange. *J. Atmos. Sci.*, **56**(2), 319–330.

Elbern, H., J. Hendricks, and A. Ebel, 1998: A climatology of tropopause folds by global analysis. *Theor. Appl. Climatol.*, **59**(3-4), 181–200.

Er-El, J., and R. L. Peskin, 1981: Relative diffusion of constant-level balloons in the southern hemisphere. *J. Atmos. Sci.*, **38**, 2264–2274.

Ertel, H., 1942: Ein neuer hydrodynamiscer Wirbelsatz. *Meteor. Zeitschr.*, **59**, 277–281.

Eumetsat, 2001: `http://www.eumetsat.de`.

Fehlmann, R., and C. Quadri, 2000: Predictability issues of heavy Alpine south-side precipitation. *Meteor. Atmos. Phys.*, **72**(2-4), 223–231.

Fehlmann, R., C. Quadri, and H. C. Davies, 2000: An Alpine rainstorm: Sensitivity to the mesoscale upper-level structure. *Wea. Forecasting*, **15**(1), 4–28.

Ficker, H., 1920: Der Einfluss der Alpen auf Fallgebiete des Luftdrucks und die Entstehung von Depressionen über dem Mittelmeer. *Meteor. Zeitschr.*, **37**(12), 350–363.

Fischer, H., N. Eigenwillig, and H. Müller, 1981: Information content of METEOSAT and Nimbus/THIR water vapor channel data: Altitude association of observed phenomena. *J. Appl. Meteor.*, **20**(11), 1344–1352.

Fischer, H., F. G. Wienhold, P. Hoor, O. Bujok, C. Schiller, P. Siegmund, M. Ambaum, H. A. Scheeren, and J. Lelieveld, 2000: Tracer correlations in the northern high latitude lowermost stratosphere: Influence ofcross-tropopause mass exchange. *J. Geophys. Res.*, **27**(1), 97–100.

Fix, A., and G. Ehret, 1997: *Injection seeded optical parametric oscillator system for water vapor DIAL measurements*, pp. 313–316, in "Advances in Atmospheric Remote Sensing with Lidar: Selected papers of the 18^{th} International Laser Radar Conference", ed. by A. Ansmann et al, Springer.

Fix, A., V. Weiss, and G. Ehret, 1998: Injection-seeded optical parametric oscillator for airborne water vapor DIAL. *Pure Appl. Opt.*, **7**, 837–852.

Gouget, H., G. Vaughan, A. Marenco, and H. G. J. Smith, 2000: Decay of a cut-off and contribution to stratosphere-troposphere exchange. *Quart. J. Roy. Meteor. Soc.*, **126**(564), 1117–1141.

Gray, L. J., M. Bithell, and B. D. Cox, 1994: The role of specific-humidity fields in the diagnosis of stratosphere-troposphere exchange. *Geophys. Res. Let.*, **21**(19), 2103–2106.

Haidvogel, D. B., and G. Halloway, 1984: Predictability: Lagrangian and eulerian views. *AIP Conference Proceedings: Predictability of Fluid Motions*, G. Holloway and B. J. West, Eds., vol. 106, pp. 67–77.

Haynes, J. R., T. G. McIntyre, and K. P. Shine, 1991: On the "downward control" of extratropical diabatic circulations by eddy-induced mean zonal forces. *J. Atmos. Sci.*, **48**, 651–678.

Haynes, P., and E. Shuckburgh, 2000a: Effective diffusivity as a diagnostic of atmospheric tranosport 1. stratosphere. *J. Geophys. Res.*, **105**(D18), 22,777–22,794.

Haynes, P., and E. Shuckburgh, 2000b: Effective diffusivity as a diagnostic of atmospheric tranosport 2. troposphere and lower stratosphere. *J. Geophys. Res.*, **105**(D18), 22,795–22,810.

Haynes, P., J. Scinocca, and M. Greenslade, 2001: Formation and maintainance of the extratropical tropopause by baroclinic eddies. *Geophys. Res. Let.*, **28**(22), 4179–4128.

Hoinka, K. P., E. Richard, G. Poberaj, R. Busen, J.-L. Caccia, A. Fix, and H. Mannstein, 2003: Analysis of a potential vorticity streamer crossing the Alps during MAP SOP on 6 November 1999. *Quart. J. Roy. Meteor. Soc.*. In press.

Holton, J. R., 1979: *An Introduction to Dynamic Meteorology*. vol. 23 of *International*

Geophysics Series, 2nd ed., Academic Press Inc.

Holton, J. R., P. Haynes, M. E. McIntyre, A. R. Douglass, R. B. Rood, and L. Pfister, 1995: Stratosphere-troposphere exchange. *Rev. Geophys.*, **33**(4), 403–439.

Hortal, M., and A. J. Simmons, 1991: Use of reduced gaussian grids in spectral models. *Mon. Wea. Rev.*, **119**(4), 1057–1074.

Hoskins, B. J., 1991: Towards a pv-theta view of the general circulation. *Tellus*, **43AB**, 27–35.

Hoskins, B. J., and K. I. Hodges, 2002: New perspectives on the northern hemisphere winter storm tracks. *J. Atmos. Sci.*, **59**, 1041–1061.

Hoskins, B. J., and P. J. Valdes, 1990: On the existence of storm-tracks. *J. Atmos. Sci.*, **47**(15), 1854–1864.

Hoskins, B. J., M. E. McIntyre, and A. W. Robertson, 1985: On the use and significance of isentropic potential vorticity. *Quart. J. Roy. Meteor. Soc.*, **111**(470), 877–946.

Juckes, M. N., and M. E. McIntyre, 1987: A high-resolution one-layer model of breaking planetary-waves in the stratosphere. *Nature*, **328**(6131), 590–596.

Kärcher, B., 1999: Aviation-produced aerosols and contrails. *Surveys Geophys.*, **20**(2), 113–167.

Kida, H., 1977: A numerical investigation of the atmospheric general circulation and stratospheric-tropospheric mass exchange: II. Lagrangian motion of the atmosphere. *J. Meteor. Soc. Jap.*, **55**(1), 71–88.

Kiemle, C., G. Ehret, A. Giez, K. J. Davis, D. H. Lenschow, and S. P. Oncley, 1997: Estimation of boundary layer humidity fluxes and statistics from airborne differential absorption lidar (DIAL). *J. Geophys. Res.*, **102**(D24), 29,189–29,203.

Kleinschmidt, E., 1950: Über Aufbau und Entstehung von Zyklonen. I. Teil. *Meteor. Rundschau*, **3**(1), 1–6.

Klinker, E., E. Rabier, G. Kelly, and J. F. Mahfouf, 2000: The ECMWF operational implementation of four-dimensional variational assimilation. III: Experimental results and diagnostics with operational configuration. *Quart. J. Roy. Meteor. Soc.*, **126**(564), 1191–1215.

Knudsen, B. M., J. P. Pommereau, A. Garnier, M. Nunez-Pinharanda, L. Denis, G. Letrenne, M. Durand, and J. M. Rosen, 2001: Comparison of stratospheric air parcel trajectories based on different meteorological analyses. *J. Geophys. Res.*, **106**(D4), 3415–3424.

Kowol-Santen, J., H. Elbern, and A. Ebel, 2000: Estimation of cross-tropopause airmass fluxes at midlatitudes: Comparison of different numerical methods and meteorological situations. *Mon. Wea. Rev.*, **128**(12), 4045–4057.

Lait, L. R., 1994: An alternative form for potential vorticity. *J. Atmos. Sci.*, **51**(12), 1754–1759.

Lamarque, J. F., and P. G. Hess, 1994: Cross-tropopause mass-exchange and potential vorticity budget in a simulated tropopause folding. *J. Atmos. Sci.*, **51**(15), 2246–2269.

Lelieveld, J., B. Bregman, F. Arnold, V. Burger, P. J. Crutzen, H. Fischer, A. Waibel, and P. Siegmund, 1997: Chemical perturbation of the lowermost stratosphere through exchange with the troposphere. *J. Geophys. Res.*, **24**(5), 603–606.

Lichtenberg, A. J., and M. A. Lieberman, 1992: *Regular and Chaotic Dynamics*. vol. 38 of *Applied Mathematical Sciences*, 2nd ed., Springer.

Liechtenstein, L., 2000: *A detailed Analysis of a PV Streamer over Western Europe in November 1999*. Diploma thesis, Institute for Atmospheric Science, ETH Zürich.

Liniger, M. A., and H. C. Davies, 2003: Sub-structure of a MAP streamer. *Quart. J. Roy. Meteor. Soc.*. In press.

Lyapunov, A. M., 1907: Problème general de la stabilité de mouvement. *Ann. Fac. Sci. Toulouse*, **9**, 203–474. Reprinted in Ann. Math. Stud., **17**, 1949.

Mahfouf, J. F., and E. Rabier, 2000: The ECMWF operational implementation of four-dimensional variational assimilation. II: Experimental results with improved physics. *Quart. J. Roy. Meteor. Soc.*, **126**(564), 1171–1190.

Manney, G. L., and J. L. Stanford, 1987: On the relation of 6.7 μm water vapour features to isentropic distributions of potential vorticity. *Quart. J. Roy. Meteor. Soc.*, **113**, 1048–1057.

Manney, G. L., J. A. Michelsen, F. W. Irion, G. C. Toon, M. R. Gunson, and A. E. Roche, 2000: Lamination and polar vortex development in fall from ATMOS long-lived gases observed during november 1994. *J. Geophys. Res.*, **105**(D23), 29,023–29,038.

Martin, J. E., Mon. Wea. Rev.: Quasigeostrophic forcing of ascent in the occluded sector of cyclones and the trowal airstream. *1999*, **127**(1), 70–88.

Maryon, R. H., and A. T. Buckland, 1995: Tropospheric dispersion: the first ten days after a puff release. *Quart. J. Roy. Meteor. Soc.*, **121**, 1799–1833.

Massacand, A. C., 1999: Linkages between upper-tropospheric flow and European seasonal weather, Ph.D. thesis, Swiss Federal Institute of Technology (ETH), Dissertation Nr. 13300.

Massacand, A. C., and H. C. Davies, 2001a: Interannual variability of european winter weather: The potential vorticity insight. *Atmos. Sci. Let.* doi:10.1006/asle.2001.0026.

Massacand, A. C., and H. C. Davies, 2001b: Interannual variability of the extratropical northern hemisphere and the potential vorticity wave guide. *Atmos. Sci. Let.* doi:10.1006/asle.2001.0027.

Massacand, A. C., H. Wernli, and H. C. Davies, 1998: Heavy precipitation on the Alpine southside: An upper-level precursor. *Geophys. Res. Let.*, **25**(9), 1435–1438.

McIntyre, M. E., 1980: Towards a Lagrangian-mean description of stratospheric circulations and chemical transports. *Phil. Trans. R. Soc. Lond. A*, **296**, 129–148.

McIntyre, M. E., and T. N. Palmer, 1983: Breaking planetary waves in the stratosphere. *Nature*, **305**, 593–600.

McIntyre, M. E., and T. N. Palmer, 1984: The surf zone in the stratosphere. *J. Atmos. Terr. Phys.*, **46**, 825–849.

Measures, R. M., 1984: *Laser Remote Sensing: Fundamentals and Applications*. Wiley.

Methven, J., and B. Hoskins, 1999: The advection of high-resolution tracers by low-resolution winds. *J. Atmos. Sci.*, **56**, 3262–3285.

Morgan, M. C., and J. W. Nielsen-Gammon, 1998: Using tropopause maps to diagnose midlatitude weather systems. *Mon. Wea. Rev.*, **126**(10), 2555–2579.

Morgenstern, O., and H. C. Davies, 1999: Disruption of an upper-level PV-streamer by orographic and cloud-diabatic effects. *Contr. Atmos. Phys.*, **72**, 172–186.

Muraki, D. J., and G. J. Hakim, 2001: Balanced asymmetries of waves on the tropopause. *J. Atmos. Sci.*, **58**(3), 237–252.

Nakamura, N., 1995: Modified Lagrangian-mean diagnostics of the stratospheric polar vortices. Part I: Formulation and analysis of GFDL SKYHI GCM. *J. Atmos. Sci.*, **52**(11), 2096–2108.

Nash, E. R., P. A. Newmann, J. E. Rosenfield, and M. R. Schoeberl, 1996: An objective determination of the polar vortex using ertel's potential vorticity. *J. Geophys. Res.*, **101**(D5), 9471–9478.

Newman, P. A., and M. R. Schoeberl, 1995: A reinterpretation of the data from the NASA stratosphere-troposphere exchange project. *Geophys. Res. Let.*, **22**(18), 2501–2504.

Ngan, K., and T. G. Shepherd, 1999: A closer look at chaotic advection in the stratosphere.

Part II: Statistical diagnostics. *J. Atmos. Sci.*, **56**, 4153–4166.

Norton, W. A., 1994: Breaking Rossby waves in a model stratosphere diagnosed by a vortex-following coordinate system and a technique for advecting material contours. *J. Atmos. Sci.*, **51**(4), 654–676.

O'Connor, F. M., G. Vaughan, and H. de Backer, 1999: Observations of subtropical air in the European mid-latitude lower stratosphere. *Quart. J. Roy. Meteor. Soc.*, **125**(560), 2965–2986.

Ottino, J. M., 1989: *The Kinematics of Mixing: Stretching, Chaos and Transport*. Cambridge texts in applied mathematics, Cambridge University Press.

Peters, D., and D. W. Waugh, 1996: Influence of barotropic shear on the poleward advection of upper-tropospheric air. *J. Atmos. Sci.*, **53**(21), 3013–3031.

Petterssen, S., 1956: *Weather analysis and Forecasting*. Vol 1, Motion and motion systems, 2^{nd} ed., McGraw-Hill, New York, 428pp.

Pierce, R. B., and T. D. Fairlie, 1993: Chaotic advection in the stratosphere: Implications for the dispersal of chemically perturbed air from the polar vortex. *J. Geophys. Res.*, **98**(D10), 18,589–18,595.

Pierrehumbert, R. T., and R. Roca, 1998: Evidence for control of atlantic subtropical humidity by large scale advection. *Geophys. Res. Let.*, **25**(24), 4537–4540.

Pierrehumbert, R. T., and H. Yang, 1993: Global chaotic mixing on isentropic surfaces. *J. Atmos. Sci.*, **50**(15), 2462–2480.

Platzmann, G. W., 1968: The Rossby wave. *Quart. J. Roy. Meteor. Soc.*, **94**(401), 225–248.

Poberaj, G., 2001: Airborne differential absorption lidar for water vapour measurements in the upper troposphere and lower stratosphere in the spectral region around 940 nm, Ph.D. thesis, University of Ljubljana.

Poc, M. M., M. Roulleau, N. A. Scott, and A. Chedin, 1980: Quantitative studies of Meteosat water-vapor channel data. *J. Appl. Meteor.*, **19**, 868–876.

Polvani, L. M., and R. A. Plumb, 1992: Rossby-wave breaking, microbreaking, filamentation, and secondary vortex formation: The dynamics of a perturbated vortex. *J. Atmos. Sci.*, **49**(6), 462–476.

Polvani, L. M., and R. Saravanan, 2000: Three-dimensional structure of breaking Rossby waves in the polar wintertime stratosphere. *J. Atmos. Sci.*, **57**, 3663–3685.

Pomroy, H. R., and A. J. Thorpe, 2000: The evolution and dynamical role of reduced upper-tropospheric potential vorticity in intensive observing period one of FASTEX. *Mon. Wea. Rev.*, **128**(6), 1817–1834.

Popovic, J. M., and R. A. Plumb, 2001: Eddy shedding from the upper-tropospheric Asian monsoon anticyclone. *J. Atmos. Sci.*, **58**(1), 93–104.

Postel, G. A., and M. H. Hitchman, 1999: A climatology of Rossby wave breaking along the subtropical tropopause. *J. Atmos. Sci.*, **56**, 359–373.

Price, J. D., and G. Vaughan, 1993: The potential for stratosphere troposphere exchange in cut-off-low systems. *Quart. J. Roy. Meteor. Soc.*, **119**(510), 343–365.

Provenzale, A., 1999: Transport by coherent barotropic vortices. *Annu. Rev. Fluid Mech.*, **31**, 55–93.

Pudykiewicz, J. A., and A. S. Koziol, 1998: An application of the theory of kinematics of mixing to the study of tropospheric dispersion. *Atmos. Envir.*, **32**(24), 4227–4244.

Rabier, E., A. McNally, E. Andersson, P. Courtier, P. Unden, J. Eyre, A. Hollingsworth, and F. Boutier, 1998: The ECMWF implementation of three-dimensional variational assimilation (3d-var). II: Structure functions. *Quart. J. Roy. Meteor. Soc.*, **124**(550), 1809–1829.

Rabier, E., H. Jarvinen, E. Klinker, J. F. Mahfouf, and A. Simmons, 2000: The ECMWF operational implementation of four-dimensional variational assimilation. I: Experimental results with simplified physics. *Quart. J. Roy. Meteor. Soc.*, **126**(564), 1143–1170.

Ramond, D., H. Corbin, M. Desbois, G. Szejwach, and P. Waldteufel, 1981: The dynamics of polar jet streams as depicted by the METEOSAT WV channel radiance field. *Mon. Wea. Rev.*, **109**, 2164–2176.

Ravetta, F., G. Ancellet, J. Kowol-Santen, R. Wilson, and D. Nedeljkovic, 1999: Ozone, temperature and wind field measurements in a tropopause fold: Comparison with a mesoscale model simulation. *Mon. Wea. Rev.*, **127**, 2641–2653.

Richardson, L. F., 1926: Atmospheric diffusion shown on a distance - neighbour graph. *Proc. Roy. Soc. London*, **110**(A), 709–737.

Richardson, L. F., 1948: Note on eddy diffusion in the sea. *J. Meteor.*, **5**(5), 238–240.

Ritchie, H., C. Temperton, A. Simmons, M. Hortal, T. Davies, D. Dent, and M. Hamrud, 1995: Implementation of the semi-lagrangian method in a high-resolution version of the ECMWF forecast model. *Mon. Wea. Rev.*, **123**(2), 489–514.

Robock, A., 2000: Volcanic eruptions and climate. *Rev. Geophys.*, **38**(2), 191–219.

Schär, C. J., 1989: Dynamische Aspekte der aussertropischen Zyklogenese, Theorie und numerische Simulation im Limit der balancierten Strömungsanalyse, Ph.D. thesis, Eidgenössische Technische Hochschule ETH, Dissertation Nr. 8845.

Schmetz, J., and O. M. Turpeinen, 1988: Estimation of the upper tropospheric relative humidity field from METEOSAT water vapor image data. *J. Appl. Meteor.*, **27**(8), 889–899.

Schoeberl, M. R., and P. A. Newman, 1995: A multiple-level trajectory analysis of vortex filaments. *J. Geophys. Res.*, **100**(D12), 25,801–25,815.

Schotland, R. M., 1974: Errors in the lidar measurement of atmospheric gases by diffential absorption. *J. Appl. Meteor.*, **13**, 71–77.

Schumann, U., J. Strom, R. Busen, R. Baumann, K. Gierens, M. Krautstrunk, F. P. Schroder, and J. Stingl, 1996: In situ observations of particles in jet aircraft exhausts and contrails for different sulfur-containing fuels. *J. Geophys. Res.*, **101**(D3), 6853–6869.

Schwierz, C. B., 2001: Interactions of Greenland-scale orography and extra-tropical synoptic-scale flow, Ph.D. thesis, Swiss Federal Institute of Technology (ETH), Dissertation Nr. 14356.

Shapiro, M. A., 1980: Turbulent mixing within tropopause folds as a mechanism for the exchange of chemical constituents between the stratosphere and troposphere. *J. Atmos. Sci.*, **37**, 994–1004.

Simmons, A. J., D. M. Burridge, M. Jarraud, C. Girard, and W. Wergen, 1989: The ECMWF medium-range prediction models development of the numerical formulations and the impact of increased resolution. *Meteor. Atmos. Phys.*, **40**(1-3), 28–60.

Sobel, A. H., R. A. Plumb, and D. W. Waugh, 1997: Methods of calculating transport across the polar vortex edge. *J. Atmos. Sci.*, **54**(18), 2241–2260.

Soden, B. J., and F. P. Bretherton, 1993: Upper tropospheric relative humidity from the GOES 6.7 μm channel: Method and climatology for July 1987. *J. Geophys. Res.*, **98**(D9), 16,669–16,688.

Stoelinga, M. T., 1996: A potential vorticity-based study of the role of diabatic heating and friction in a numerically simulated baroclinic cyclone. *Mon. Wea. Rev.*, **124**(5), 849–874.

Stohl, A., 1998: Computation, accuracy and applications of trajectories – A review and bibliography. *Atmos. Envir.*, **32**(6), 947–966.

Stohl, A., 2001: A one-year Lagrangian "climatology" of airstreams in the northern hemisphere troposphere and lowermost stratosphere. *J. Geophys. Res.*, **106**(D7), 7263–

7279.

Stohl, A., and P. Seiber, 1998: Accuracy of trajectories as determined from the conservation of meteorological tracers. *Quart. J. Roy. Meteor. Soc.*, **124**(549), 1465–1484.

Stohl, A., and T. Trickl, 1999: A textbook example of long-range transport: Simultaneous observation of ozone maxima of stratospheric and North American origin in the free troposphere over Europe. *J. Geophys. Res.*, **104**(D23), 30,445–30,462.

Stohl, A., L. Haimberger, M. P. Scheele, and H. Wernli, 2001: An intercomparison of results from three trajectory models. *Meteor. Applic.*, **8**(2), 127–135.

Stohl, A., et al., 2000: The influence of stratospheric intrusions on alpine ozone concentrations. *Atmos. Envir.*, **34**(9), 1323–1354.

Sutton, R. T., 1994: Lagrangian flow in the middle atmosphere. *Quart. J. Roy. Meteor. Soc.*, **120**, 1299–1321.

Sutton, R. T., H. Maclean, R. Swinbank, O. Alan, and F. W. Taylor, 1994: High-resolution stratospheric tracer fields estimated from satellite observations using Lagrangian trajectory calculations. *J. Atmos. Sci.*, **51**(20), 2995–3005.

Swanson, K. L., 2001: Upper-tropospheric potential vorticity fluctuations and the dynamical relevance of the time mean. *J. Atmos. Sci.*, **58**(13), 1815–1826.

Tan, D. G. H., P. H. Haynes, A. R. MacKenzie, and J. A. Pyle, 1998: Effects of fluid-dynamical stirring and mixing on the deactivation of stratospheric chlorine. *J. Geophys. Res.*, **103**(D1), 1585–1605.

Thorpe, A. J., and C. H. Bishop, 1995: Potential vorticity and the electrostatics analogy - ertel-rossby formulation. *Quart. J. Roy. Meteor. Soc.*, **121**(526), 1477–1495.

Uccellini, L. W., D. Keyser, K. F. Brill, and C. H. Wash, 1985: The Presidents' Day cyclone of 18-19 february 1979: Influence of upstream trough amplification and associated tropopause folding on rapid cyclogenesis. *Mon. Wea. Rev.*, **113**, 962–988.

Vaughan, G., and J. D. Price, 1991: On the relation between total ozone and meteorology. *Quart. J. Roy. Meteor. Soc.*, **117**(502), 1281–1298.

Vaughan, G., J. D. Price, and A. Howells, 1994: Transport into the troposphere in a tropopause fold. *Quart. J. Roy. Meteor. Soc.*, **120**(518), 1085–1103.

Vaughan, G., H. Gouget, F. M. O'Connor, and D. Wier, 2001: Fine-scale layering on the edge of a stratospheric intrusion. *Atmos. Envir.*, **35**(12), 2215–2221.

Wallace, J. M., G.-H. Lim, and M. L. Blackmon, 1988: Relationship between cyclone tracks, anticyclone tracks and baroclinic waveguides. *J. Atmos. Sci.*, **45**, 439–462.

Walmsley, J. L., and J. Mailhot, 1983: On the numerical accuracy of trajectory models for long-range transport of atmospheric pollutants. *Atmos.-Ocean*, **21**(1), 14–39.

Waugh, D. W., and R. A. Plumb, 1994: Contour advection with surgery: Technique for investigating finescale structure in tracer transport. *J. Atmos. Sci.*, **51**(4), 530–540.

Waugh, D. W., et al., 1994: Transport out of the lower stratospheric arctic vortex by Rossby-wave breaking. *J. Geophys. Res.*, **99**(D1), 1071–1088.

Wernli, H., 1997: A Lagrangian-based analysis of extratropical cyclones. II: A detailed case-study. *Quart. J. Roy. Meteor. Soc.*, **123**, 1677–1706.

Wernli, H., and M. Bourqui, 1999: *Mesoscale Processes in the Stratosphere*, chap. A 1-year climatology of stratosphere-troposphere exchange on the northern hemisphere – quantification and associated mesoscale processes, pp. 265–270, Air pollution research report 69, EUR 18912 EN, European Community, Brussels.

Wernli, H., and M. Bourqui, 2002: A Lagrangian "one-year climatology" of (deep) cross-tropopause exchange in the extratropical northern hemisphere. *J. Geophys. Res.*, **107**(D2), 10.1029/2001JD000,812.

Wernli, H., and H. C. Davies, 1997: A Lagrangian-based analysis of extratropical cyclones.

I: The method and some applications. *Quart. J. Roy. Meteor. Soc.*, **123**, 467–489.

Wernli, H., S. Dirren, M. A. Liniger, and M. Zillig, 2002: Dynamical aspects of the life-cycle of the winter storm "LOTHAR" (24-26 December 1999). *Quart. J. Roy. Meteor. Soc.*, **128**, 405–429.

Wirth, V., 1995: Diabatic heating in an exisymmetric cut-off cyclone and related stratosphere-troposphere exchange. *Quart. J. Roy. Meteor. Soc.*, **121**, 127–147.

Wirth, V., 2001: Cyclonic-anticyclonic asymmetry concerning the height of the thermal and the dynamical tropopause. *J. Atmos. Sci.*, **58**, 26–37.

Wirth, V., and J. Egger, 1999: Diagnosing extratropical synoptic-scale stratosphere-troposphere exchange: A case study. *Quart. J. Roy. Meteor. Soc.*, **125**(554), 635–655.

Wirth, V., C. Appenzeller, and M. Juckes, 1997: Signature of induced vertical air motion accompanying quasi-horizontal roll-up of stratospheric intrusions. *Mon. Wea. Rev.*, **125**(10), 2504–2519.

Yang, H., 1998: The central barrier, asymmetry and random phase in chaotic transport and mixing by Rossby waves in a jet. *Int. J. Bif. and Chaos*, **8**(6), 1131–1152.

Zierl, B., and V. Wirth, 1997: The influence of radiation on tropopause behaviour and stratosphere-troposphere exchange in an upper tropospheric anticyclone. *J. Geophys. Res.*, **102**(D20), 23,883–23,894.

Acknowledgments

Without any claim of comleteness, I would like to thank cordially the following persons to have made this thesis possible: Huw C. Davies, Andreas Stohl, Heini Wernli, Cornelia B. Schwierz, David N. Bresch, Klaus-Peter Hoinka, Michael Sprenger, Sandro Buss, Xenia Gośl̈icka, Jan Roth, my family and Antonia Kerland.

Curriculum Vitae

Name	Mark Andrea Liniger
Address	Buckhauserstr. 18
	CH - 8048 Zürich
Telephone	+41 1 400 38 54
eMail	mark@atmos.umnw.ethz.ch
URL	www.iac.ethz.ch/staff/mark/
Date and place of birth	23rd of May, 1973 in Portland, Oregon, USA
Nationalities	Swiss and American

Education

October, 1998 - May, 2002 :
Doctorate at the Institute for Atmospheric Sciences at the Swiss Federal Institute of Technology (ETHZ) in Zürich, Switzerland under supervision of Prof. Dr. H. C. Davies.

October, 1992 - April, 1998 :
Study of physics at the ETHZ with specialization in the fields *Atmospheric Science* and *Scientific Computing*. Diploma thesis "Direct Impact of Sea Surface Temperature South of Newfoundland on the General Circulation: A Trajectory Analysis", under supervision of Prof. Dr. Huw C. Davies and Dr. David N. Bresch.
Dipl. Phys. ETH

1986 - 1992 :
Kantonsschule Wiedikon in Zürich, Switzerland
Matura Typus B

1980 - 1986 :
Primary school in Zürich, Switzerland.

International conferences and special training courses

EGS (European Geophysical Society) XXVII General Assembly, Nice, 21 - 26 April 2002; Training course "Predictability, diagnostics and seasonal forecasting", ECMWF, Reading, UK, 8 - 12 April 2002; 8th Scientific Assembly of IAMAS, Innsbruck, Austria, 10 - 18 July 2001; 13th Conference on Atmospheric and Oceanic Fluid Dynamics, Breckenridge, Colorado, USA, 4 - 8 June 2001; MAP-meeting 2001, Schliersee, Germany, 16. May 2001; EGS (European Geophysical Society) XXV General Assembly, Nice, 25 - 29 April 2000; Summerschool "Transport and mixing in geophysical flows", Aosta, Italy, 14 - 25 June 1999.

Practical experience

May, 2002 - :
PostDoc position at MeteoSwiss, Zürich.

May, 1996 - July, 1996 :
Teaching mathematics at Kantonsschule Wiedikon, Zürich.

December, 1994 - January, 1996 :
Software developing at Zürich Life Insurance in a 20% position, Zürich.